MID-INFRARED QUANTUM CASCADE LASER

A THESIS SUBMITTED TO

THE GRADUATE SCHOOL OF ENGINEERING AND SCIENCE

OF BILKENT UNIVERSITY

IN PARTIAL FULFILLMENT OF THE REQUIREMENTS FOR

THE DEGREE OF

MASTER OF SCIENCE

IN

ELECTRICAL AND ELECTRONICS ENGINEERING

By

Berkay Bozok

May 2017

MID-INFRARED QUANTUM CASCADE LASER

By Berkay Bozok

May 2017

We certify that we have read this thesis and that in our opinion it is fully adequate, in scope and in quality, as a thesis for the degree of Master of Science.

Ekmel Özbay (Advisor)

Bayram Bütün (Co-Advisor)

Vakur Behçet Ertürk

Hamza Kurt

Approved for the Graduate School of Engineering and Sciences:

Ezhan Karaşan

Director of Graduate School

ABSTRACT

MID-INFRARED QUANTUM CASCADE LASER

Berkay Bozok
M.S. in Electrical and Electronics Engineering
Advisor: Ekmel Özbay & Bayram Bütün
May 2017

Mid-infrared quantum cascade laser technology has been developed rapidly since it was demonstrated in 1994. Since quantum cascade laser technology is small, robust and efficient, they have become commonly used mid-infrared laser source for various applications. The particular application fields of quantum cascade lasers are free space communication, chemical spectroscopy, environmental monitoring and infrared countermeasure.

This work presents a comprehensive study over mid-infrared quantum cascade laser including review of theoretical background, theoretical analyses, active layer design, quantum mechanical, thermal and optical simulations, device fabrication, optimization and experimental characterization.

As a result of this work mid-infrared quantum cascade laser have been successfully demonstrated.

Keywords: Laser, Mid-infrared, MWIR, Quantum cascade laser, QCL, Intersubband transition, Wave function engineering.

ÖZET
ORTA KIZILÖTESİ KUANTUM ÇAĞLAYAN LAZER

Berkay Bozok
Elektrik ve Elektronik Mühendisliği, Yüksek Lisans
Tez Danışmanı: Ekmel Özbay & Bayram Bütün
Mayıs 2017

Orta kızılötesi kuantum çağlayan lazer teknolojisi, 1994 yılında icadından beri hızla gelişmiştir. Kuantum çağlayan lazer teknolojisi küçük, karmaşık olmayan ve verimli olduğundan, çeşitli uygulamalar için en çok kullanılan orta kızılötesi lazer kaynağı haline gelmiştir. Kuantum çağlayan lazerlerinin özel uygulama alanları serbest alan iletişimi, kimyasal spektroskopi, çevresel izleme ve kızılötesi karşı önlemlerdir.

Bu çalışma teorik arka plan incelemesi, teorik analizler, kuantum çağlayan lazer tasarımı, kuantum mekanik, termal ve optik simülasyonlar, cihaz imalatı, optimizasyonu ve deneysel karakterizasyonu içeren orta kızılötesi kuantum çağlayan lazeri üzerinde kapsamlı bir analiz sunmaktadır.

Bu çalışma sonucunda orta kızılötesi kuantum çağlayan lazer başarıyla geliştirilmiş ve üretilmiştir.

Anahtar Sözcükler: Lazer, Orta kızılötesi, Kuantum çağlayan lazer, KÇL, İntersubband geçiş, Dalga fonksiyonu mühendisliği.

Acknowledgements

I would like to thank my supervisor Prof. Dr. Ekmel Özbay and my co-supervisor Dr. Bayram Bütün. They provided me with invaluable guidance, suggestions and motivation during this work. Indeed I am thankful to Dr. Bayram Bütün for his patience and for being willing to discuss the problems arising from my life and research.

I would also like to thank Prof. Dr. Vakur B. Ertürk and Prof. Dr. Hamza Kurt for being on my thesis committee and evaluating my thesis.

This work would not be possible without good colleagues and friends. First, I would also thank all the past and present members of the NANOTAM. Especially, I would like to thank Doğan Yılmaz and Gökhan Mehmetoğlu for their friendships, their invaluable support and work for this thesis. I would also like to thank NANOTAM opto-electronic team; Dr. Deniz Çalışkan, Deniz Gülcü, Ramazan Özsoy, Tolga Şenol and Okan Ateşal.

Also I want to thank present and past members of Demir research group, where I have started doing science. Especially, I would like to thank Can Uran and Shahab Akhavan from whom I have learned my basic lab skills.

Finally, I would like to thank my family, my grandmother Şükran, my grandfather Abuzer, my mother Zerrin, my father İsmail, my uncle Erkan and my cousin Hakkı for their love, support and encouragement.

Contents

List of Figures

List of Tables

Chapter 1

Introduction

Laser (Light Amplification by Stimulated Emission of Radiation) devices are very important light sources and they have found various applications. Lasers are optical oscillators and they consist of two parts; optical amplifier and optical feedback element. Amplification is provided by stimulated emission and optical feedback is achieved by optical resonators (cavities). Semiconductor lasers are widely used and commercialized for violet to near-infrared spectrum. However it is very hard to achieve longer wavelengths such as mid-, far-infrared and terahertz with conventional semiconductor lasers.

The quantum cascade laser technology can completely satisfy the requirement of long wavelength semiconductor laser source. Quantum cascade lasers are based intersubband electron transition instead of electron-hole recombination as conventional semiconductor lasers do. Since intersubband transition energy is independent of material band gap, and it can be engineered by changing material thickness, essentially any wavelength can be obtained by quantum cascade lasers

1.1. Mid-Infrared Applications

Coherent mid-infrared source has found large number of applications;

Chemical spectroscopy and environmental monitoring: Most chemical molecules have special absorptions fingerprints in mid-infrared spectrum because of their chemical bonding vibrational transition in mid-infrared. Therefore mid-infrared lasers can be used as spectroscopy source and environmental monitoring. Graphical representation of the location of absorptions of some molecules in infrared spectrum is presented in Figure 1.1 (a).

Free space communication: Since water vapor does not have absorption in mid-infrared, atmosphere is almost transparent for mid-infrared light. Therefore mid-infrared lasers can be used for long range free space communication and light detection and ranging (LIDAR).

Infrared countermeasure: It is important military application. It is possible to confuse heat-seeking missiles guidance systems by mid-infrared source in order to protect aircrafts. Illustration of infrared countermeasures of an aircraft is presented in Figure 1.1 (b).

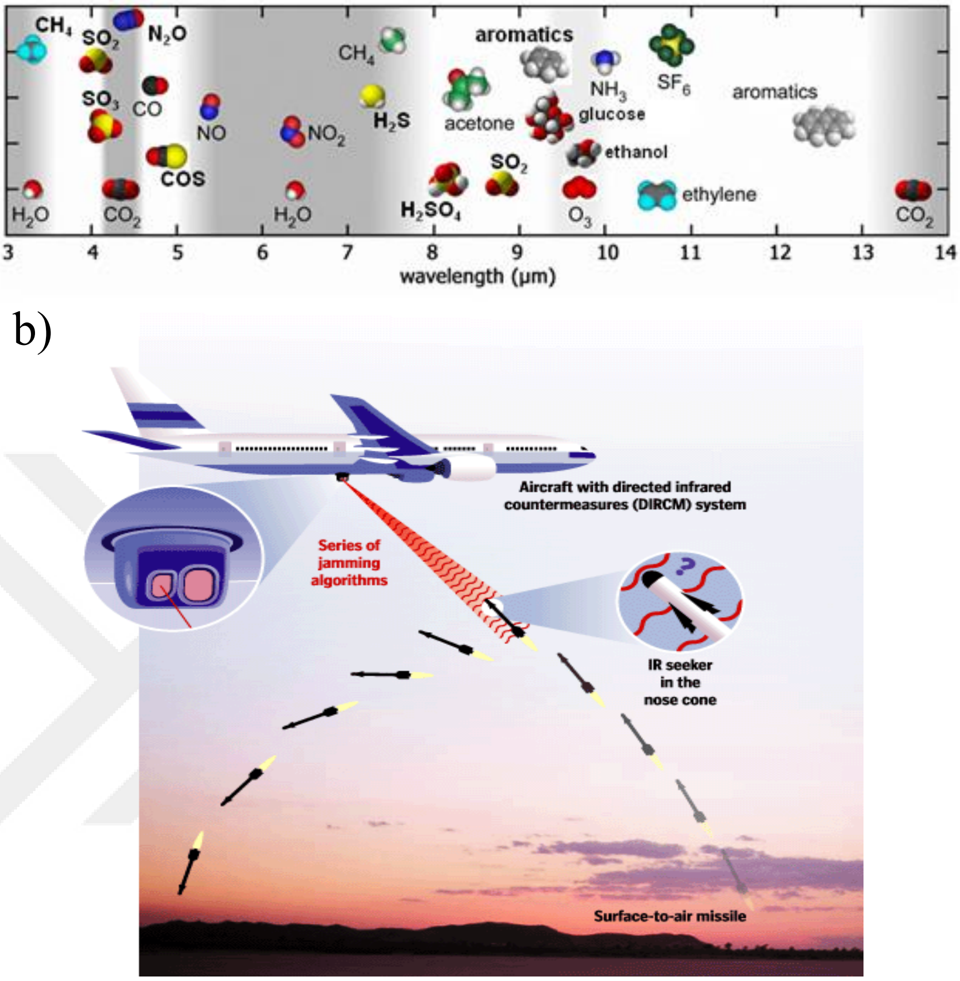

Figure 1.1 Figure 1.1 a) Graphical representation of the location of strong absorptions of molecules [1] b) Illustration of infrared countermeasures of an aircraft [2].

1.2. Mid-Infrared Sources

A schematic comparison of various mid-infrared laser sources is presented in Figure 1.2 [3].

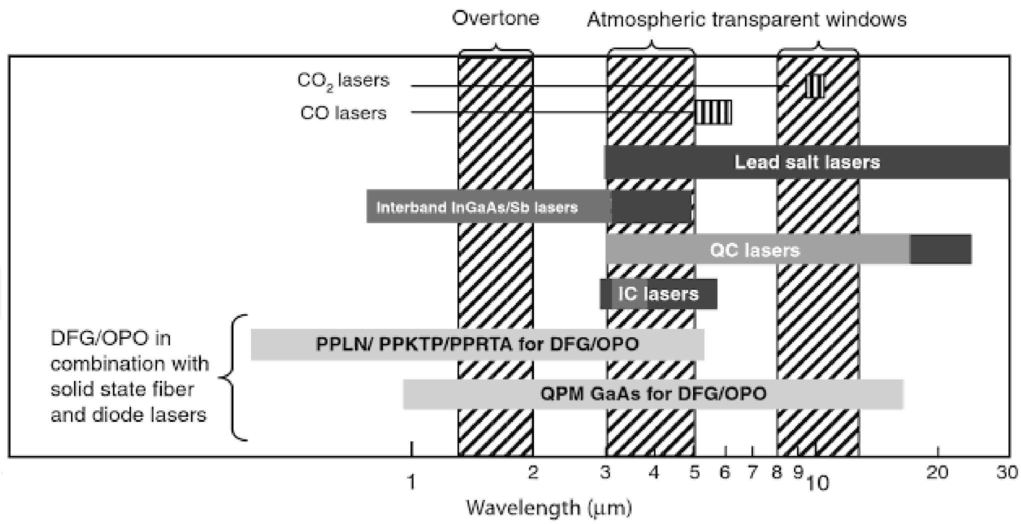

Figure 1.2 Schematic comparison of various mid-infrared laser sources [3].

CO and CO_2 lasers can be mid-infrared laser sources but their emission wavelength is fixed and tunability is not possible, also they are expensive and bulky. Fiber lasers are being used for non-linear down conversion to produce mid-infrared laser light but this technique is very complex and expensive. Conventional semiconductor lasers based on GaInSb/InAlSb or AlSb material can be used as mid-infrared laser sources but they operate at cryogenic temperatures only. IV-VI lead salt lasers are also possible for mid-infrared laser source but it requires cryogenic temperatures for operation and its output power is very low. However quantum cascade lasers can operate at room temperature, their emission wavelength can be widely tunable with high optical power, they are not too expensive and complex; therefore they are very attractive for number of mid-infrared applications.

1.3. Intersubband Transitions and Quantum Cascade Lasers

The main difference between conventional semiconductor lasers and quantum cascade lasers is conventional semiconductor lasers based on electron transition between conduction band to valence band whereas quantum cascade lasers are unipolar devices, which means laser beam is generated by the electron transition in conduction band only. The realization of the quantum cascade devices requires nanometer accuracy epitaxial growth. Very thin and smooth quantum well structures are needed. When these quantum wells are thin below the de-Broglie wavelength of electrons in semiconductor, quantum states which are controlled by confinement are formed. Therefore it is possible to create upper and lower laser levels in conduction band with these thin quantum well structures.

The joint density of states is different for interband and intersubband transitions. Therefore optical behaviors of interband and intersubband transitions are very different. The joint density of states in interband transition is characterized by electron and hole distribution in conduction and valence band respectively. Therefore gain spectrum of interband transition is broadened naturally. In contrast, the joint density of states in intersubband transition is delta like [3], so transition is very similar to atomic systems. Gain spectrum is less broadened than interband transitions. Schematic illustration of optical transition and gain spectrum of intersubband and interband transitions are presented in Figure 1.3.

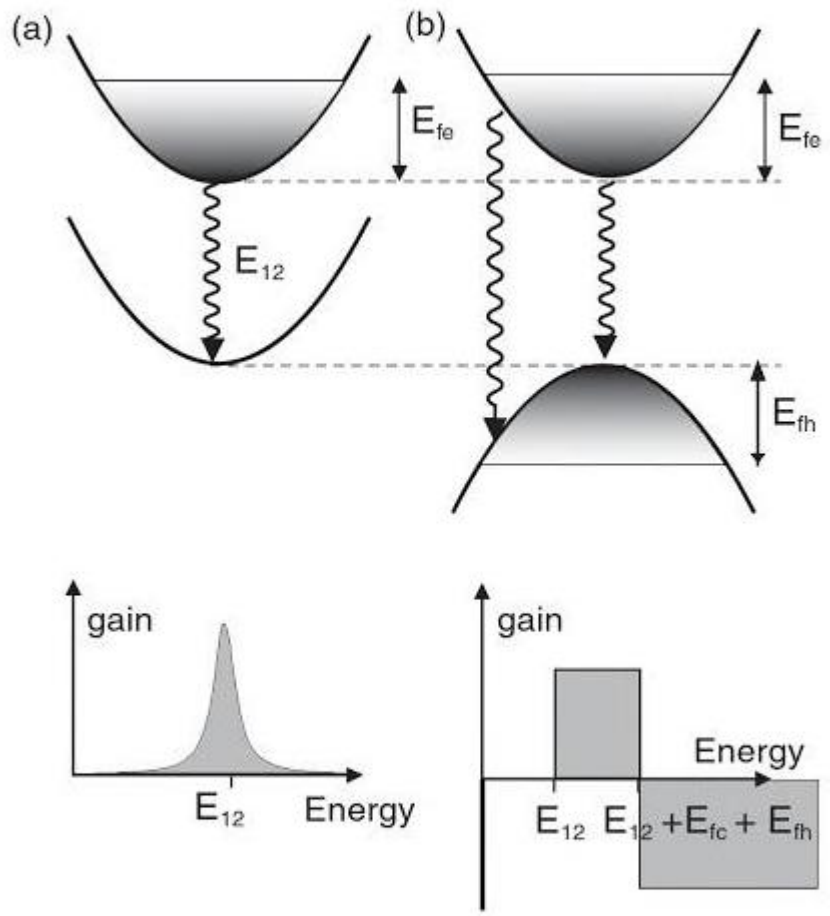

Figure 1.3 (a) Intersubband transition and gain spectrum, (b) interband transition and gain spectrum [3].

In 1971, Kazarinov and Suris [4] demonstrate that light amplification is possible with a transition between two intersubband states in a semiconductor. They demonstrate that electron can tunnel from the ground state of the quantum well to excited state of neighboring well by emitting photon, which process is called "photon assisted tunneling". Also this process can be repeated many times by cascading quantum wells. However, they could not achieve gain. Since when several quantum wells are cascaded (without doping), due to space charge domain formation, electric field cannot be uniform in the structure and structure become electrically unstable [5]. J.Faist and F.Capasso solved this electrical instability problem by adding injector regions (some of them are doped) between Kazarinov's and Suris's active region and they proposed first quantum cascade laser in 1994 [7]. These injector states behaves as if electron reservoir to prevent space charge domain formation and provide uniform electric field across the device.

Similar for all kind of laser systems, quantum cascade laser also consist of two parts; gain medium and optical resonator. Optical resonator can be simply formed by micro fabrication techniques and it is very similar to conventional semiconductor lasers. However gain medium of quantum cascade lasers are very different than conventional semiconductor lasers. It is possible to divide gain medium as active region where laser transition occurs and injection region where electron pumped to following active region.

Active region consists of thin quantum wells. Since these quantum wells are thin enough due to quantum confinement discrete energy levels are formed. These discrete energy levels are upper and lower laser states. Additionally laser wavelength can be controlled by changing the thickness of these quantum wells.

Injection region is a superlattice structure. As Esaki and Tsu [6] point out first that artificial miniband and minigap structures can be created by forming periodic quantum wells. Sequence of quantum well layers can behave as one dimensional crystal structure; they form artificial band and band gaps. This injection region pumps electron to upper laser levels and discharge electron from lower laser levels. They are used as to create cascade structure, in other words active regions can be combined by injection regions to create cascaded structure.

The first quantum cascade laser are made by J.Faist and F.Capasso in 1994 in Bell Labs [7]. It is operated at wavelength of 4.2 µm and it could lase only in pulse mode at cryogenic temperatures with 14 kA/cm^2. The very first quantum cascade laser gain medium band structure is presented in Figure 1.4. The active part consist of three coupled quantum wells, there is three level laser system in which population inversion between level 2 and 3 is obtained.

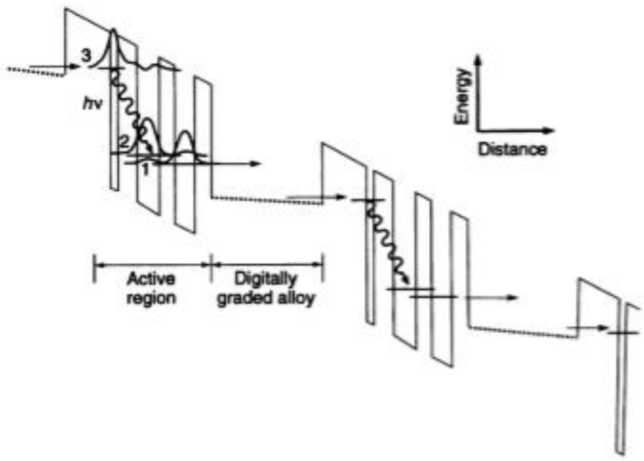

Figure 1.4 Conduction band energy diagram of the first quantum cascade laser and corresponding energy levels. Energy level 3 is upper laser level, 1 and 2 are lower laser levels. Active region is region where laser action takes place and digitally graded alloy is region that superlattice structure exists [7].

1.4. Material Systems

In this work InGaAs/AlInAs/InP material system is used to realize quantum cascade laser. However other heterostructures material systems (Figure 1.5) are also possible for quantum cascade lasers.

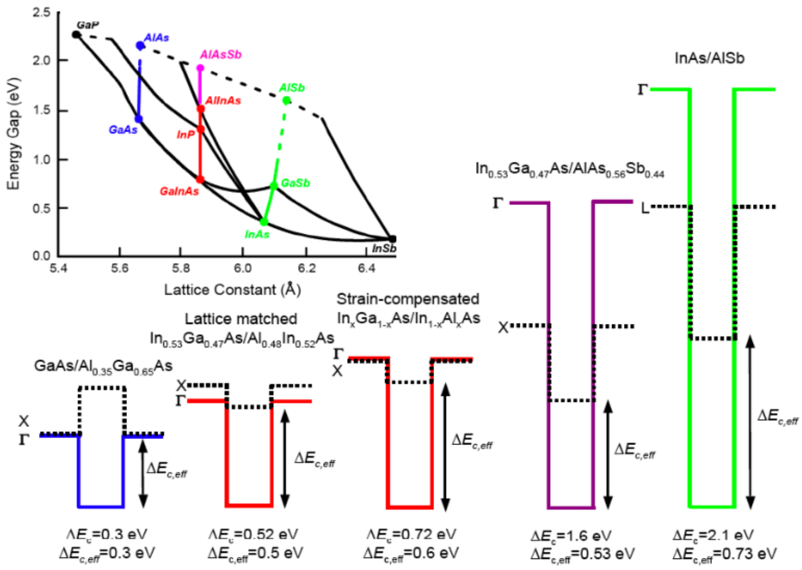

Figure 1.5 Conduction band and effective conduction band offset

Lattice matched InGaAs/AlInAs/InP material system has 0.52 eV band discontinuities, so it allows minimum 4.3 μm wavelengths. Furthermore, electron effective mass of InGaAs/AlInAs/InP material system is small ($m \approx 0.043m_0$) [15] almost half of the GaAs/AlGaAs material system, which allows to use larger quantum well width and make thickness fluctuations less critical (since optical matrix element inversely proportional to effective mass). Non-radiative relaxation time is also larger since $\tau \sim 1/\sqrt{m}$, therefore gain is larger than GaAs/AlGaAs material system, because gain is also inversely proportional to effective electron mass. Additionally refractive index of InP is less than InGaAs an InAlAs; hence forming cladding layer is also straightforward. It is also possible to increase conduction band discontinuity by strain compensation in order to obtain shorter wavelengths (minimum possible is 3.05 μm).

Due to higher electron effective mass comparing to InGaAs/AlInAs/InP material system, GaAs/AlGaAs material systems has lower gain. However GaAs/AlGaAs material systems has lower free-carrier losses (since free carrier loss is inversely proportional to electron effective mass). Therefore GaAs/AlGaAs material system is very promising for longer wavelengths especially THz lasers.

InAs/AlSb material system is very promising for short wavelength quantum cascade lasers and it has very low electron effective mass ($m \approx 0.023m_0$), so gain should be 2.5 times higher than InGaAs/AlInAs/InP material system [15]. However forming waveguide is very challenging because refractive index of active layer and cladding layers are the same. Also epitaxy growth of InAs/AlSb material systems is harder than InGaAs/AlInAs/InP material system.

There is also Si/SiGe material system for quantum cascade lasers but in this case laser transition occurs in valance band instead of conduction band. This material system is very promising for silicon-based integrated optic. However, there is no Si-based quantum cascade laser has been reported so far, intersubband electroluminescence was reported only in 2000 and 2002 [8,9].

1.5. Thesis Overview

The objective of this work is the developed quantum cascade laser which emits laser beam in between 4 μm to 5 μm wavelength and it must be operated above 50 mW optical power under 1% pulsed operation and it must be operated in continuous mode with minimum 5 mW optical power at room temperature.

This thesis organized as follows: in Chapter 2, the basic theory behind the quantum cascade laser is discussed. In particular, elementary quantum mechanics, formation of intersubband electronic states, radiative and non-radiative transitions are described. Theoretical backgrounds are explained to design quantum cascade laser, design methodology of quantum cascade lasers are mentioned, thermal and optical behavior of the quantum cascade lasers are analyzed and simulation results are presented.

In Chapter 3 overview of ridge waveguide fabrications process are presented in detail and fabrication development processes are mentioned. Different waveguide formation techniques are discussed and their effects on device performance are analyzed.

Chapter 4 covers characterization results of the fabricated quantum cascade laser are analyzed. Temperature dependent optical powers with different duty cycles and under different bias conditions are measured. Performance parameters; characteristic temperature, threshold current density and slope efficiencies are analyzed. Spectrum of laser is also measured at different temperatures and under different bias conditions.

Chapter 5 includes conclusion remarks and further works.

Chapter 2

Intersubband Laser Theory and Modeling

In this chapter, the essential background to design mid-infrared quantum cascade lasers is reviewed. Basic quantum mechanics including single quantum well solutions, coupled well systems, superlattice structures and intersubband electronic states are reviewed. Intersubband optical processes both radiative and nonradiative transitions are reviewed and their effects on device performance are discussed. Active region design parameters and conduction band engineering tools to design quantum cascade laser are presented. Macroscopic laser rate equations are derived for quantum cascade laser and performance parameters such as threshold current density and slope efficiency equations are obtained. Finally, thermal and optical design parameters are discussed.

2.1. Fundamentals

In this section fundamental quantum mechanics is reviewed to understand how quantum cascade laser works. Single quantum well solutions, coupled well systems, superlattice structures and intersubband electronic states are reviewed.

2.1.1. Single Quantum Well

Single quantum well problem is easy and a fundamental problem in quantum mechanics. Even if single quantum well problem is not used directly in quantum cascade laser design, it is a good starting point. In addition to that single quantum well problem is routinely used in some modern optoelectronic devices such as electro-absorption modulators and semiconductor interband lasers. The simplest form of single quantum well problem is one dimensional quantum well with infinite barriers. Consider particle with mass m with spatially varying potential V (z).

$$V(z) = \begin{Bmatrix} 0 \; if \; 0 \leq z \leq L_Z \\ \infty \quad otherwise \end{Bmatrix}, \tag{2.1}$$

where Lz is quantum well width. In order to solve this problem (time-independent) Schrödinger equation is solved and equate boundary conditions. Since energy is infinite at the edges of the quantum well, it is safely say, wavefunction is zero at the edges. So Schrödinger equation in the well is

$$-\frac{\hbar^2}{2m}\frac{d^2\Psi(z)}{dz^2} = E\Psi(z), \tag{2.2}$$

where $\Psi(z)$ is wavefunction, z is growth direction, E is energy eigenvalue and subject to the boundary conditions at the edges. Solution to (2.2) is simple

$$\Psi(z) = Asin(kz) + Bcos(kz), \tag{2.3}$$

where A and B are constants and according to boundary condition B=0 and k=$\sqrt{2mE/\hbar^2}$. Hence the solution of this equation is,

$$\Psi(z) = A_n sin\left(\frac{n\pi z}{L_z}\right), \tag{2.4}$$

Where A_n is normalization constant which is $\sqrt{2/L_z}$. Associated energies are

$$E_n = \frac{\hbar^2}{2m}\left(\frac{n\pi z}{L_z}\right)^2. \tag{2.5}$$

More realistic picture of single quantum well is finite barrier quantum well. In this case potential of outside is not infinite, it is finite and for simplicity it is constant. Let spatially varying potential V (z) as;

$$V(z) = \begin{Bmatrix} -Vb \quad if \quad -{L_z}/{2} \leq z \leq {L_z}/{2} \\ 0 \qquad otherwise \end{Bmatrix}. \tag{2.6}$$

In this case, it is known that nature of the solution in the outside the well is exponential and in the well solution is sinusoidal. Therefore wave function must be;

$$\Psi(z) = \begin{cases} Ge^{\kappa z},\ z \leq -{L_z}/{2} \\ Asin(kz) + Bcos(kz),\ -{L_z}/{2} \leq z \leq {L_z}/{2} < 0 \\ Ge^{-\kappa z},\ z \geq {L_z}/{2} \geq 0 \end{cases} \tag{2.7}$$

In this case solution is trivial after applying boundary conditions, which is continuity of wavefunction. However analytical solution is not possible, graphically wavefunctions and associated energy levels can be found [10].

2.1.2. Coupled Well Systems

The coupled well system can be considered as two finite quantum well coupled thought a barrier. This problem can be solved directly by calculating Hamiltonian of the whole system. However it requires cumbersome mathematical procedures. Instead of solving Hamiltonian directly, tight binding model is much more useful [11]. Perturbation theory, especially finite basis set approach can be used to approximate starting basis function [10]. Consider two infinite well as separately and define wavefunctions and potentials as $\Psi(z)_{right}$ and $V(z)_{right}$ for well on the right ,$\Psi(z)_{left}$ and $V(z)_{left}$ for left well. Let V(z) is the potential of the coupled system, which is $V(z) = V(z)_{left} + V(z)_{right}$.

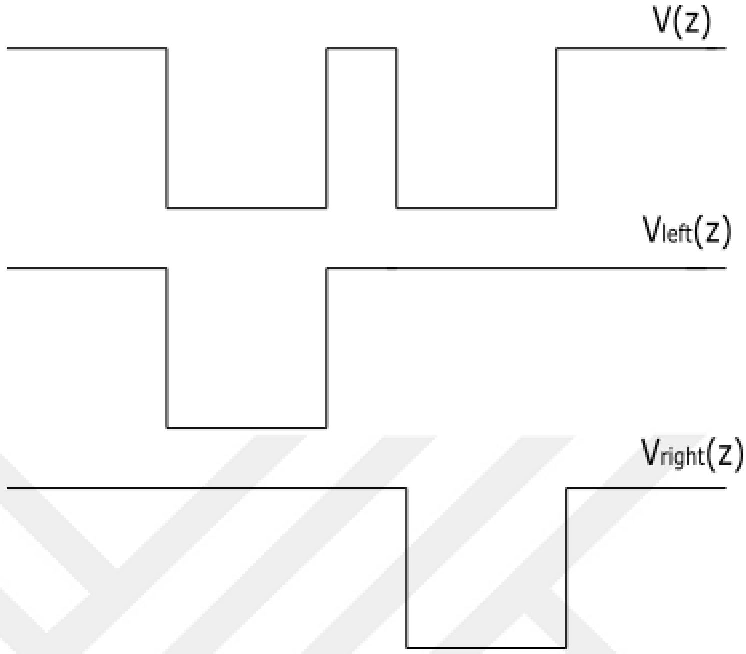

Figure 2.1 Illustration of coupled well system and two un-coupled wells.

Hamiltonian of this system is

$$\hat{H} = -\frac{\hbar^2}{2m}\frac{d^2}{dz^2} + V(z)_{left} + V(z)_{right}. \quad (2.8)$$

As long as barrier is reasonably thick, it can be approximated that wavefunctions in the wells are tightly combined, in other words, leakage of the wavefunction to adjacent well is negligible. With this approximation, wavefunctions are considered as approximately orthogonal and they can be used as basis for coupled system and wavefunction of the coupled system is:

$$\Psi(z) = A\Psi(z)_{left} + B\Psi(z)_{right}. \quad (2.9)$$

In the matrix form of finite basis approximation of coupled well Schrödinger equation is:

$$\begin{bmatrix} H_{11} & H_{12} \\ H_{21} & H_{22} \end{bmatrix} \begin{bmatrix} A \\ B \end{bmatrix} = E \begin{bmatrix} A \\ B \end{bmatrix}. \quad (2.10)$$

Hamiltonians can be given explicitly as;

$$H_{11} = \int \Psi(z)^*_{left} \left(-\frac{\hbar^2}{2m}\frac{d^2}{dz^2} + V(z)_{left} + V(z)_{right}\right) \Psi(z)_{left}, \quad (2.11)$$

and

$$H_{22} = \int \Psi(z)^*_{right} \left(-\frac{\hbar^2}{2m}\frac{d^2}{dz^2} + V(z)_{left} + V(z)_{right}\right) \Psi(z)_{right}. \quad (2.12)$$

Since we assume leakage of the wavefunction to adjacent well is negligible $H_{11} \approx E_1$ and $H_{22} \approx E_1$ where E_1 is associated ground energy of uncoupled well. However interaction of the wavefunction in the barrier cannot be completely negligible and this interaction appears in H_{21} and H_{12} terms, they are:

$$H_{21}{}^* = H_{12} = \int \Psi(z)^*_{left} \left(-\frac{\hbar^2}{2m}\frac{d^2}{dz^2}\right) \Psi(z)_{right}. \quad (2.13)$$

Additionally this Hamiltonians can be defines as splitting energy (ΔE).
With these assumptions and simplifications, matrix form of Schrödinger equation is:

$$\begin{bmatrix} E_1 & \Delta E \\ \Delta E^* & E_1 \end{bmatrix} \begin{bmatrix} A \\ B \end{bmatrix} = E \begin{bmatrix} A \\ B \end{bmatrix}. \quad (2.14)$$

In order to find energy eigenvalues, determinant of (2.14) should be zero;

$$\begin{vmatrix} E_1 - E & \Delta E \\ \Delta E^* & E_1 - E \end{vmatrix} = 0, \quad (2.15)$$

and obtaining eigenvalues;

$$E = E_1 \pm \Delta E, \quad (2.16)$$

and normalized wavefunctions are;

$$\Psi(z) = \sqrt{\frac{1}{2}}(\Psi(z)_{left} \pm \Psi(z)_{right}). \quad (2.17)$$

As given in Figure 2.1 wavefunction consists of symmetric and anti symmetric combinations of single quantum well solution. Since normalization constant is same for right and left, electron equally exist in both wells. These states are separated by energy difference of ΔE. Actually, this is a common phenomenon in quantum mechanics, it is mostly observed in solid-state physics; when two atoms are brought closer, they have a tendency to form energy bands of very closely spaced energy states rather than discrete energy levels. This phenomenon can also be observed when quantum wells are brought together; they form an artificial energy band, which kind of systems calls superlattice, which will be covered in detail in the next subsection.

2.1.3. Superlattice

As it is discussed in previous subsection, it is possible to create artificial band gaps by bringing quantum wells closely together. These structures are called superlattice. Suppose in the superlattice potential is

$$V(z) = \sum_{n=-\infty}^{\infty} V_w(z - nl). \tag{2.18}$$

where V_w is

$$V_w(z - nl) = \begin{cases} -Vb & if \quad |z - nl| \leq \mathrm{L_z}/2 \\ 0 & if \quad |z - nl| \geq \mathrm{L_z}/2 \end{cases}. \tag{2.19}$$

where n is an integer. As it is also understood from the potential definition, it is not possible to create such a potential in practice, since n spans minus infinity to infinity. However it is not too wrong to approximate as if it is infinite [10]. Wavefunctions in the well and in the barrier is:

$$\Psi(z) = \begin{cases} Ae^{\mathrm{ik_w(z-nl)}} + Be^{-\mathrm{ik_w(z-nl)}}, & |z - nl| < \mathrm{L_z}/2 \\ Ce^{\mathrm{ik_B(z-nl-\frac{l}{2})}} + De^{-\mathrm{ik_B(z-nl-\frac{l}{2})}}, & |z - nl| < \mathrm{h}/2 \end{cases}. \tag{2.20}$$

where Lz is quantum well width and h is barrier width.

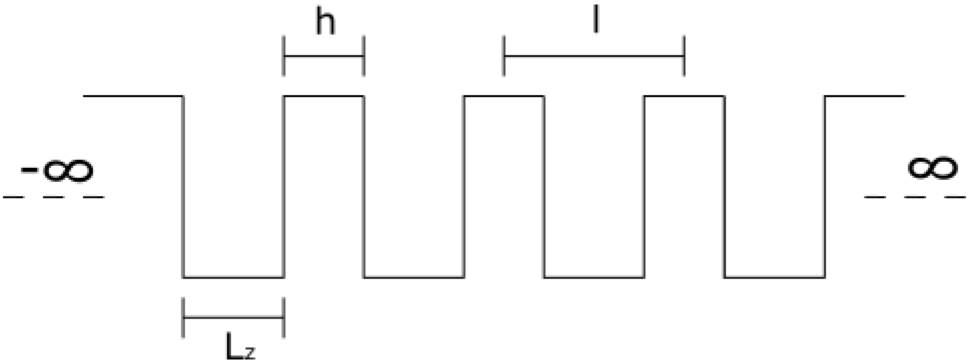

Figure 2.2 Illustration of superlattice potential.

Since structure is periodic, boundary conditions have to obey Bloch theorem that is

$$\Psi_q(z+nl) = \Psi_q(z)\mathrm{e}^{\mathrm{iqnl}}. \quad (2.21)$$

where l is periodicity and q is an integer. After applying boundary condition solution of this potential system is

$$\cos(ql) = \cos(\mathrm{k_w}L)\cos(\mathrm{k_B h}) - \frac{1}{2}\left(\frac{\mathrm{k_B}}{\mathrm{k_w}} - \frac{\mathrm{k_w}}{\mathrm{k_B}}\right)\sin(\mathrm{k_w L})\sin(\mathrm{k_B h}) \quad (2.22)$$

The (2.22) completely defines dispersion relation between q and energy, which is the origin of artificial energy bands [3]. This artificial energy bands are called mini-band and artificial energy gaps are called mini-gap in literature. It is possible to adjust energy levels of minigaps and minibands by just changing barrier and/or well thicknesses. Supperlattices are very useful in quantum cascade design especially injection/relaxation design. Because superlattice structure provide confinement for upper laser states whereas allow efficient tunneling for lower laser states.(This phenomena discuss in “Active Region Design” chapter in detail.)

2.2. Intersubband Electronic States

The quantum cascade lasers are composed of atomically abrupt layers. Layers are composed of alternating materials that have different electron affinities. This electron affinity difference forms a sharp band edge difference, which creates quantum wells and barriers in conduction band. In addition since layer thicknesses are in the order of de Broglie wavelength, energy stares are quantized along to the growth direction (conventionally this direction is assigned as z direction).

The effective mass theorem and envelope function approximation is very useful to obtain wavefunctions and energy bands of that kind of structure. Indeed it is possible to solve this structure without any approximation such as its band can be solved by "ab inito" quantum chemistry method but such a computation is very time consuming and it will not add any significant correction to envelope approximation [3].

According to the effective mass theorem, envelope function approximation, and because of in-plane (x and y directions) translational invariance wavefunction of the electron in this structure can be written in cylindrical coordinates as;

$$\Psi(z) = F(r)U_{n,0}(r). \tag{2.23}$$

where F(r) is the envelope function and satisfies the effective mass equation and $U_{n,0}$ is Bloch function (n is index of considered band).

In addition a few approximations are made: envelope function is varying slowly compared to Bloch function, envelope function can be expressed as linear combination of other functions and Bloch function is identical in all layers. According to these assumptions and in-plane translational in variance, envelope function is;

$$F(r)_{n,k_{||}} = \frac{1}{\sqrt{S_{||}}} e^{ik_{||}r_{||}} \mathrm{X}(z)_n. \tag{2.24}$$

where $S_{||}$ is the normalization area, $k_{||}$ is in plane wavevector and $\chi(z)_n$ is n[th] wavevector. Hamiltonian of the system can be written in growth direction and assume that electron behaves as free particle in plane direction. First start with one-band model [12], in this model effective mass of electron just depends on conduction band (depends on bandgap only since Kane's energy is much higher than bandgap), which is also known as parabolic effective mass model. In this model we ignore valence bands effects on effective mass. Hamiltonian according to this model is;

$$\hat{H} = \left[-\frac{\hbar^2}{2m(z)}\frac{d^2}{dz^2} + V(z)\right]\chi(z)_n. \tag{2.25}$$

and corresponding Schrödinger equation is;

$$\left[-\frac{\hbar^2}{2m(z)}\frac{d^2}{dz^2} + V(z)\right]\chi(z)_n = E\chi(z)_n. \tag{2.26}$$

Note that effective mass is not position dependent in the same material in this model, however since material are different effective mass is also different in the wells and barriers. (2.26) can be solved easily with boundary conditions between interfaces (interface between material w and b for example);

$$\chi(z)_n^w = \chi(z)_n^b. \tag{2.27}$$

$$\frac{1}{m_w(z)}\frac{\partial\chi(z)_n^w}{\partial z} = \frac{1}{m_b(z)}\frac{\partial\chi(z)_n^b}{\partial z}. \tag{2.28}$$

The eigenvectors and eigenvalues of (2.26) with boundary conditions ((2.27) and (2.28)) are enough to characterize energy levels of quantum cascade lasers. However it is also possible to add valence bands effects on effective mass, this addition can be based on k-p theory [11], which includes eight band model; conduction band, light and heavy hole, split of valence bands and their spins.

However correction on effective mass (nonparabolicity effect) can be made much easier way based on empirical two-band model [13], which assumes valence band is only one band and calculate interaction between conduction band to calculate effective mass. According to this model, effective mass is energy dependent and effective mass is [14];

$$m(E) = m\left[1 + \frac{2m\gamma(E-E_C)}{\hbar^2}\right]. \tag{2.29}$$

where m is effective mass from one-band model, E_c is conduction band energy, E is corresponding band energy and γ is nonparabolicity parameter. After this correction to effective mass, conduction band is not parabolic, nonparabolic, and *E*-*k* relation is

$$E_c(k) = E_c(0) + \frac{\hbar^2 k^2}{2m(E,z)}\,. \tag{2.30}$$

This correction does not add any complexity to our first model ((2.26)), only effective mass term changes. We consider one-band model again but considering valence band effect on effective mass and effective mass becomes energy dependent, this model is called effective one band model in literature[15].

There are additional factors affect the accuracy of energy states in quantum cascade lasers, which are space charge effect and electron-electron interaction due to high doping (Hartree potential). In the quantum cascade structure different energy states contain different electron population, which forms electrostatic potential that affect band profile. This can be easily modeled with Poisson equation [16]. Schrödinger equation (2.26) and Poisson equation are solved iteratively to obtain more accurate solution. Since electron density in quantum cascade lasers are low (generally about 10^{16} cm^{-2}), space-charge effect is negligible and such an iterative solution is unnecessary [17]. Electron-electron interaction can be considering with Hartree potential. This can be modeled as adding potential to Hamiltonian (2.25) and solve this new Hamiltonian and

Poisson equation iteratively [3]. However since electron density is low, this correction is also ignorable.

2.3. Intersubband Transitions

Radiative and nonradiative transitions result intersubband laser phenomena. As it is well known in order to make a laser gain medium is required. Optical gain in quantum cascade laser provided by stimulated emission between intersubband electronic states, and electron movement through the device is provided by nonradiative transition.

2.3.1. Interaction Hamiltonian

Interaction between light and electron can be modeled by defining perturbation Hamiltonian. Optical field is strong enough to change electron occurrence probability in quantum states but it is not strong enough to create new states, therefore perturbation theory can be used to model optical interaction. [10] Hamiltonian with optical field can be written as;

$$\hat{\mathrm{H}} = \hat{\mathrm{H}}_0 + \hat{\mathrm{H}}_{\mathrm{int}}. \tag{2.31}$$

where $\hat{\mathrm{H}}_0$ is Hamiltonian of current state and $\hat{\mathrm{H}}_{\mathrm{int}}$ is perturbation Hamiltonian due to optical field. Interaction Hamiltonian can be derived from electromagnetic potential vector $\vec{A}$ as using coulomb gauge (or transverse gauge). Interaction Hamiltonian is;

$$\hat{\mathrm{H}}_{\mathrm{int}} = \frac{(\boldsymbol{p} - e\boldsymbol{A})^2}{2m}. \tag{2.32}$$

For low intensity magnitude square of A can be neglected so

$$\hat{\mathrm{H}}_{\mathrm{int}} = -\frac{e}{2m}\, A \cdot p. \qquad (2.33)$$

where m is effective mass, which can be effective mass from-one band model or effective one band model. It is also possible to write this term with full band k-p model, in this case interaction Hamiltonian remains same but perturbation term will changes. In our discussion we will continue with one band or effective one band model. After defining interaction Hamiltonian, a perturbation term is;

$$\langle \Psi(z)_i \big| \hat{\mathrm{H}}_{\mathrm{int}} \big| \Psi(z)_f \rangle = -\frac{e}{m} \langle \Psi(z)_i | A \cdot p | \Psi(z)_f \rangle. \qquad (2.34)$$

To make dipole approximation which assumes that light wavelength is too longer than wells dimensions so spatial dependency of A can be neglected in dot product, so perturbation term is:

$$\langle \Psi(z)_i \big| \hat{\mathrm{H}}_{\mathrm{int}} \big| \Psi(z)_f \rangle = -\frac{e}{m} A \langle \Psi(z)_i | p | \Psi(z)_f \rangle. \qquad (2.35)$$

The vector potential A can be expressed as electromagnetic wave. Let electromagnetic field is;

$$\vec{E} = E_0 \cos(kr - wt)\, (\hat{x} + \hat{y} + \hat{z}). \qquad (2.36)$$

So vector potential is;

$$A = \frac{iE_0}{2w} (\hat{x} + \hat{y} + \hat{z}) e^{i(kr - wt)} + C. \qquad (2.37)$$

Therefore perturbation term is;

$$\langle \Psi(z)_i \big| \hat{\mathrm{H}}_{\mathrm{int}} \big| \Psi(z)_f \rangle = -\frac{eE_0}{2mw} \langle \Psi(z)_i | (\hat{x} + \hat{y} + \hat{z}) \cdot p | \Psi(z)_f \rangle. \qquad (2.38)$$

This term is essential to calculate absorption or gain coefficient.

2.3.2. Selection Rule: The Origin of Polarization Behavior

Since quantum cascade laser emission based on intersubband electron relaxation, it has very unique property; stimulated emission (also absorption) is strongly polarized. If (2.28) is written explicitly (with using envelope approximation);

$$\langle \Psi(z)_i | (\hat{x}+\hat{y}+\hat{z}) \cdot p | \Psi(z)_f \rangle = (\hat{x}+\hat{y}+\hat{z}) \cdot \langle U_{i,0} | p | U_{f,0} \rangle \langle F(r)_{i,k_{||}} | F(r)_{f,k_{||}} \rangle + (\hat{x}+\hat{y}+\hat{z}) \cdot \langle U_{i,0} | U_{f,0} \rangle \langle F(r)_{i,k_{||}} | p | F(r)_{f,k_{||}} \rangle. \qquad (2.39)$$

where i and f is initial band final states of band indices, since initial and final envelope functions are orthogonal first term in (2.29) vanishes. In the second term Bloch function is unity so only last part remains;

$$\langle F(r)_{i,k_{||}} | (\hat{x}+\hat{y}+\hat{z}) \cdot p | F(r)_{f,k_{||}} \rangle = \langle F(r)_{i,k_{||}} \frac{1}{\sqrt{S_{||}}} e^{ik_{||}r_{||}} \chi(z)_i \left| \left(\hat{x} \cdot \widehat{p_x} + \hat{y} \cdot \widehat{p_y} + \hat{z} \cdot \widehat{p_z} \right) \right| \frac{1}{\sqrt{S_{||}}} e^{ik_{||}r_{||}} \chi(z)_f \rangle. \qquad (2.40)$$

Contribution of x and y direction vanish; only z component remains. Therefore electromagnetic field (electric field in our case) interacting intersubband energy levels and propagating in plane direction (either x or y direction) has to be in z direction (growth direction), which means electromagnetic field which couples to the intersubband energy levels has to be TM polarized.

2.3.3. Intersubband Radiative Transitions

It is conventional to begin with Fermi's golden rule to define transition rate between states. Transition rate from state $|i, k_{\parallel}{}^{i} >$ to $|f, k_{\parallel}{}^{f} >$ is

$$W_{if,k_{||}{}^{i}k_{||}{}^{f}} = \frac{2\pi}{\text{h}} \left|\langle \Psi(z)_i \middle| \hat{\text{H}}_{\text{int}} \middle| \Psi(z)_f \rangle\right|^2 \delta(\text{E}_\text{f}(k_{\parallel}{}^{f}) - \text{E}_\text{i}(k_{\parallel}{}^{i}) \pm \hbar\omega). \quad (2.41)$$

Since absorption coefficient can be written as [15]

$$\alpha(\hbar\omega) = \frac{\hbar\omega \text{W}_{\text{Tot}}}{S_{act}LI}. \quad (2.42)$$

where S_{act} is active area surface area, L is cavity length, I is light intensity and W_{Tot} is total absorption or gain. In order to find all possible transition between state *i* and *f*, we have to sum over all states in k-space. Therefore absorption coefficient can be written as [15].

$$\alpha(\hbar\omega) = \frac{2\pi\hbar\omega}{S_{act}LI} \sum_{\text{if}} \sum_{k_{||}{}^{i}k_{||}{}^{f}} \left|\langle \Psi(z)_i \middle| \hat{\text{H}}_{\text{int}} \middle| \Psi(z)_f \rangle\right|^2 \delta(\text{E}_\text{f}(k_{||}{}^{f}) - \text{E}_\text{i}(k_{||}{}^{i}) \pm \hbar\omega)(\text{f}_\text{i} - \text{f}_\text{f}) \quad (2.43)$$

where f_i and f_f are Fermi-Dirac distribution of electron in the states *i* and *f* respectively.

Equation (2.40) can be simplified according to selection rule and replace momentum matrix element with position matrix element with using commutation relation which is

$$\frac{\text{i}}{\hbar}[\text{H}_0, \text{z}] = \frac{\text{p}_\text{z}}{\text{m}^*}. \quad (2.44)$$

and absorption coefficient reads;

$$\alpha(\hbar\omega) = \frac{2(e\pi)^2}{\varepsilon_0 n \lambda_0 L S_{act}} \sum_{if} \left|z_{ij}\right|^2 \sum_{k_{||}{}^i k_{||}{}^f} \delta(E_f(k_{||}{}^f) - E_i(k_{||}{}^i) \pm \hbar\omega)(f_i - f_f). \quad (2.45)$$

Considering in-plane translational in variance (in-plane symmetry), sum over k space can be replace with an integral;

$$\alpha(\hbar\omega) = \frac{(e)^2}{\varepsilon_0 n \lambda_0 L} \sum_{if} \left|z_{ij}\right|^2 \int_0^\infty \delta(E_f - E_i \pm \hbar\omega)(f_i - f_f)\, k_{||} dk. \quad (2.46)$$

Due to scattering (because of lattice vibration, collisions, interface roughness etc.) delta function transition deviates. It can be replaced with Lorentzian line shape function with full width of half maximum γ [18], which is

$$\frac{\gamma/\pi}{(E_f - E_i \pm \hbar\omega)^2 + \gamma^2}. \quad (2.47)$$

Also replace Fermi-Dirac distribution with sheet carrier density n_i and n_f, absorption coefficient reads

$$\alpha(\hbar\omega) = \frac{2(\pi e)^2}{\varepsilon_0 n \lambda_0 L} (n_i - n_f) \frac{\gamma/\pi}{(E_f - E_i \pm \hbar\omega)^2 + \gamma^2} \left|z_{ij}\right|^2. \quad (2.48)$$

Since only the some part of optical mode overlaps with gain medium (especially active region of cascade structure). The gain must be multiplied with coefficient which defines overlap factor (Γ). Therefore absorption coefficient is;

$$\alpha(\hbar\omega) = \Gamma \frac{2(\pi e)^2}{\varepsilon_0 n \lambda_0 L} (n_i - n_f) \frac{\gamma/\pi}{(E_f - E_i \pm \hbar\omega)^2 + \gamma^2} \left|z_{ij}\right|^2. \quad (2.49)$$

2.4. Nonradiative Inter-subband and Intra-subband Transitions

Electron in the upper band can relax to lower bands through several processes. These processes do not have to be radiative; in fact non radiative processes are dominant in our cases. Electron can change its energy states with spontaneous emission, phonon emission, impurity scattering or electron-electron scattering.

Dominant relaxation process is optical phonon emission in inter/intra subband transitions. Hence it is better to think two situations separately; two subbands which are spaced by energy smaller or larger than optical phonon energy [3].

In the first case optical phonon emission is always possible since energy gap between states are larger than one optical phonon energy, and its lifetime in the order of picoseconds, which dominates relaxation process.

In the second case since energy gap between states are lower than one optical phonon energy; hence, optical phonon emission is forbidden. Therefore lifetime is determined by other processes. In fact second situation is avoidable for quantum cascade laser design except THz quantum cascade lasers. Because naturally desired stimulated emission energy is far larger than optical phonon energy (except THz emission), and energy gap between lower states are designed to be larger than optical phonon energy on purpose in order to increase injection and extraction efficiency.(This topic will be covered in Active region design section in detail.)

For inter or intra subband scattering rate can be expressed for any given Hamiltonian. The main difference between intra and inter subband scattering is; electron changes its band during intersubband process, while electrons stay in same band but changes k-state (wave vector) during intersubband scattering.

Intersubband scattering rate can be written as;

$$W_{inter} = \frac{2\pi}{\hbar}\sum_{\mathrm{kf}}\left|\langle\Psi(z)_{i,ki}\left|\hat{\mathrm{H}}_{\mathrm{int}}\right|\Psi(z)_{f,kf}\rangle\right|^2 \delta(\mathrm{E_f}(k_{||}{}^{f}) - \mathrm{E_i}(k_{||}{}^{i}) \pm \Delta\mathrm{E}). \quad (2.50)$$

where $\Psi(z)_{i,ki}$ is initial state and $\Psi(z)_{f,kf}$ is final state, ΔE is zero if scattering is elastic and non-zero if scattering is inelastic.

Intersubband scattering rate is;

$$W_{intra} = \frac{2\pi}{\hbar}\sum_{\mathrm{kf}}\left|\langle\Psi(z)_{i,ki}\left|\hat{\mathrm{H}}_{\mathrm{int}}\right|\Psi(z)_{i,kf}\rangle\right|^2 \delta(\mathrm{E_i}(k_{||}{}^{f}) - \mathrm{E_i}(k_{||}{}^{i}) \pm \Delta\mathrm{E}). \quad (2.51)$$

As it is a seen only wave vector changes after intersubband scattering. In addition it is possible to define energy broadening in terms of the scattering rates [19],

$$\Gamma_{inter} = W_{inter}\hbar, \quad (2.52)$$

and

$$\Gamma_{intra} = W_{intra}\hbar, \quad (2.53)$$

So total optical broadening due to inter and intra subband scattering is

$$\gamma = \frac{1}{2}(\Gamma_{inter} + \Gamma_{intra}). \quad (2.54)$$

2.4.1. Spontaneous Emission

Actually, spontaneous emission is not considered as scattering process for optoelectronic devices generally, because it is completely radiative process rather than nonradiative. However for intersubband optoelectronic devices, spontaneous emission hinders intersubband transition.

Since optical matrix element is not zero between laser upper and lower state, spontaneous emission between these states is inevitable. Fortunately spontaneous emission lifetime is an order of magnitude longer than stimulated emission. Typically spontaneous lifetime is about 60 ns [3].

Spontaneous emission rate is;

$$W_{spon} = \frac{e^2 n |z_{ij}|^2 E_{ij}{}^2}{3\pi c^3 \varepsilon_0 \hbar^4}. \qquad (2.55)$$

where n is refractive index, z_{ij} is optical matrix element, E_{ij} is energy difference between states and c is speed of light in vacuum. Since spontaneous emission rate is proportional to square of photon energy, spontaneous emission rate is very short for intersubband transition (spontaneous emission lifetime is in the order of nanosecond as a result). This very long lifetime comparing to nonradiative processes, their lifetime is picoseconds order, it is the reason why intersubband light emitting diodes are very inefficient.

2.4.2. Phonon Scattering

Phonon causes intersubband transitions and creates energy flow between the electronic states to crystal lattice. Essentially there are two types of phonons optical and acoustic. Optical phonon scattering mechanism is much more dominant than acoustic phonon scattering in intersubband transitions [3].

Optical phonon scattering mechanism can be outlined with following three assumptions; first assume that optical phonons' dispersion is too low so they can be considered as mono-energetic, second Frohlich Hamiltonian dominates phonon scattering and finally one-band model is used (ignore the effects of valence bands). Therefore optical phonon scattering rate with envelope function approximation is [3];

$$W_0 = \frac{m^* e^2 \omega_{LO}}{2\hbar^2 \varepsilon_{ef}} \sum_f \int_0^{2\pi} \frac{1}{Q} dQ \int dz \int d\grave{z}\, \chi(z)_i \chi(z)_f e^{-Q|z-\grave{z}|} \chi(\grave{z})_i \chi(\grave{z})_f. \qquad (2.56)$$

where $\chi(z)_i$ and $\chi(z)_f$ are envelope function, ε_{ef} is effective dielectric constant which is ;

$$\varepsilon_{ef}^{-1} = \varepsilon_{inf}^{-1} + \varepsilon_{st}^{-1}. \qquad (2.57)$$

where ε_{inf} is infrared dielectric function and ε_{st} is static dielectric function. After summation over all possible phonon modes (change $\sum_f \ldots$ term with $(n_{Lo} + 1)$ for emission and n_{Lo} for absorption) (2.56) becomes;

$$W_0^{abs} = \frac{m^* e^2 \omega_{LO}}{2\hbar^2 \varepsilon_{ef}} \; n_{Lo} \int_0^{2\pi} \frac{1}{Q} dQ \int dz \int d\grave{z}\, X(z)_i X(z)_f e^{-Q|z-\grave{z}|} X(\grave{z})_i X(\grave{z})_f \;, \qquad (2.58)$$

$$W_0^{em} = \frac{m^* e^2 \omega_{LO}}{2\hbar^2 \varepsilon_{ef}} (n_{Lo} + 1) \int_0^{2\pi} \frac{1}{Q} dQ \int dz \int d\grave{z}\, X(z)_i X(z)_f e^{-Q|z-\grave{z}|} X(\grave{z})_i X(\grave{z})_f \;. \qquad (2.59)$$

Since phonons are boson n_{Lo} have to obey Bose-Einstein statistics as;

$$n_{Lo} = \frac{1}{e^{\left(\frac{\hbar\omega_{LO}}{k_B T}\right)} - 1}. \qquad (2.60)$$

Also Q represents the magnitude of the difference between k_f and k_i in k-space. Explicitly;

$$Q = \sqrt{k_f^{\,2} + k_i^{\,2} - 2} k_f k_i \cos\theta. \qquad (2.61)$$

The physical meaning of Q is very fundamental and idea behind that is commonly used in quantum cascade laser design especially at lower laser level design. Graphical interpretation is represented in Figure 2.3. Due to parabolic dispersion, states of k_f and k_i stay on a circle of radius k_f or k_i.Therefore as it seen in Figure 2.3 , as energy between the states increases, distance between the states increases (Q increases), hence scattering rate decreases (lifetime increases).

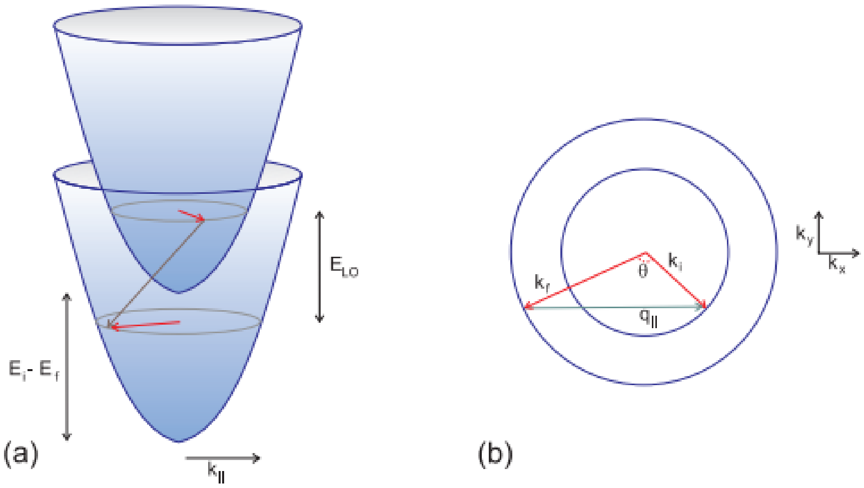

Figure 2.3 (a) Illustration of intersubband optical phonon scattering process.(b) In-plane reciprocal lattice space illustration of the initial and final electron wavevectors k_i and k_f and their vector difference [17].

This is very important result especially to design energy levels which are desired to have low lifetime. Since optical phonon scattering lifetime is in the order of picoseconds, if designing two energy states separated by one optical phonon energy, upper states lifetime is strongly reduced. This is commonly used quantum cascade laser design idea to enhance population inversion by reducing low level lifetime by optical phonon scattering.

There are also acoustic phonon scattering between inter and intra subband, same derivation as optical phonon scattering can make for acoustic phonon scattering rate calculation.[3] However acoustic phonon scattering lifetime is too long (about 400 ps), therefore it can be ignored for quantum cascade design [17].

2.4.3. Other Scattering Mechanisms

There are also other scattering mechanism between inter and intra subbands. Dominant scattering mechanism is optical phonon scattering, and other scattering mechanisms are ignorable when compared to optical phonon scattering lifetime.

Active region doping or doping regions close to active region leads to impurity scattering. However in quantum cascade laser design, it is avoidable to dope active region or region close to active region, typically doping of the active region is $10^{16}\ cm^{-3}$ intrinsically, which lead to 40 picoseconds impurity scattering lifetime [3].

Since quantum cascade laser structure have different layers whose alloy composition changes frequently, alloy scattering is inevitable. The scattering rate can be calculated according to Bastard’s work [20]. However alloy scattering is also very weak for InP based quantum cascade laser.

There is also electron-electron scattering in quantum cascade structures. In this process electrons exchange energy and momentum. After scattering, electrons may still stands on same energy state or change their energy bands. Dominant electron-electron scattering results to intersubband transition instead of intersubband transition. However in quantum cascade lasers typical electron-electron scattering lifetime is 45 picoseconds [3]. Therefore it is also ignorable for quantum cascade design when comparing very short optical phonon scattering lifetime.

Finally, since quantum cascade laser consists of many layers, an interface quality between these layers is very important. Roughness between layers causes interface roughness scattering. This scattering process differs other processes, interface roughness scattering strongly depends growth conditions. Lifetime of interface roughness scattering is ignorable or not when comparing to optical phonon scattering lifetime strongly depends on growth condition. Effects of interface roughness on scattering rate are modeled by Unuma in detail [21].

2.5. Quantum Cascade Laser Rate Equation

Up to now, quantum cascade laser is analyzed by quantum mechanics with microscopic properties. However some macroscopic quantities such as threshold current density and slope efficiency can be analyzed without having to quantum mechanics. These quantities can be derived in a very simple rate equation approach.

Consider simple rate equation analyses of a single active region only. Let active region have 3 energy states and assume that laser action happened in between state 3 and 2 and state 1 is just state that enhance relaxation of level 2. Also assume that there is injector state with constant population n_g. Schematic illustration of this system is presented in Figure 2.4.

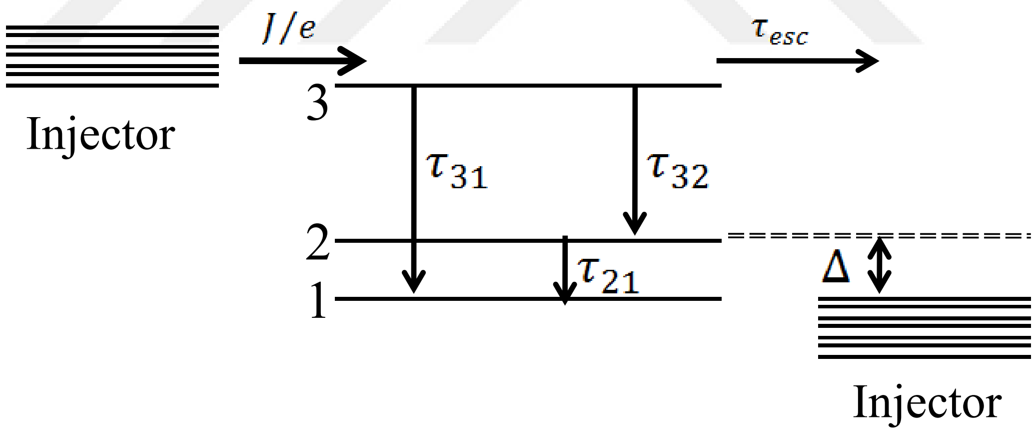

Figure 2.4 Rate equation model illustration

Before writing rate equations, some assumptions should be made;

1. Assume scattering from level 1 to injector is very fast, which means lifetime in level 1 is zero.
2. Electrons are injected in state 3 at rate J/e and injection is only through state 3, injection to state 2 is forbidden, which means injection efficiency is 100 %.
3. Injector consist of only one level with constant electron density n_g

4. Lifetime of state 3 is $\tau_3^{-1} = \tau_{32}^{-1} + \tau_{31}^{-1} + \tau_{esc}$, τ_{esc} is lifetime of electron escape process state 3 to continuum.
5. Assume electrons can thermally activated from injector to state 2 and thermally activated number of electrons at thermal equilibrium is n_2^{term}.

Rate equations for one active region period are;

$$\frac{dn_3}{dt} = \frac{J}{e} - \frac{n_3}{\tau_3} - Sg_c(n_3 - n_2), \tag{2.62}$$

$$\frac{dn_2}{dt} = \frac{n_3}{\tau_{32}} + Sg_c(n_3 - n_2) - \frac{(n_2 - n_2^{term})}{\tau_2}, \tag{2.63}$$

$$\frac{dS}{dt} = \frac{c_0}{n_r}\left[S(g_c(n_3 - n_2) - \alpha_{tot}) + \beta\frac{n_3}{\tau_{sp}}\right]. \tag{2.64}$$

where S is photon flux per period, g_c is gain cross section, α_{tot} is total modal loss and β is spontaneous emission overlap factor to laser mode.
n_2^{term} is ;

$$n_2^{term} = n_g e^{-\Delta kT}. \tag{2.65}$$

where Δ is energy difference between state 2 and Fermi level of injector region.
g_c is gain cross section which is;

$$g_c = \Gamma \frac{4\pi e^2}{\varepsilon_0 n \lambda_0 L}\frac{|z_{32}|^2}{2\gamma}. \tag{2.66}$$

where Γ is overlap factor, z_{32} is dipole matrix element L is length of period and γ is broadening of the laser transition.

Below threshold, to find steady state solution equates derivatives and S to zero and neglect spontaneous emission (since lifetime is too long) obtain;

$$\Delta n = (n_3 - n_2) = \frac{J\tau_3}{e}\left(1 - \frac{\tau_2}{\tau_{32}}\right) - n_2^{term}. \qquad (2.67)$$

and it is know that at the threshold modal gain is equal to the loss $g_c\Delta n$=α_{tot}
So threshold current is;

$$J_{th} = \left(e\,\frac{g_c}{\alpha_{tot}} + n_2^{term}\right)\frac{1}{\tau_3(1-\tau_2/\tau_{32})}\,, \qquad (2.68)$$

More explicitly;

$$J_{th} = \frac{1}{\tau_3(1-\tau_2/\tau_{32})}\left[\frac{\varepsilon_0 n \Lambda_0 L 2\gamma}{4\pi e^2 \Gamma |z_{32}|^2}\,\alpha_{tot} + e n_2^{term}\right]. \qquad (2.69)$$

Above the threshold to find steady state solution equate all derivatives ((2.62), (2.63) and (2.64)) to zero. Photon flux (S) is obtained as;

$$S = \frac{\left(J\left(\tau_3(1-\tau_2/\tau_{32})\right) - e\alpha_{tot}/g_c\right)}{e\alpha_{tot}(\tau_3(1-\tau_2/\tau_{32})+\tau_2)} = \frac{(J-J_{th})\tau_3(1-\tau_2/\tau_{32})}{e\alpha_{tot}(\tau_3(1-\tau_2/\tau_{32})+\tau_2)}\,. \qquad (2.70)$$

Also to obtain slope efficiency take derivative of S over J;

$$\frac{dS}{dJ} = \frac{\tau_3(1-\tau_2/\tau_{32})}{\alpha_{tot}(\tau_3(1-\tau_2/\tau_{32})+\tau_2)}. \qquad (2.71)$$

Therefore slope efficiency (derivative of optical output power over applied current to the device) of the device is;

$$\frac{dP}{dI} = N_p \hbar\omega \alpha_{f1}\frac{dS}{dJ}. \qquad (2.72)$$

where N_p is number of period of the device α_{f1} is front mirror loss.

2.6. Gain Medium Design and Modeling

The quantum cascade design has to overcome interrelated problems:

- Population inversion between upper and lower laser state has to be achieved
- Laser threshold gain has to overcome waveguide losses.
- Structure has to be electrically stable at bias point.

First demonstration of the quantum cascade laser that solved these problems is published in 1994 by J. Faist *et.al* milestone work [22].

Generally, in order to solve these problems quantum cascade laser structure are divided two parts; active region where laser action occurs and injection/relaxation region where electrons carried to following period of cascaded structure.

In simplest case, active region consist of at least three energy states; laser action occurs between third and second state, this model can be model with three level pumping schemes [23]. To satisfy population inversion, third energy level lifetime is adjusted to be longer then lower states' lifetime.

Injection/relaxation regions consist of minibands and minigaps, which is realized by sequence of alternating quantum wells and barriers. Main purpose of these regions is enabling resonant tunneling to deplete lower state and pumping adjacent upper state.

Also some layers of these regions are doped to serve as electron reservoir and to prevent arising space charge regions.

The most attractive feature of quantum cascade laser is cascading [3]. Active region and injection/relaxation region can be connected consecutively. Theoretically a single electron is able to stimulate number of photon in cascading process. Conduction band diagram of first quantum cascade laser is in Figure 2.5.

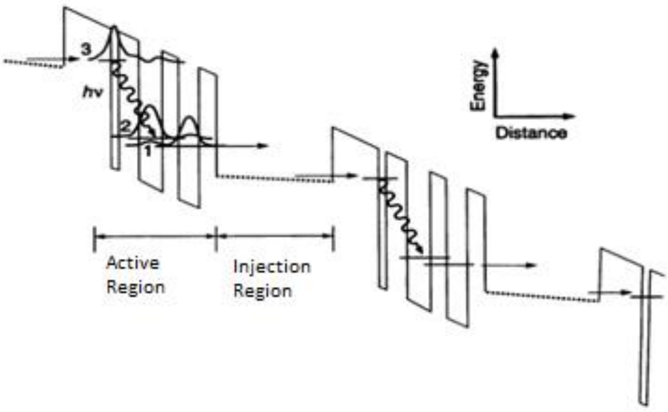

Figure 2.5 Conduction band diagram of first quantum cascade laser [7].

2.6.1. Active Region Design

Active region is the most important part of the quantum cascade laser, since entire laser action happened in this region. According to (2.69) and (2.71) high efficient and robust active region should have following properties:

- Long upper state lifetime
- Short lower state lifetime
- Low waveguide loss
- Narrow transition line width
- Large optical matrix element
- Low thermally activated electrons to fill lower states (low thermal backfilling)

As expected, it is not possible to satisfy all of these properties at the same time Upper state lifetime and optical matrix element is inversely correlated. In other words, in order to increase optical matrix element, spatial overlap between wave functions in upper and lower laser states have to be increased, however as spatial overlap between states increases, lifetime between states decreases. Therefore optimum value between lifetime and matrix element should be adjusted or designs should be made according to desired parameters (such as high power, operation mode and operation temperature).

For example, initial and final laser states do not have to be in same quantum well. It is possible to obtain lasing when initial and final laser states are localized in different wells [3]. If initial and final laser states are localized in same well, it is called vertical transition and if initial and final laser states are localized in different wells it is called diagonal transition. Comparison between vertical and diagonal transition is the best example to analyze inverse correlation of upper state lifetime and optical matrix element. Conduction band energy, corresponding wave function probability and calculated upper state lifetime and optical matrix element of vertical [24] and diagonal transition [3] example is presented in Figure 2.6. In diagonal transition design upper and lower laser states are spatially separated so optical matrix element is low while upper state life time is high yet in vertical design since wavefunctions of upper and lower laser states are spatially overlapped optical matrix element is high but upper state life time is low.

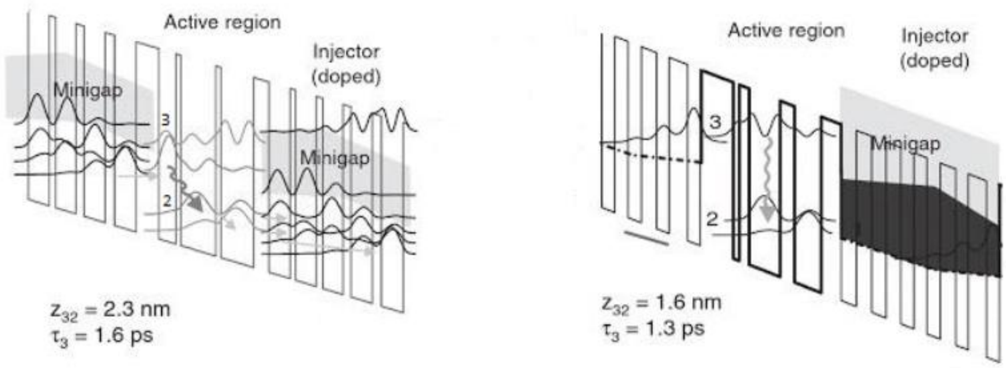

Figure 2.6 Vertical and diagonal transition comparison [3].

Whether the transition is either vertical or diagonal is determined by the thickness of the first well in active region. If the first quantum well thickness of active region is high, upper state in the first well get in resonance with upper state of the well in the middle and laser transition occurs between the upper state in the first well and lower state in the second well, which is also called photon assisted resonant tunneling. This phenomenon can explain working principle of diagonal transition quantum cascade lasers Figure 2.6. If the first quantum well thickness of active region is small, upper energy state in this well is above the upper energy state in the middle well therefore, resonance transition between this state is not possible; electron in the upper state of the first well, tunnels through the upper state of the second well and relaxes to the lower energy state in the second well, which is called vertical transition.

If wavefunctions are analyzed, for vertical transition, spatial overlap of upper and lower states' wavefunctions is very high, whereas for diagonal transition, their overlap is small, since upper and lower states of the laser is in different wells. Hence, vertical transition quantum cascade designs have much larger optical matrix element but their upper state lifetime is smaller as well.

Additionally, laser emission wavelength is adjusted by the well thickness of the middle well in the active region.

In order to ensure population inversion lower laser states should be emptied efficiently. To fulfill this requirement, additional energy level is formed below the lower laser state. As it is discussed before, an efficient reduction of lifetime can be obtained when energy difference between lower laser state and additional energy state is equal to one optical phonon energy. This energy difference can be adjusted by changing well thickness of last quantum well in active region.

To be more precise, without additional energy state below lower laser state, electron tunneling from lower state to relaxation region is a long time process, as a result; ensuring population inversion is hard to satisfy. Also it is very hard to adjust lower laser level and relaxation band energy levels are equal or close to each other (this is required to enhance tunneling). In order to overcome this problem additional energy level whose energy is one optical phonon energy below the lower laser state is formed. Therefore electrons in the lower laser state rapidly relax to the additional level and tunnel to the relaxation region, and this process is called "resonant optical phonon tunneling".

Also it is possible to form two additional energy levels below lower laser state. Again in this case energy difference between lower laser state and two additional energy levels should be equal to one optical phonon energy. That kind of design is called "double phonon resonance structure".

Double phonon resonance structure, of course, shortens the lifetime of lower laser state since additional relaxation path is defined; however, major advantage is increasing energy difference between relaxation region and lower laser state. This strongly reduces the thermal back filling effect and it is crucial for room temperature operation.

2.6.2. Injection Region Design

Simply injection/relaxation region is responsible for electron transfer between active regions. Optimum injection/relaxation region should have following features;

- High injection and extraction efficiency
- Increase upper level confinement and escape time from the upper state of the laser
- Provide electrical stability

To derive rate equations (2.62), (2.63) and (2.64), it is assumed that injection from injection state to upper laser level has unit efficiency and we ignore electron motion from injection state to lower laser state. However for more realistic picture, we should define efficiency coefficients and lower level transition. As shown in Figure 2.7 electron can tunnel from injection state to upper laser level and it can be tunnel to lower laser level by scattering processes. Of course tunneling through the lower laser level hinders the population inversion by increase electron number in lower laser state.

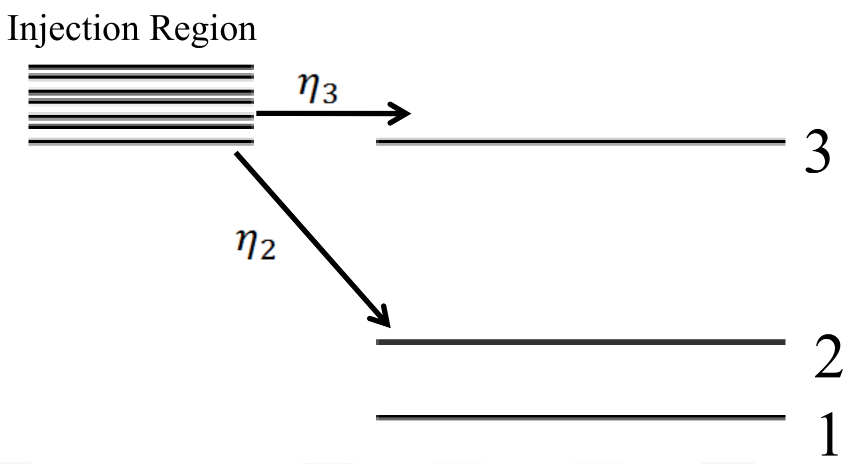

Figure 2.7 Illustration of electron transfer from injection region to active region.

We can modify the rate equation (2.67), and redefine population inversion with injection efficiency coefficients;

$$\Delta n = (n_3 - n_2) = \frac{J\tau_3\eta_3}{e}\left(1 - \frac{\tau_2}{\tau_{32}}\right) - n_2^{term} - \eta_2 n_2. \quad (2.73)$$

Obviously, for good injection design η_3 should be equal to one and η_2 should be equal to zero. These injection efficiency coefficients cannot be found by rate equation approach. Fully quantum mechanical calculations are required. Tight-binding density matrix approach can be used to find these coefficients. Detailed derivations and analyses about these coefficients can be found [25, 26, 27].

Another assumption made before, transition of electron in the upper laser level is only downward. However in reality electron in the upper laser level can make transition to continuum level and injector region without making laser transition. This phenomenon of course reduces the population inversion and hinders the quantum cascade laser performance.

Electrons in the upper laser state can escape to continuum level without contributing lasers transition with lifetime τ_{esc} which is called escape time. If escape time is not infinite, it reduces the upper laser state lifetime and hinders the laser performance. It is possible to prevent electron escape to continuum by increase the barrier thickness of the last barrier of active region but this also reduce the relaxation efficiency of the lower laser level, which is not desirable. To overcome this problem, upper laser state should be confined with barrier whereas lower laser states are not confined even their escape rate should be encouraged. The solution of this contradiction is forming minigaps and minibands in the injection/relaxation region. Adjust the minigap energy to increase upper laser state confinement while adjust the minibands according to lower laser states to allow electron escape. In other words minibands/minigap design should block the upper state escape whereas it should allow the lower sate escape.

Schematic illustration of minibands/minigap design idea is presented in Figure 2.8.

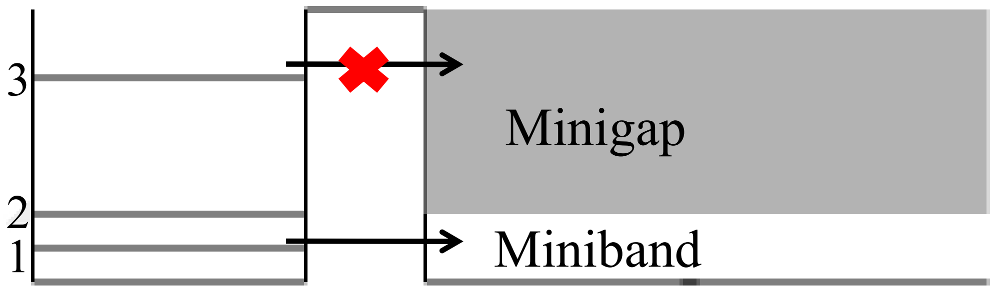

Figure 2.8 Minibands/minigap design logic illustration.

Minibands and minigaps are designed based on Bragg reflection condition [28]. Minibands and minigaps can be formed with superlattice structure. Number of period of superlattice directly determines the sharpness of minigap and minibands [3]. In other words escape time of both upper laser state and lower laser states are depends on number of period of the super lattice. Since as it is well known transition is completely depends on number of period in Bragg reflector. In Figure 2.9, sharpness and transition of superlattice with 3 and 5 number of period is presented [3].

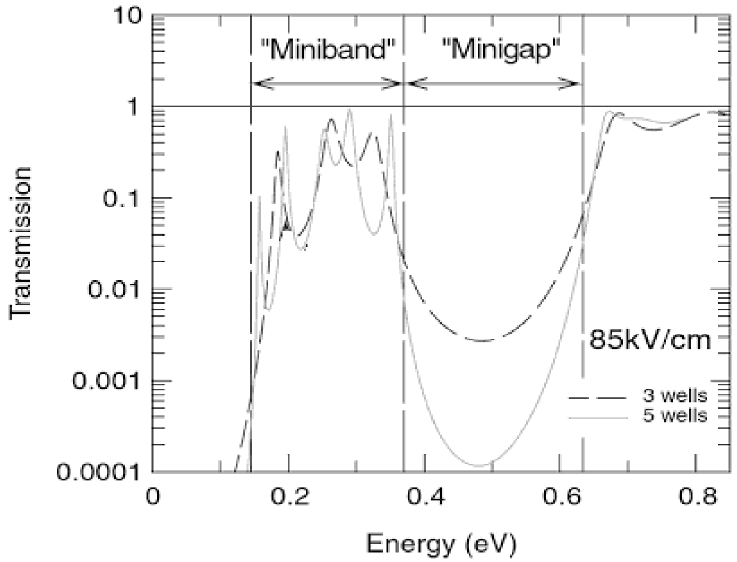

Figure 2.9 Computed transition of superlattice structure with 3 and 5 number of periods [3].

In addition, while superlattice designs, it should be noticed that escape time of electron in the lower laser state to the minibands should be shorter than phonon scattering time to ensure efficient population inversion.

Also good injection/relaxation design should provide electrical stability of the quantum cascade lasers. To fulfill this some portion of superlattice is doped. (Generally doped regions are placed as far as possible to the active region to prevent additional scattering). This doped layer prevents the formation of space charge regions by providing required electron charge for transport [3]. Also this region behaves as if electron source to feed the electrons to next cascade period, which enhance the electron motion and reduce ohmic resistance of the device as well.

2.6.3. Cascading

The most interesting feature of quantum cascade laser or more generally intersubband optoelectronic devices is cascading. In a quantum cascade laser the active region can be cascaded; hence the gain region can include number of periods. The advantages of cascading are obvious;

- As number of cascaded period is increased, entire gain of the quantum cascade laser is increases. Therefore for specific gain, required threshold current decreases as number of period increases.
- Theoretically, a single electron is able to emit number of period photon, which means as cascading period increase, slope efficiency of the device increases.
- As number of cascaded period is increased, it increases the overlap between active region and laser beam (increase the overlap coefficient Γ) which reduce the laser threshold current density and increase the slope efficiency as well.

However there is a cost of cascading, which is high bias voltage. As number of period increases, required applied electrical power to the laser operation increases. High operating power is problematic since it increases the heat generation (since quantum efficiency is not unity) and high temperature might be catastrophic for quantum cascade lasers. (Detailed temperature analyses will be covered in chapter 2.8.)

Therefore there is an optimum cascading number. For mid-infrared quantum cascade laser, optimum number of period is around 30 [29].

2.7. Active Layer Design and Modeling

Active region band structure and magnitude of relevant wavefunctions are presented in Figure 2.10. Active region (compose of 30 cascaded layers) was grown on low doped InP substrate (10^{18} cm^{-3}) and sandwiched between 35 nn thick InGaAs layers. Top cladding layer is 2.6 µm InP.

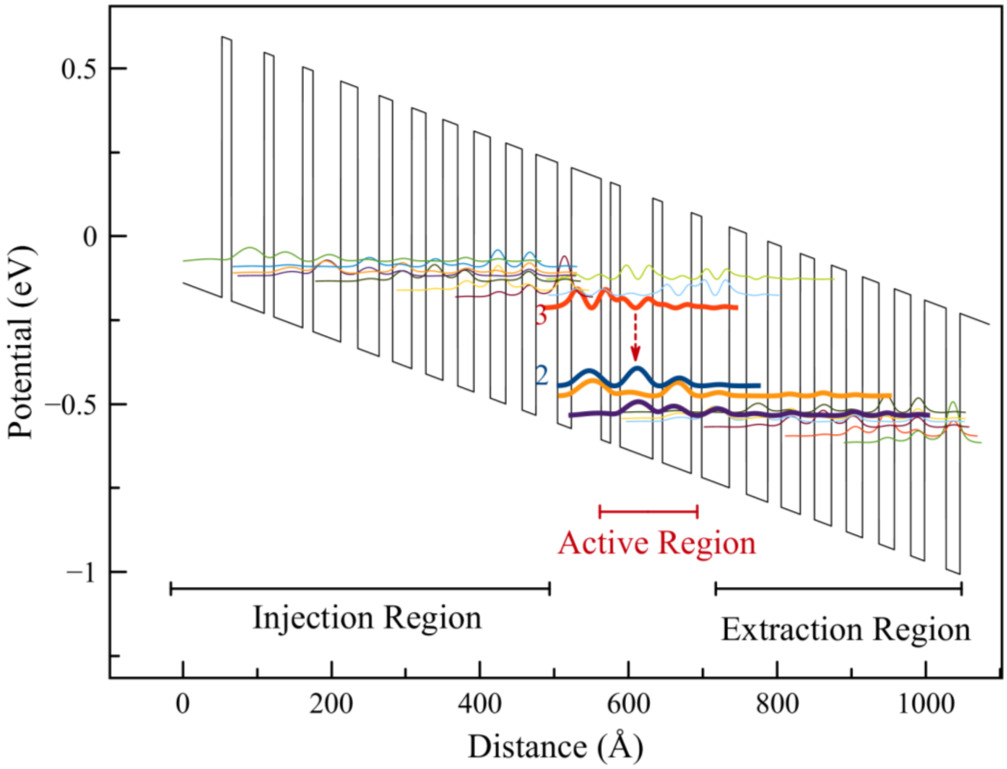

Figure 2.10 Band structure and moduli squared of corresponding wave function under an 83kV/cm electric field. Laser action happened between level 3 and level 2.

Active region based on $In_{0.572}Ga_{0.428}As/Al_{0.52}Ga_{0.48}As$ and $In_{0.53}Ga_{0.47}As/Al_{0.366}Ga_{0.634}As$ strain balanced material system and resulting net strain is -0.009%. Band structure and moduli squared of the corresponding wavefunctions for one period of cascaded layers under applied electric field of 83 kV/cm is presented in Figure 2.11. ErwinJr [33] is used to design active region and to calculate performance parameters. Laser action happens between level 3 and level 2. Energy difference between level 3 and level 2 is ~275 meV, corresponding wavelength is 4.5 µm. Laser transition is vertical since wavefunctions of level 3 and level 2 are spatially overlapped, corresponding dipole matrix element is 2.07 nm. Level 3 state lifetime is 2.22 ps and level 2 lifetime is 0.37 ps.

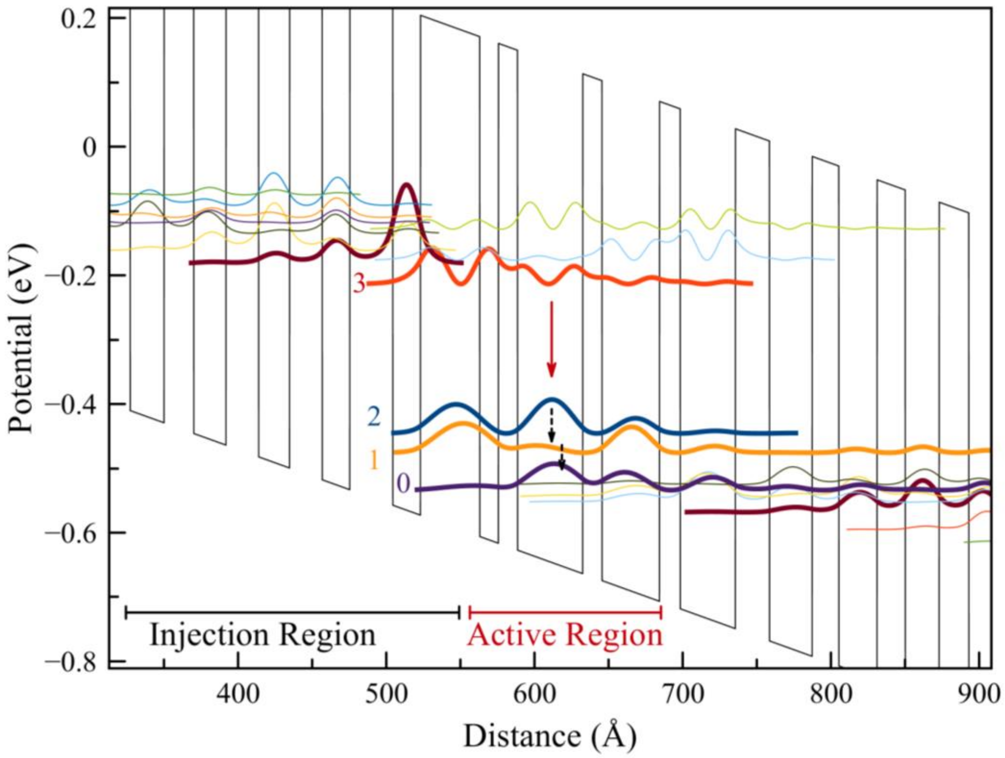

Figure 2.11 Band structure and moduli squared of the corresponding wavefunctions for one period of cascaded layers under applied electric field of 83 kV/cm. Laser action occurs between level 3 and level 2,red (solid) line indicates radiative transition. Electrons are relax from level 2 to level 1 and level 1 to level 0 by LO phonon scattering, black (dashed) arrow indicates non-radiative transition.

2.8. Thermal Design and Modeling

Since quantum cascade lasers' quantum efficiency is not unity and they operate under high bias conditions, they generate considerable amount of heat. Although comparing to the interband lasers, quantum cascade lasers show less temperature dependent broadening due to the atomic like joint density of state, temperature effects directly inter and intra subband scattering rates. Since the dominant scattering mechanism is optical phonons and they are bosons, they obey Bose-Einstein distribution, which means as temperature increases phonon population increases; hence inter and intra subband lifetimes reduce dramatically. This reduction decreases the population inversion and hinders the laser performance. In addition temperature increment also stimulates thermal back filling, which also reduce population inversion. Also as thermal energy increase thermally activated electrons can leakage to continuum, which also decrease the population inversion as well.

The self heating of active region can be modeled as

$$T_{act} = T_{sub} + R_{th} J_{op} w_{act} L V_{op}. \qquad (2.74)$$

where T_{act} is active region temperature, T_{sub} is substrate temperature, R_{th} is thermal resistance, J_{op} operating current density, w_{act} active region width, L is laser length and V_{op} is operating voltage.

Also it is possible to define threshold current density as a function of T_{act} ;

$$J_{th} = J_0 e^{T_{act}/T_0}. \qquad (2.75)$$

where J_0 is threshold current density at 0 K and T_0 is characteristic temperature which indicates how much threshold current depends active region temperature. Higher T_0 is desirable for high temperature and high duty cycle operation. T_0 is not only depends active region design but also depends waveguide design and device packaging.

The maximum active region temperature can be found, at the threshold maximum substrate temperature can be derived by setting $\frac{\partial T_{sub}}{\partial T_{act}} = 0$;

$$T_{sub,max} = T_0 \left[\ln \left(\frac{T_0}{R_{th} J_0 w_{act} L V_{th}} \right) - 1 \right]. \qquad (2.76)$$

So maximum active region temperature by empirical characteristic temperature coefficient is ;

$$T_{act} = T_0 \left[\ln \left(\frac{T_0}{R_{th} J_0 w_{act} L V_{th}} \right) - 1 \right] + R_{th} J_{op} w_{act} L V_{op}. \qquad (2.77)$$

Therefore to reduce active region temperature or keep active region temperature close to the substrate temperature;

- Characteristic temperature should be high
- Thermal resistance should be low
- Device dimensions (width and length) should be small
- Threshold current density should be low.

Threshold current density depends on active region design. Device dimensions are design parameters which determine maximum optical power. Characteristic temperature depends on both active region design and waveguide and packaging. Thermal resistance is also depends on waveguide design and packaging. In order to analyze effects of waveguide and packaging on device heat removal performance and in order to optimize waveguide and packaging design for better heat removal (make thermal resistance as low as possible) "COMSOL Multiphysics" is used.

In order to model thermal effects finite element software package of "COMSOL Multiphysics" is used. Basically software solves 2D heat transport equations in the quantum cascade structure. The generated heat in the active region is removed by convection, conduction and radiation [30]. Steady state heat transfer equations used in simulation are;

$$-\nabla\left(\begin{bmatrix} k_{th||} & 0 \\ 0 & k_{th\perp} \end{bmatrix} \nabla T\right) = Q, \tag{2.78}$$

$$\begin{bmatrix} k_{th||} & 0 \\ 0 & k_{th\perp} \end{bmatrix} \nabla T = h(T_{inf} - T) + \varepsilon\sigma(T_{surf}^4 - T^4), \tag{2.79}$$

where

$$\nabla T = \frac{\partial T}{\partial x}\,\hat{x} + \frac{\partial T}{\partial y}\,\hat{y}. \tag{2.80}$$

where k_{th} is thermal conductivity is heat source density (power(heat generated) per device volume), h is heat transfer coefficient (20 W/m^2 for our case), ε is emissivity of the surface (0.02 for our case), σ is the Stefan– Boltzmann constant, T_{inf} is temperature in the far-field and T_{surf} is the surface temperature [30].

Thermal conductivities used in simulation are given in Table 2.8.1 [30]. Since active region consist of thin quantum wells thermal conductivities are different along the growth direction and in plane direction at active region. Anisotropic thermal conductivity as a result of phonon scattering at the quantum well interfaces [31]. This interface scattering reduces thermal conductivity in the growth direction, in plane thermal conductivity is close to the bulk thermal conductivity but cross plane thermal conductivity is much less than bulk thermal conductivity.

Material	$\mathbf{k_{th}}$(W/m-K)
InP	74
$In_{0.57}Ga_{0.43}As$	5.84
Si_3N_4	15
SiO_2	1.3
Au	337
Cu	384
In Solder	93.6
Active Region	$k_{th\|\|}$=5.7 , $k_{th\perp}$ =1.1

Table 2.1 Thermal conductivities of materials used in the simulation

Note that thermal conductivities are temperature dependent but their dependencies are low enough to ignore at our simulation temperature range.

In addition, it is assumed that heat generation is in active region only; we ignore ohmic losses in cladding layers. Figure 2.12 presents simulation results of temperature mapping and heat flux on the front facet of quantum cascade laser device using Si_3N_4 or SiO_2 as passivation layer and different structures: either conventional ridge wave guide without gold top contact or conventional ridge wave guide with gold top contact and different mount option, either epi-up or epi-down. In all cases quantum cascade laser structure are mounted on copper plate with indium-indium soldering. Copper plate temperature is fixed at 283 K and air temperature is fixed at 300 K in the simulation. (In reality copper plate temperature fixed by thermo-electric cooler (TEC)). Dissipated electrical power in the active region is assumed as 19.375 W (peak optical power is achieved at 12.5 V and 1.5 A with 2mm X 20 µm device) in the simulation.

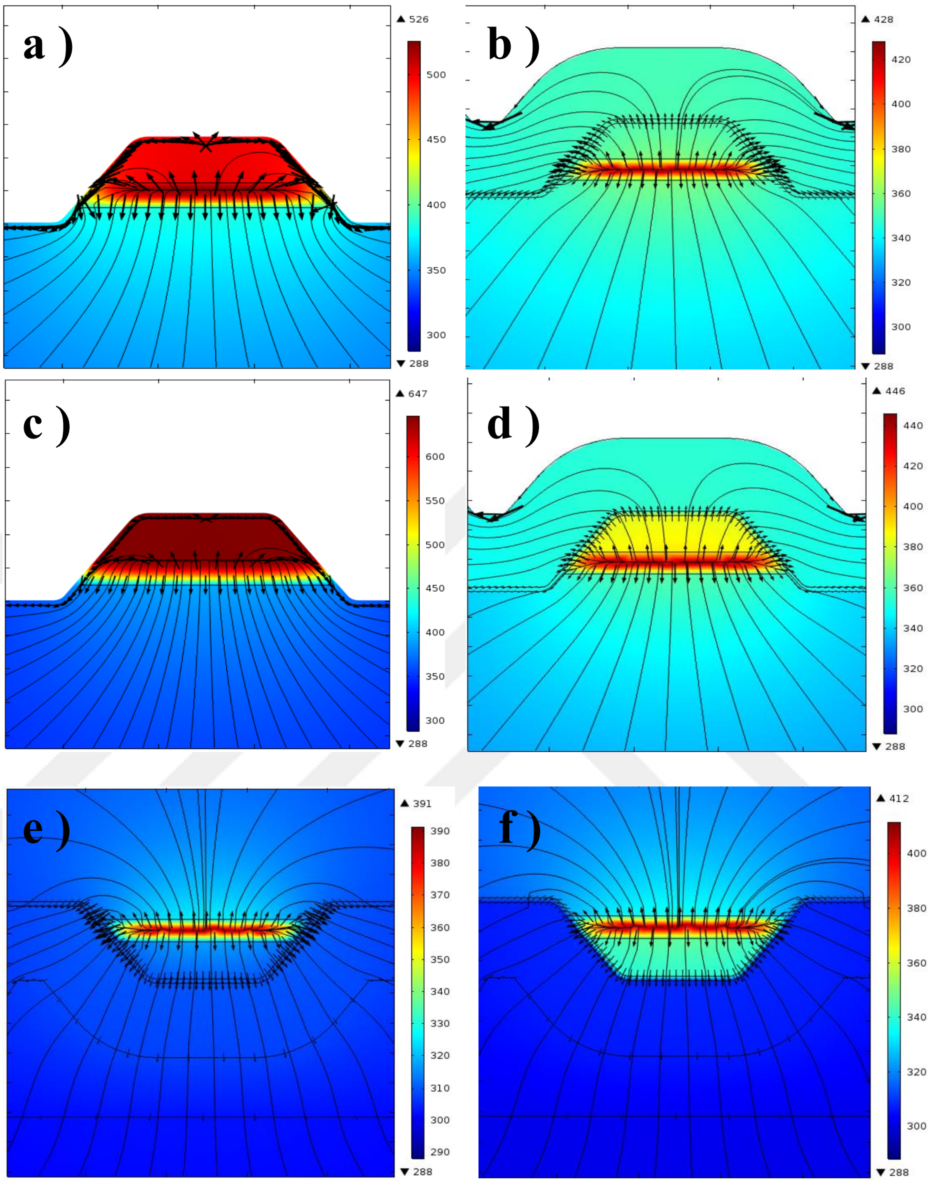

Figure 2.12 Total heat flux patterns and temperature distribution simulated for conventional ridge waveguide quantum cascade lasers (a) passivated with Si_3N_4 and without electroplated gold for epi-up bonding, and (b) passivated with Si_3N_4 and with 5 µm thick electroplated gold for epi-up bonding, (c) passivated with SiO_2 and without electroplated gold for epi-up bonding, (d) passivated with SiO_2 and with 5 µm thick electroplated gold for epi-up bonding, (e) passivated with Si_3N_4 and with 5 µm thick electroplated gold for epi-down bonding,(f) passivated with SiO_2 and with 5 µm thick electroplated gold for epi-down bonding

The heat flow is a vector quantity and its direction is represented by arrows and gradient lines. Temperature magnitudes are indicated by color. Since Si_3N_4 has one order of magnitude higher thermal conductivity than SiO_2, devices passivated with Si_3N_4 shows better heat removal performance. Additionally electroplated thick gold layer improve lateral heat removal performance significantly by spreading generated heat. Also mounting type effects heat removal performance directly. As it is seen, heat flow thought the growth direction therefore epi-down mounting both reduces the heat transfer path and since gold and indium have higher thermal conductivity than InP, improves the thermal conductance. Another option to improve heat performance of the quantum cascade laser is buried heterostructures, in this case iron doped InP is grown by MOCVD (metal organic chemical vapor deposition) as passivation layer instead of Si_3N_4 or SiO_2. Since InP has much higher thermal conductance, laser heat removal performance improves significantly. However, iron doped InP is very expensive process, it requires P-based MOCVD system which is not available for us.

2.9. Mid-Infrared Waveguides, Design and Modeling

Laser has to have two principle components: a gain medium and cavity resonator. The aim of resonator is provide optical feedback with minimum loss. In order to minimize required threshold current density, resonator should provide large optical overlap factor and should have low loss. The threshold condition of lasing is ;

$$g_{th}\,\Gamma = \alpha_w + \alpha_m. \tag{2.81}$$

where g_{th} is threshold gain, Γ is overlap (confinement) factor(overlap integral of cavity mode and gain medium), α_w is waveguide loss per length and $\alpha_m$is mirror loss. The waveguide loss is as a result of scattering and absorption in the waveguide and the reason of mirror loss is finite reflectivity of mirrors.

Mirror loss can be written as ;

$$\alpha_m = -\ln(\mathrm{R}_1\mathrm{R}_2)/2\mathrm{L}. \quad (2.82)$$

where L is length of cavity, R_1 is reflectivity of one face and R_2 is reflectivity of other face. Except threshold gain, other variables depend on waveguide design. Vertical cavity of quantum cascade laser is naturally present. Since active region is in between cladding layers and active region refractive index is higher than cladding layers' refractive index vertical confinement is achieved. The lateral confinement is generally realized by fabrication (etching).

The reason of the mirror loss is finite reflectivity of the mirrors. Fortunately since active region refractive index is much larger than air, mirrors can be realized by itself. At (InGaAs/AlGaAs)/air interface, R = 0.33, and for 2 mm long waveguide will have $\alpha_m \approx 5.54\ cm^{-1}$ according to (2.82). Is it possible to decrease mirror loss with high reflective coating on the back side of the laser. Coating laser facet (InGaAs/AlGaAs) with 100 nm Al_2O_3 and 100 nm Au provides almost unity reflectivity at 4.5 µm wavelength ($\mathrm{R}_{\mathrm{Al2O3/Au}} \approx 0.97$). With high reflectivity coating mirror loss of 2 mm long waveguide is $2.85 cm^{-1}$. FDTD simulation of reflectivity of Al_2O_3/Au coating presented in Figure 2.13.

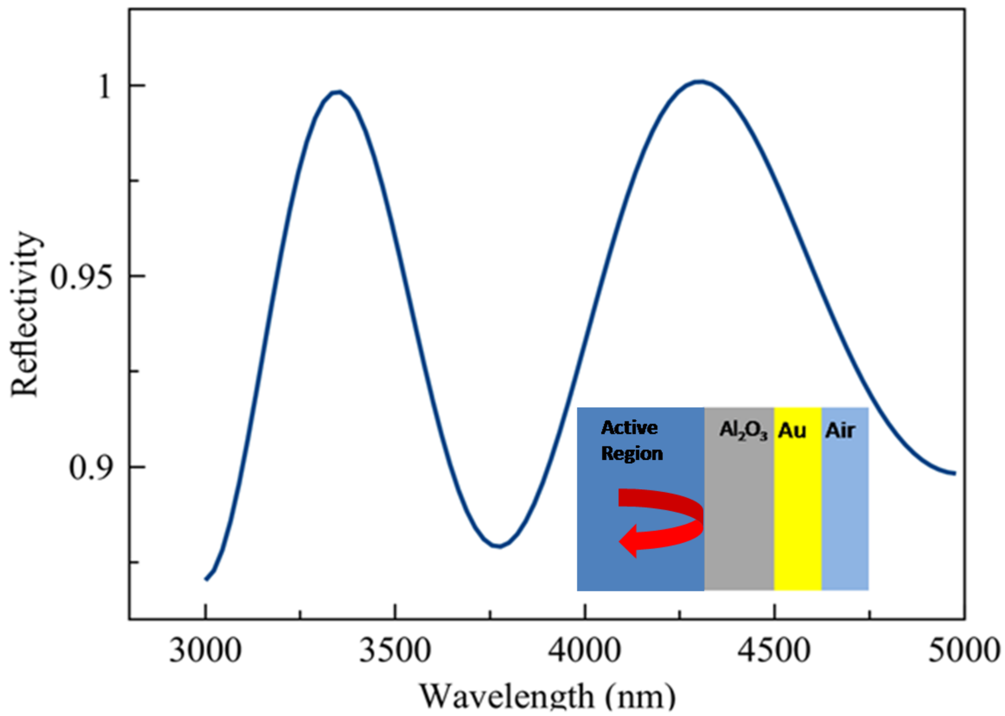

Figure 2.13 FDTD simulation (Lumerical) of reflectivity of Al_2O_3/Au (100 nm/100 nm) dielectric/metal stack

Free carrier absorption in the cladding layers leads to waveguide losses. The free carrier loss can be calculated from the Drude model which gives frequency dependent real and imaginary permittivity;

$$\varepsilon(\omega) = \varepsilon_b \left(1 - \frac{\omega_p^2 \tau^2}{1+(\omega\tau)^2} + j\frac{\omega_p^2 \tau}{\omega(1+(\omega\tau)^2)}\right). \qquad (2.83)$$

where ε_b is material permittivity without considering free carrier contribution, τ is Drude scattering time (momentum relaxation time) and ω_p is plasma frequency ;

$$\omega_p = \frac{ne^2}{\varepsilon_b m^*}. \qquad (2.84)$$

where n is free carrier density and m^* is effective mass of electron. Since Drude scattering time is long enough for mid infrared quantum cascade lasers, free carrier absorption can be written as [32] ;

$$\alpha_{fca} = \frac{ne^2\lambda^2}{4\pi^2 m^* c^3 \tau \varepsilon_0} \sqrt{\frac{\varepsilon_0}{\varepsilon_b}} . \tag{2.85}$$

It is observed that the absorption due to free carriers increases with carrier density, Drude scattering time and lasing wavelength.

However, in order to reduce ohmic losses of the device cladding layers are doped. To reduce ohmic losses while keep free carrier absorption low, waveguide vertical planning should be designed carefully. Highly doped cladding layer should be far enough to active region and it is separated from active region by undoped cladding layer. In addition, increasing optical confinement in the active region, reduces overlap between optical wave and cladding layer. Fabricated device waveguide design is presented in Figure 2.14.

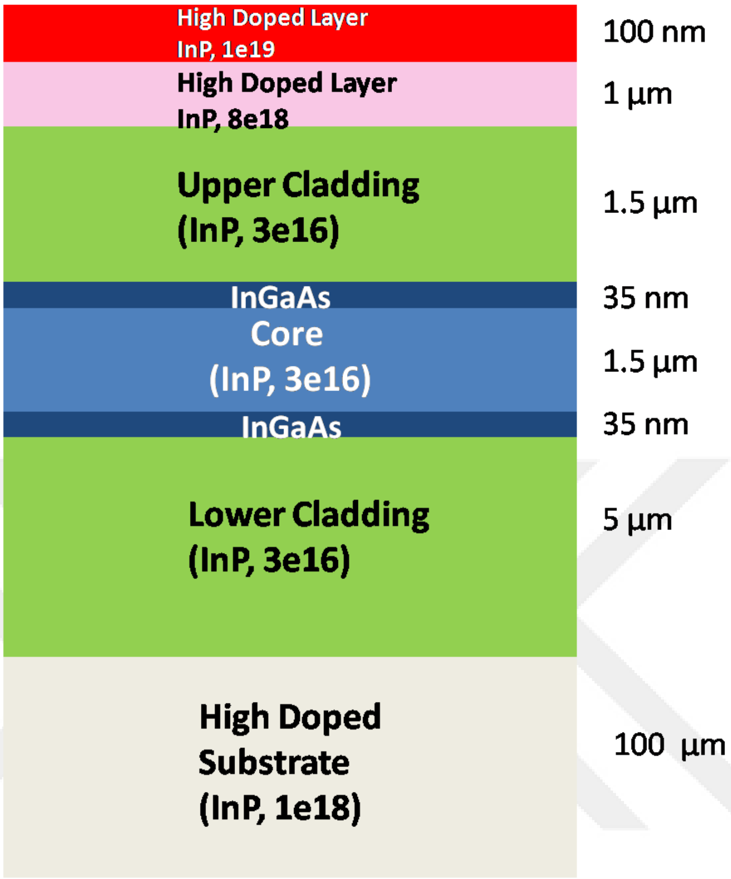

Figure 2.14 Waveguide design illustration of fabricated device

One dimensional mode solver is very practical tool to design vertical part of the waveguide and it is very useful to model optical confinement and absorption in the cladding layers. The one-dimensional mode solver approximation is reasonable since waveguide's vertical dimensions are much smaller than lateral dimensions. To analyze and design vertical confinement in the cavity and free carrier absorption losses ErwinJr [33] is used. A fundamental TM mode intensity and refractive index simulation of waveguide design through the growth direction is presented in Figure 2.15.

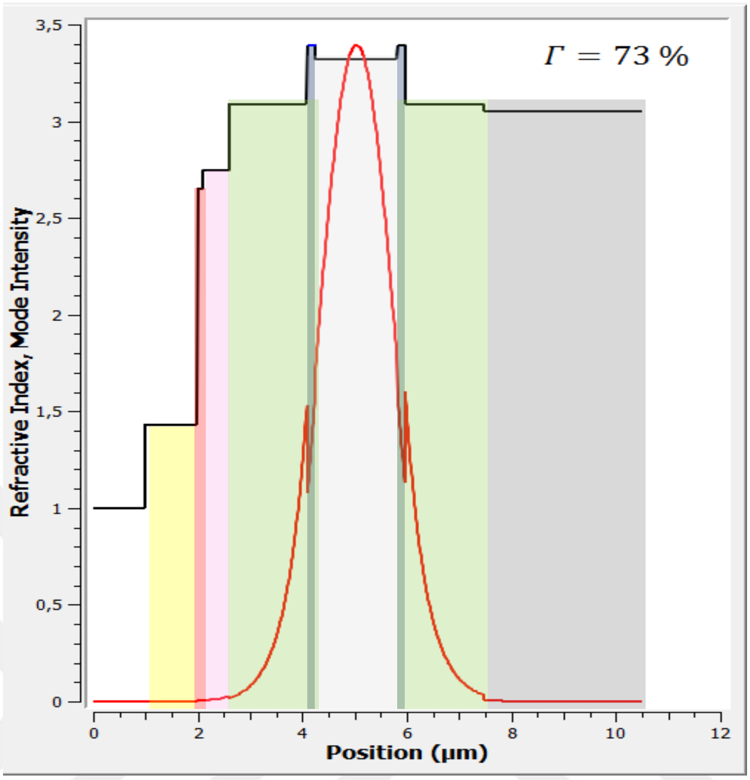

Figure 2.15 Fundamental TM mode intensity and refractive index of the vertical waveguide at 4.5 μm wavelength.

Other sources of waveguide loss are passivation layer absorption, plasmonic losses and scattering loss due to vertical side wall roughness. All of these are fabrication dependent loss mechanisms and they can be minimized by appropriate fabrication methods as well. Detailed analysis and works done to optimize these parameters will be discussed in the chapter 3. To realize both vertical and lateral absorption and optical confinement, 2D mode solver is used. ”Lumerical Mode Solver” is used to analyze 2D optical behavior of the waveguide. The simulation result of fundamental TM mode profile of 16 um width waveguide Lumerical FDTD model are shown in Figure 2.16. The simulated waveguide loss is 0.45cm^{-1}.

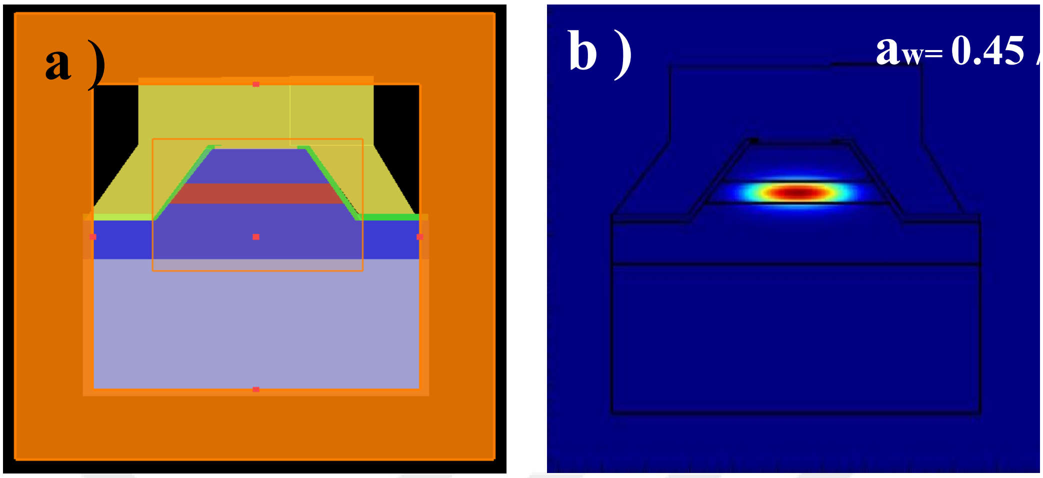

Figure 2.16 (a) Used FDTD model and (b) simulation result of fundamental TM mode profile.

Simulation geometry is extracted from SEM image of fabricated device; ridge height is 5 µm, active region thickness is 1.5 µm, active region top width is 16 µm and side wall angel is 57°.

Chapter 3

Device Fabrication and Packaging

This chapter focuses on fabrication development and fabrication steps of mid-infrared quantum cascade laser. Conventional ridge processes have been successfully developed based on the nanofabrication facility in Bilkent University Nanotechnology Research Center (NANOTAM).

3.1. Epitaxial Growth

In order to form designed quantum states the high quality of epitaxial layers are essential. The very first step in the quantum cascade laser development is active region growth with sensitive control of the layer thickness. Molecular beam epitaxy (MBE) can satisfy those requirements; sensitive thickness control, layer flatness and high quality epitaxial layer. Basically MBE is a thermal evaporator with ultra low vacuum (about 10^{-11} mbar). Schematic illustration of MBE system is presented in Figure 3.1. Thermal source of the MBE calls Knudsen cell which keeps the source material and heat them, under the ultra low vacuum environment, high quality epitaxial film can be grown on the substrate.

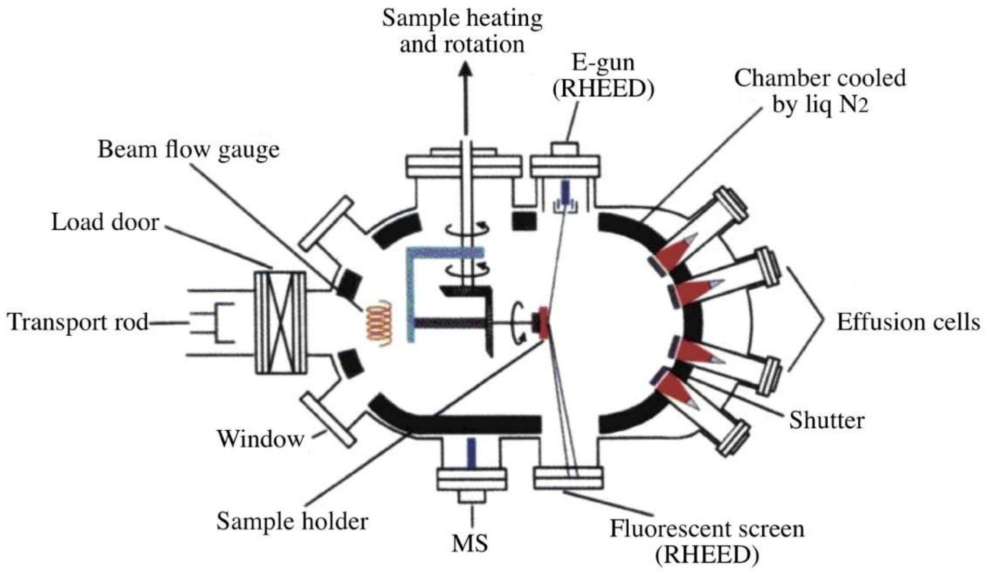

Figure 3.1 Schematic illustration of molecular beam epitaxy (MBE) system [34].

3.2. Cleanroom Fabrication

It has been clear that quantum cascade laser performance not only depends on active layer design but it strongly depends on waveguide design and packaging [35]. Waveguide structure directly affects thermal and optical performance of the laser [35,36].

In this section fabrication processes will be described in detail. Main fabrication steps are (Figure 3.2);

Step 1: Wafer Cleaving and Sample Cleaning
Step2: Top Contact Lithography
Step3: Top Contact Deposition
Step4: Mesa Lithography
Step5: Mesa Etching
Step6: Dielectric Coating
Step7: Dielectric Opening
Step8: Seed Metal Lithography
Step9: Seed Metal Deposition

Step10: Electrolyse Lithography

Step11: Electroplating

Step12: Lapping

Step13: Back Side Contact Deposition

Step14: Mounting and Mirror Coating

Step15: Packaging

Each fabrication steps will be discussed in detail in following sub-sections.

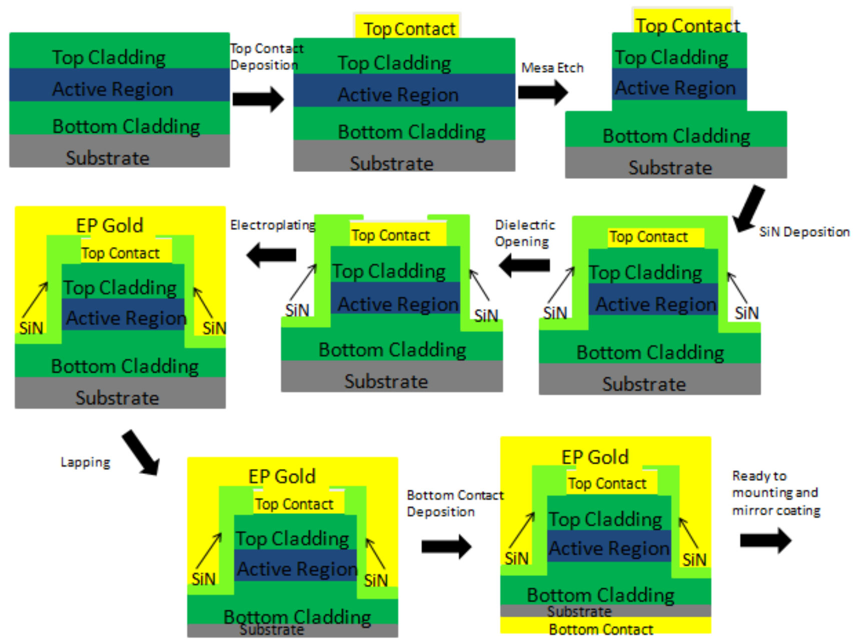

Figure 3.2 Schematic diagram of ridge quantum cascade laser fabrication process.

3.2.1. Wafer Cleaving and Sample Cleaning

2 inch wafer is cleaved into 12mmx12mm small pieces, since wafer is very expensive and very hard to grow. Also by this way, more than one process can be performed by using the same wafer. To cleave wafer, a diamond tipped scribing tool (diamond pen) is used. Wafer is scratched by diamond pen though the crystal direction and small pressure is applied to divide wafer, this process is repeated to other direction in order to obtain 12mmx12mm pieces.

Cleaved wafer pieces are cleaned by sonication by rinsing de-ionized water, acetone, and isopropyl alcohol, 10 min in each step. Since wafer is very fragile, sonication power is adjusted as less as possible (10% in our case). After that, samples are dried with nitrogen gun. Finally samples are controlled with optical microscope. If they are not clean enough, cleaning procedure repeated until obtaining clean surface.

3.2.2. Top Contact Lithography

Different than conventional quantum cascade laser fabrication, top contact lithography and deposition are the first steps of our fabrication instead of mesa etch. Since, good electrical contact requires clean surface, top contact deposition is performed first.

The top contact of the laser bars defined using image reversal resist and contact printing mask aligner (Karl Süss MA6). Photomask for top contact lithography is presented in Figure 3.3.

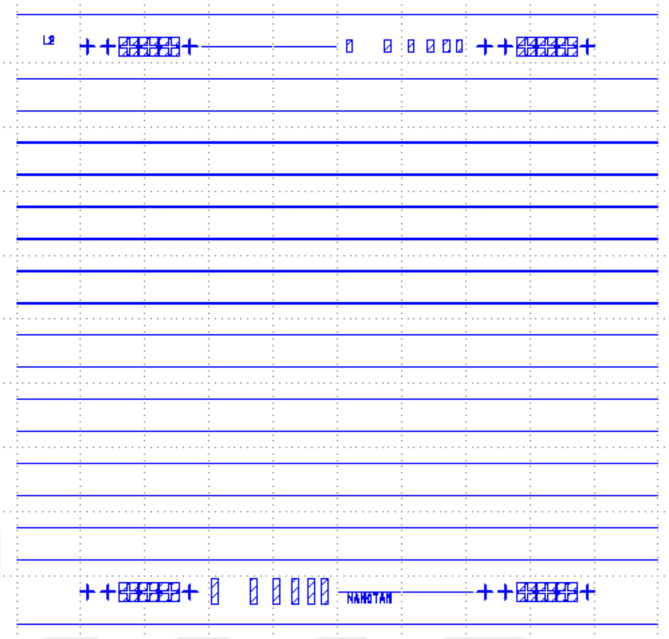

Figure 3.3 Top contact lithography mask.

20 μm and 16 μm laser bars and transfer length method (TLM) patterns exist in the mask.

In this photolithography process, AZ5214E type photoresist is used, which is an image reversal photoresist .Karl Suss MA6 Mask Aligner is used for alignment and exposure.(10mW/cm2).AZ400K developer is used for removing exposed areas on photoresist. Image reversal photoresist is chosen instead of positive tone photoresist, since lift-off process is easier [37].

For image reversal photolithography, AZ5214E photoresist is coated and spun at 5000 rpm for 60 sec (Photo resist thickness is 1.4 μm). Then samples are baked 110 ^{o}C for 55 seconds to dry photoresist. After that using photomask, with samples are exposed 16 mJ/cm^{2} UV light. Then, they are baked at 110 ^{o}C for 2 min, and after that, exposed again for 60 mJ/ cm^{2} .

After lithography step samples are developed with AZ400K (diluted with water 1:4) for 22 second, after samples are rinsed with DI water and dried with nitrogen gun. Development is checked under an optical microscope. Optical microscope image after development is presented in Figure 3.4.

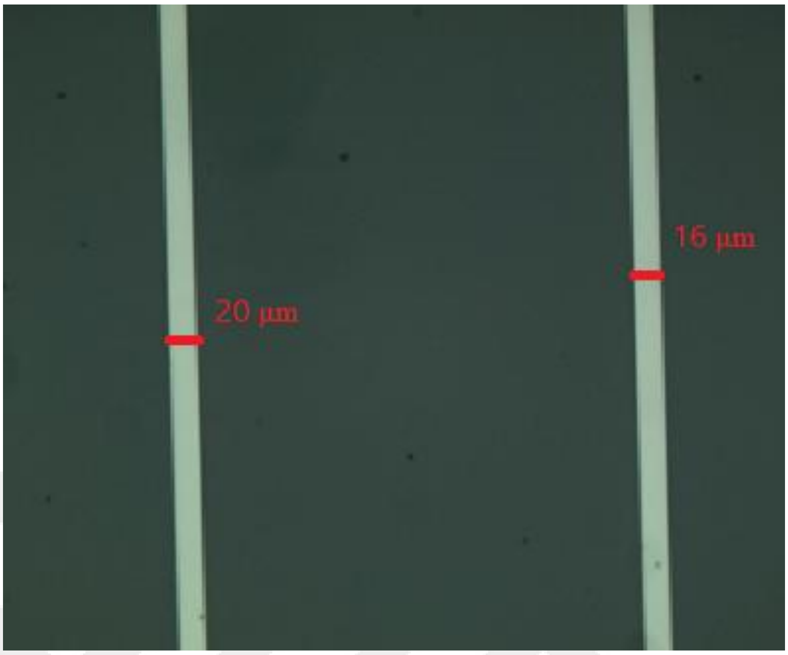

Figure 3.4 Optical microscope image (20x optical zoom) after top contact lithography an development.

3.2.3. Top Contact Deposition

For ohmic contact deposition electron beam (E-Beam) evaporator (Oerlikon Leybold Univex 350 E-Beam Evaporator System) is used.

Two different metal combinations are tried. Ti/Pt/Au and Pt/Ti/Pt/Au are deposited. However Pt/Ti/Pt/Au has adhesion problem so bubbles occur after annealing. Therefore for ohmic top contact deposition 30 nm Titanium (Ti), 40 nm Platinum (Pt) and 200 nm Gold (Au) are deposited at rate respectively 0.2 nm/sec, 0.2 nm/sec and 0.3 nm/sec. After deposition standard lift-off procedure is applied, samples rinsed with acetone to solve photoresist and rinsed with isopropanol to clean acetone on the samples. Since image reversal photoresist is used, lift-off process is straightforward. After lift-off, samples are annealed at $400^{o}C$ for 30 seconds in order to decrease contact resistance further. Since quantum cascade laser is worked at high current levels, high ohmic contact resistance forms excess electrical loss, indeed it heats the device unnecessarily and causes performance loss of the quantum cascade laser. Therefore good ohmic contact formation is crucial for high performance quantum cascade laser. In order to check ohmic contact quality 4 probe TLM measurements is performed. As extracted from TLM measurement ohmic contact specific contact resistance is $3.03x10^{-7}$ Ω.cm^2 and after annealing resistance is $1.81x10^{-7}$ Ω.cm^2. Optical microscope image after metal deposition and annealing is in Figure 3.5.

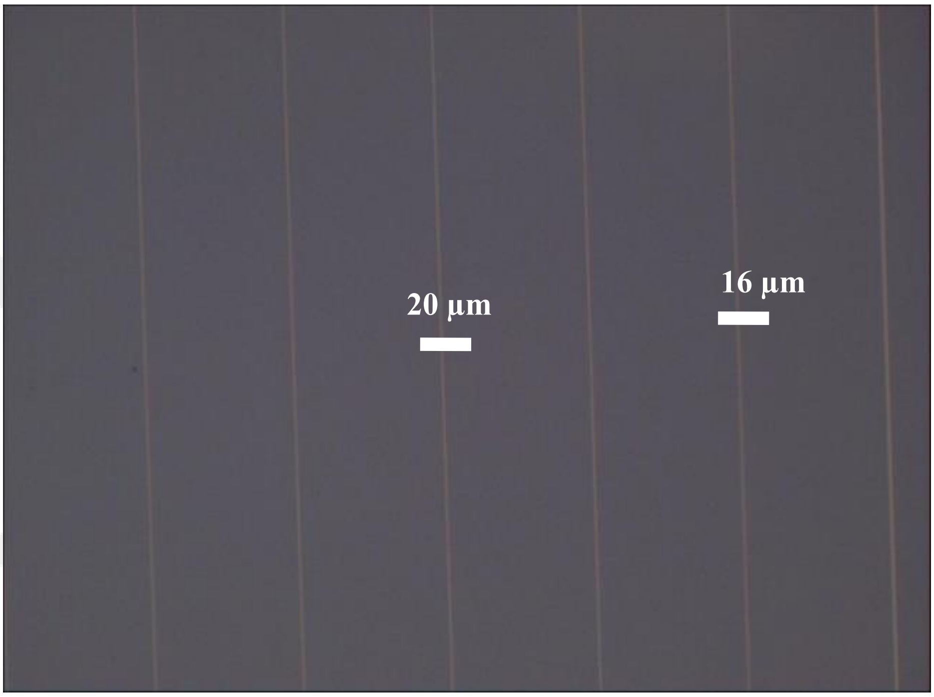

Figure 3.5 Optical microscope (5x optical zoom) image after metal deposition and annealing.

3.2.4. Mesa Lithography

The mesas of the laser bars defined using positive tone photoresist and contact printing mask aligner. Photomask for mesa lithography is presented in Figure 3.6

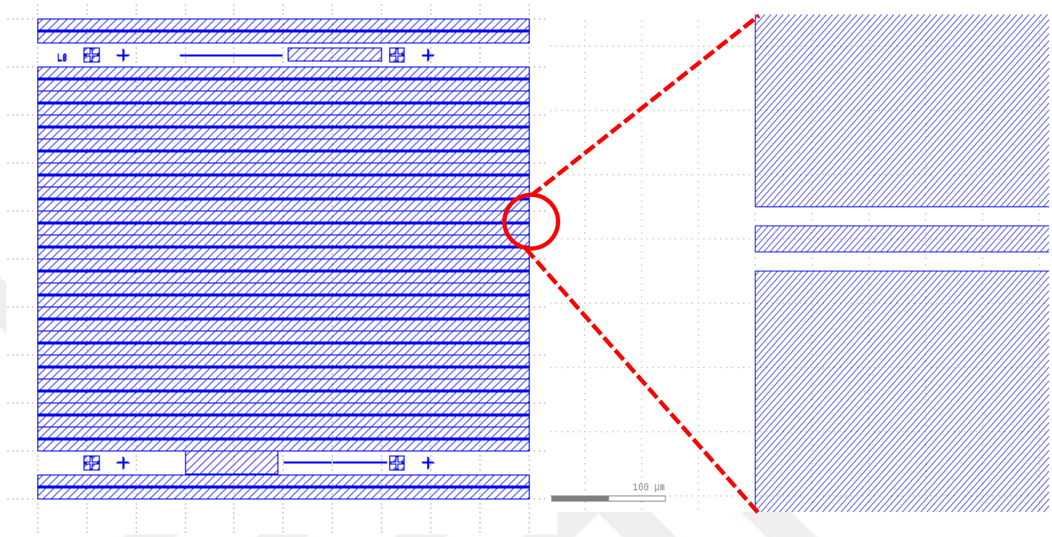

Figure 3.6 Mesa Lithography photomask.

In this lithography process, TI35ES type photoresist is used, which is a positive tone photo resist. Since samples are etched 6.5 µm, photoresist have to be strong and selective enough. TI35ES can meet the requirements; etch resistance and selectivity. Expose dose is 10mW/cm^2 and AZ400K is used as developer (AZ400K:H_2O (1:4)).

Photoresist is coated and spun at 4000 rpm for 40 sec (photoresist thickness is 4.5 µm). Then samples are baked 110 °C for 120 seconds to harden photoresist. After that samples are exposed with 300 mJ/cm^2.

After lithography step samples are developed with AZ400K (diluted with water 1:4) for 30 second, after those samples are rinsed with DI water and dried with nitrogen flow. Development is checked under an optical microscope. Optical microscope image after development is presented in Figure 3.7

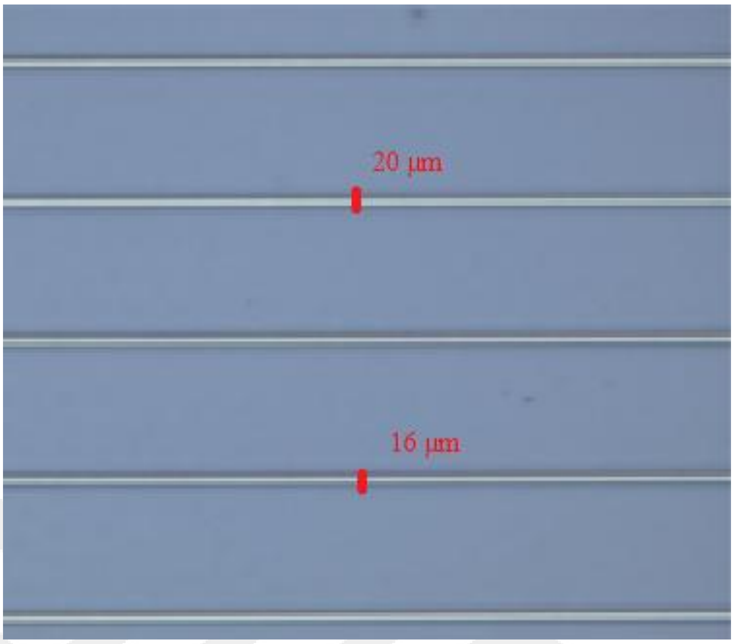

Figure 3.7 Optical microscope (5x optical zoom) image after development.

3.2.5. Mesa Etching

In this study two different etch methods are studied; dry etch or reactive ion etch and wet etch. Both etch methods are frequently used for quantum cascade laser fabrication [38,39,40,41]. Basically wet etch is the chemical reactions at the surface of the substrate with etchants. Although generally wet etching is isotropic, HCL: CH_3COOH (1:3) is strongly anisotropic for InP. Therefore HCL: CH_3COOH (1:3) solution is used for InP etching in order to reduce undercutting and obtain nearly vertical side wall and HBr: HNO_3:H_2O (1:1:10) is used for active layer etching [35,42]. Unfortunately wet etching method is not reliable enough and sometimes it causes surface contamination and surface bubbling (Figure 3.8). Indeed it is not repeatable enough for such an expensive substrates.

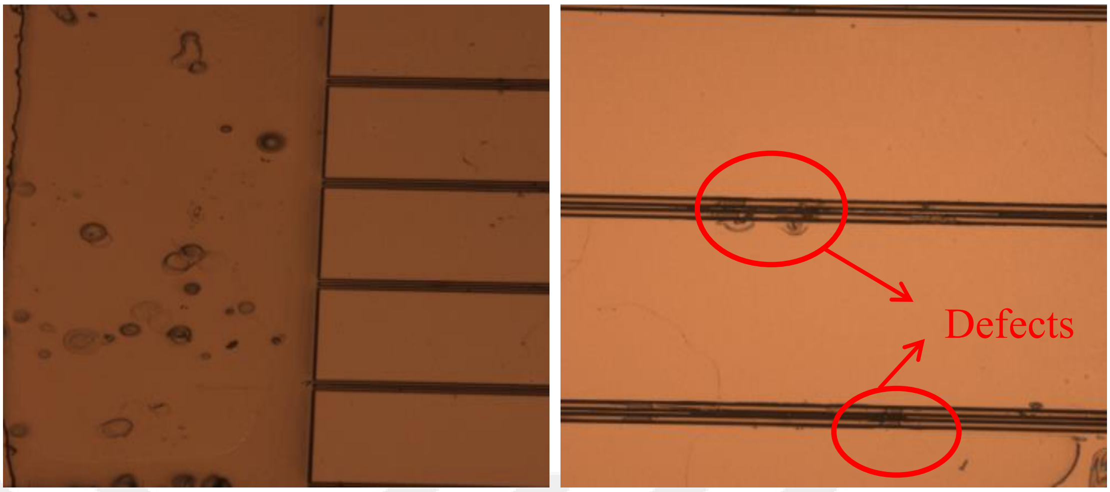

Figure 3.8 Optic microscope images after wet etching.

Scanning electron microscopy (SEM) image of quantum cascade laser after wet etch is presented in Figure 3.9

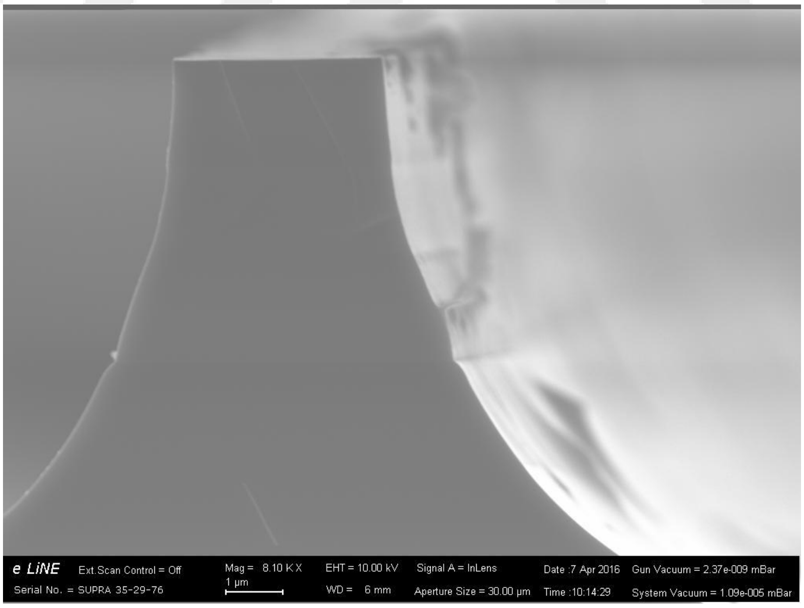

Figure 3.9 SEM image of quantum cascade laser after wet etch.

Therefore dry etching especially inductively coupled reactive ion (Sentech SI 500 Dry Etching System(ICP-RIE)) is used in this study. Shortly, ICP-RIE, which uses directional ion bombardment and utilizes chemical etching at the same time, also with using plasma (ICP) chemical etching can be utilized more, however plasma can etch organics i.e. photoresist at very high rate, therefore ICP power is kept zero in this study.

The most important property of RIE is high directionality, i.e. the vertical etch rate is much higher than the lateral etch rate, so very reliable etching can be obtained with RIE. In this study BCl_3:Cl_2 with 80 W RF power is used, 80 nm/min etch rate is obtained. Samples are etch 80 minutes to obtain 6.5 μm depth mesas.

Mesa etching is the most important part of the process because waveguide shape directly affects the optical and thermal performance of the laser [35,43]. For example side wall angle is important parameter that determines plasmonic loss [41]. Due to selection rule quantum cascade laser can only emits TE polarized light and it is well known that plasmon can only be coupled with TM polarized lights [44]. Therefore if side wall become vertical, plasmon loss will be zero. In addition side wall roughness also causes optical losses [45]. As side wall roughness increases due to scattering loss, optical power decreases. In this study different dry etch recipes are studied to obtain most vertical and smooth side wall.

Also depth of mesas is important. Mesa has to be deep enough to isolate active layer from the substrate in order to prevent electrical shorts and provide current confinement. However as depth of mesa i.e. bottom cladding depth, increases, thermal resistance increases, which directly reduce maximum optical power of the quantum cascade laser. 6.5 μm depth mesas is the optimal depth for this study.

SEM image of quantum cascade laser after dry etch is presented in Figure 3.10.

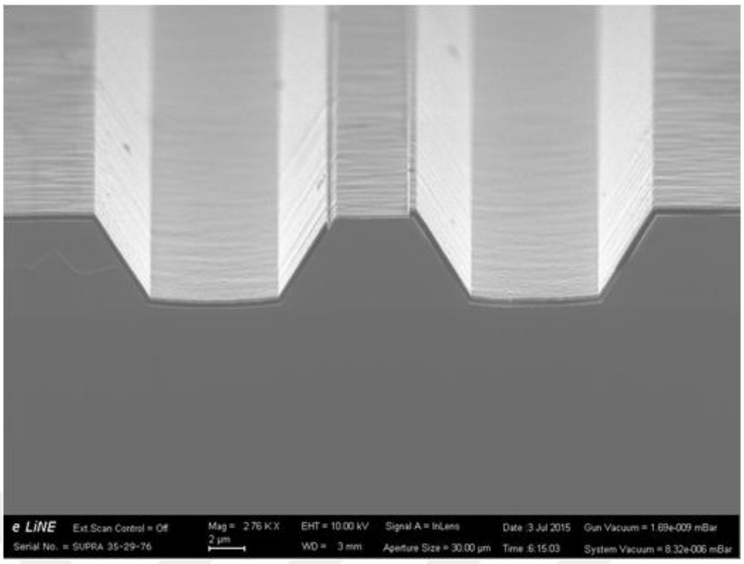

Figure 3.10 SEM image of quantum cascade laser after dry etch.

Also in order to obtain vertical and smooth side walls different dry and wet etch combinations are studied and obtain almost 90^o vertical and smoothest side wall, mushroom like quantum cascade laser. SEM image of this structure is presented in Figure 3.11.

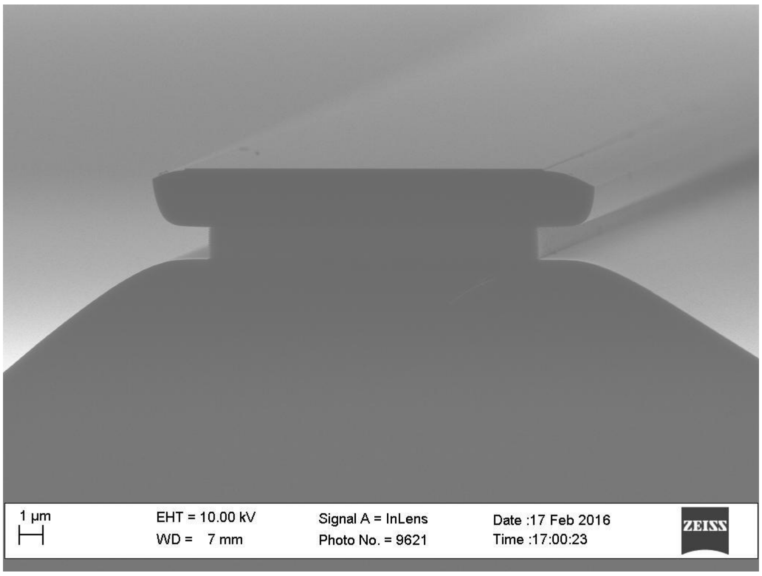

Figure 3.11 SEM image of mushroom like quantum cascade laser.

3.2.6. Dielectric Coating

Dielectric coatings (Si_3N_4, SiO_2) are deposited by plasma enhanced chemical vapor deposition system (PECVD) (SENTECH SI 500 PPD Plasma Enhanced Chemical Vapor Deposition). PECVD allows low temperature dielectric depositions by reducing required thermal energy by plasma. Gases used for dielectrics are silane (SiH_4), ammonia (NH_3), and N_2O. SiH_4 and NH_3 are used for Si_3N_4 deposition and SiH_4 and N_2O are used for, SiO_2 deposition. Thickness of dielectrics are measured by elipsometer (Sentech Se 850 Spectroscopic Elipsometer)

Thin layer of Si_3N_4 or SiO_2 is deposited on top of the structure in order to provide insulation layer between top of the waveguide and side walls of the structure and substrate. This passivation layer is crucial for quantum cascade laser operation, any degradation on this layer can cause to the malfunction of the laser operation, most probably shorting the quantum cascade laser [17].

Since ridge waveguide structure is used, this passivation layer directly influences optical and thermal performance of the device. Thermal point of view, since passivation layer cover active core, which produces entire heat of the quantum cascade laser structure, completely, thermal conductance of passivation layer should be high in order to cool active core enough. From an optical point of view, since optical modes overlap with this passivation layer absorption of these layer cause optical loss, therefore for less optical loss due to passivation layer absorption, absorption coefficient of this layer should be less in the spectrum that laser operates. Thickness of this layer is, also, important, because when thickness increase thermal resistance increases and plasmonic loss decreases. Therefore for passivation dielectric material and its thickness should be chosen by considering both optical and thermal effects at the same time.

Computer based simulations are performed for dielectric material and thickness decision. "Lumerical Mode Solver" is used for optical loss simulations and "COMSOL" is used for thermal simulations. Lumerical optical loss simulation results with different dielectric material and thickness is presented in Figure 3.12.

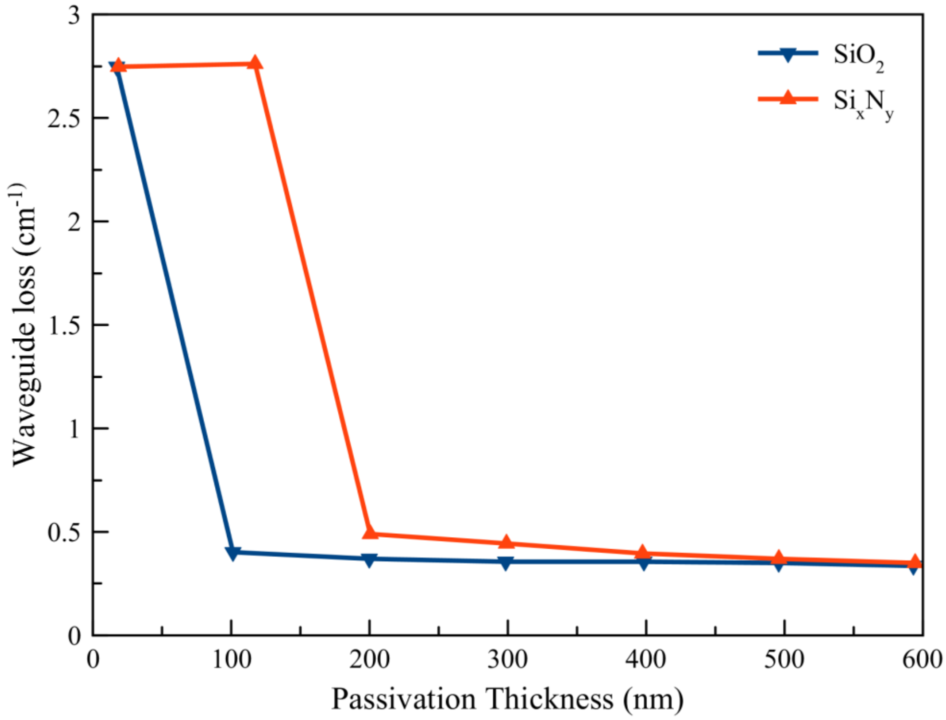

Figure 3.12 Lumerical optic loss simulation with different passivation material and thickness.

As it is seen above 250 nm dielectric thickness, optical losses of Si_3N_4 and SiO_2 are the almost same and further thickness increments would not affect loss significantly.

3.2.7. Dielectric Opening

In order to make electrical connection of top contact metal, coated dielectric is etched on the top of the top contact metal. The openings of the laser bars are defined using positive tone photoresist and contact printing mask aligner. Photomask for mesa lithography is presented in Figure 3.13.

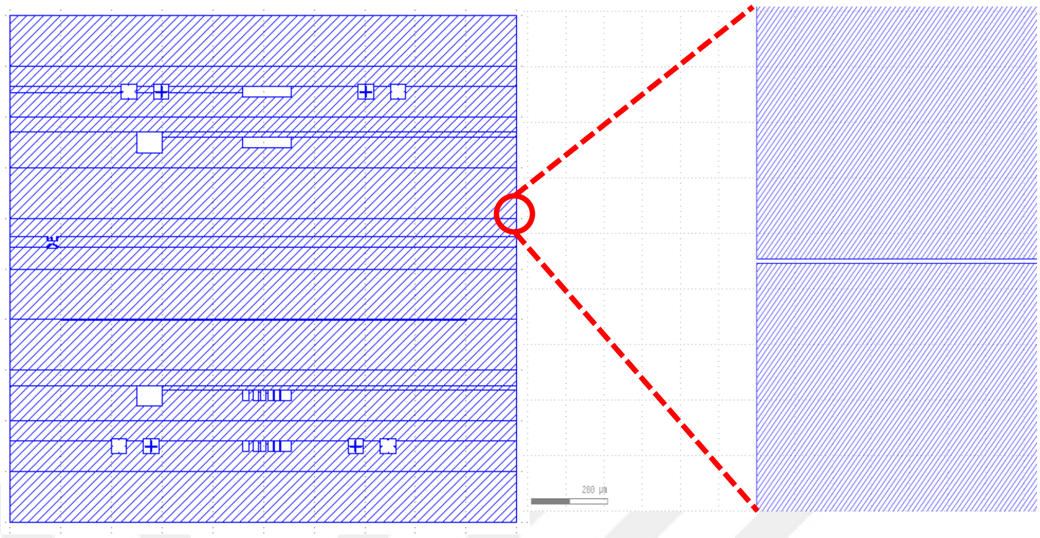

Figure 3.13 Photomask for dielectric opening lithography.

For this photolithography step, TI35ES photoresist is coated and spun at 4000 rpm for 40 sec (photoresist thickness is 4.5 µm).Then samples are baked 110 ^{o}C for 120 second to harden photoresist. After that samples are exposed 300 mJ/cm^2 optical energy.

After lithography step samples are developed with AZ400K (diluted with water 1:4) for 25 second, after those samples are rinsed with DI water and dried with nitrogen flow. Development is checked under an optical microscope. Optical microscope image after development is presented in Figure 3.14

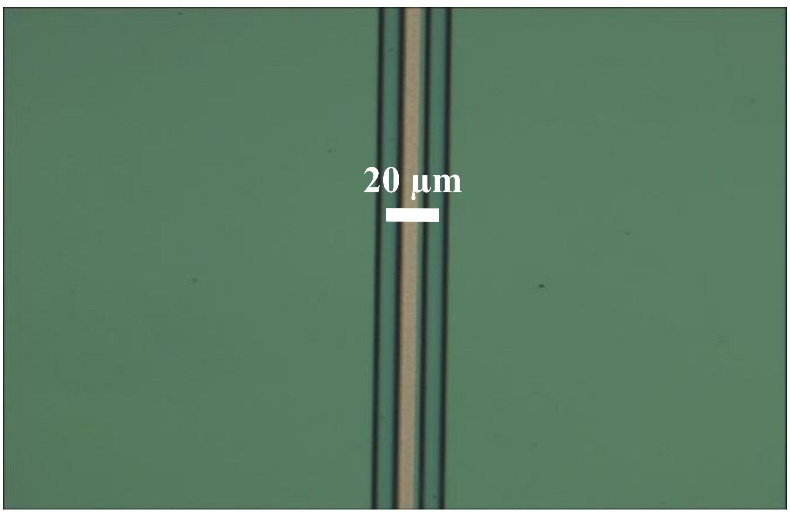

Figure 3.14 Optical microscope image after Si_3N_4 deposition and opening.

For dielectric etching, dry etch method is used. CFH_3 with 100 W RF power is applied for 5 minutes. Cross-section SEM image after dielectric opening is presented in Figure 3.15 as it is seen dielectric opening is successfully etched.

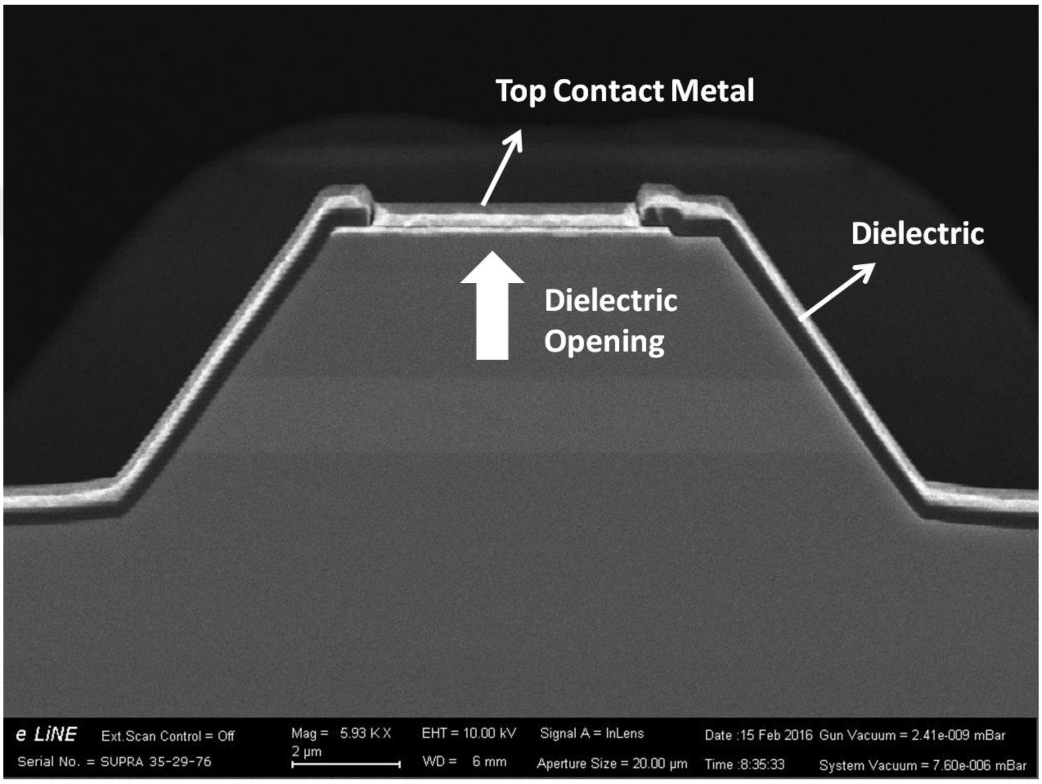

Figure 3.15 SEM image after dielectric opening.

3.2.8. Seed Metal Lithography

In order to provide better electrical connection and infrigidation, thick metal deposition is performed on top of the laser bars. In general in the order of 5 μm gold deposited on the top. However gold deposition with physical vapor deposition is too expensive for order of micron gold deposition. Therefore this thick metal is deposited with electroplating. However as it is known, electroplating can only deposit metal on the conductive surfaces. Hence, providing conductive surface on the laser bars, seed metal deposition is performed.

Indeed seed metal deposition without patterning is enough for purpose. However, since laser bars are cleaved parallel to the laser bar direction after fabrication, this thick metal flakes and causes electrical shorts if thick metal is deposited without patterning. Cross section scanning electron microscopy image of quantum cascade laser deposited thick metal without patterning is presented in Figure 3.16. Flakes can be seen on the top of the laser.

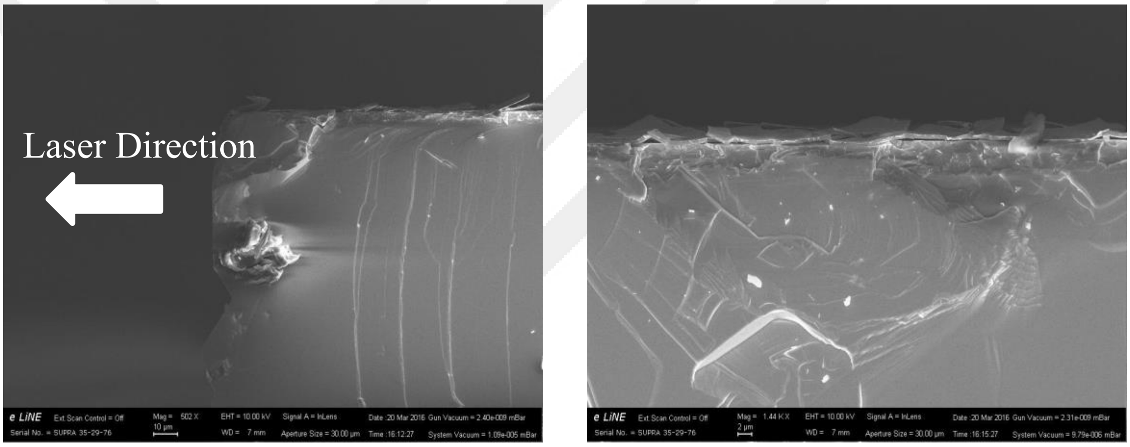

Figure 3.16 Cross section scanning electron microscopy image of quantum cascade laser deposited thick metal without patterning.

The seed metal pattern is defined by image reversal photoresist and contact printing mask aligner. Used photomask for mesa lithography is presented in Figure 3.17.

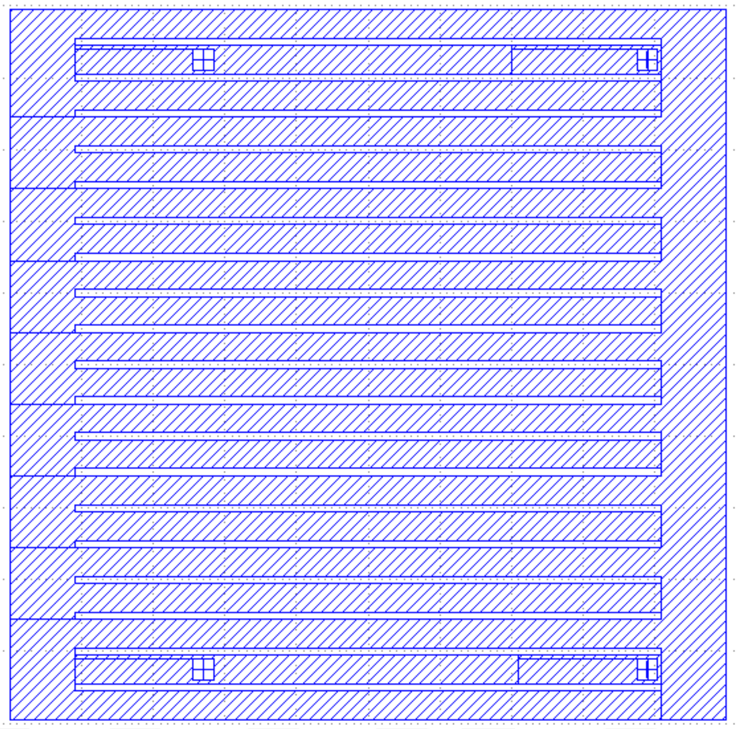

Figure 3.17 Photomask for seed metal lithography.

3.2.9. Seed Metal Deposition

For seed metal deposition electron beam (E-Beam) evaporator (Oerlikon Leybold Univex 350 E-Beam Evaporator System) is used. 20 nm Ti, 200 nm Au is deposited at rate 0.2 nm/s and 0.4 nm/s respectively. Titanium is used to promote metal adhesion and gold serve as seed layer for electroplating.

3.2.10. Electroplating Lithography

To obtain clean in other word mirror like laser facet, thick metal is not coated entire laser bar due to flaking problems. 100 µm gap is intentionally left in between 1 mm laser bars. Thus scribing blade can easily cut in this gap. Used photomask for electroplating lithography is presented in Figure 3.18

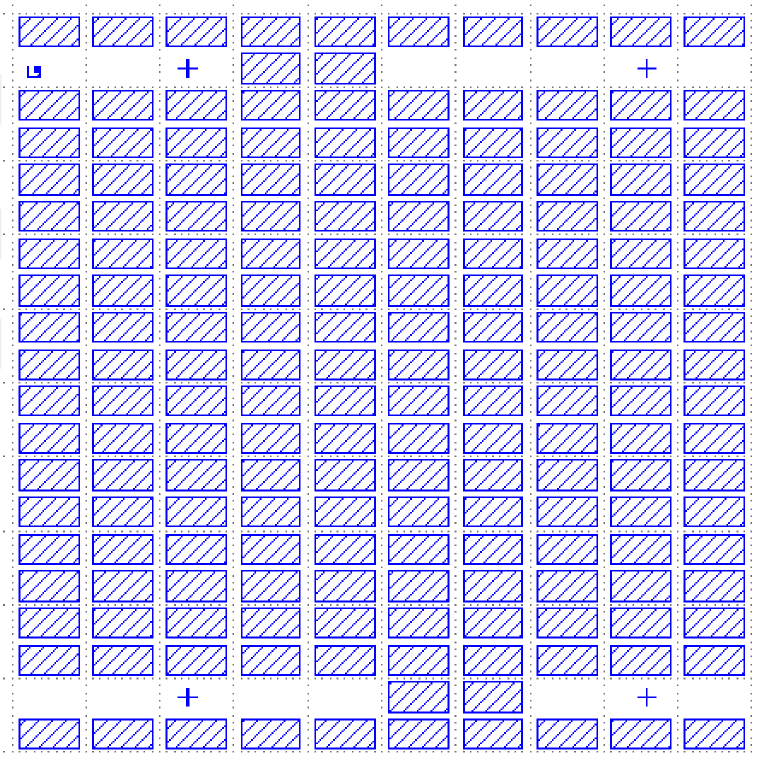

Figure 3.18 Photomask for electroplating lithography.

After lithography step samples are developed with MIF 326 for 37 second, after those samples are rinsed with DI water and dried with nitrogen gun. Development is checked under an optical microscope. Optical microscope image after development is presented in Figure 3.19.

For this photolithography step, Nlof 2070 photoresist is coated and spun at 5000 rpm for 60 sec (photoresist thickness is 8.5 μm). Then samples are baked 95 ^oC for 60 second to harden photoresist. After that samples are exposed 180 mJ/cm^2 and baked 95 ^oC for 60 seconds.

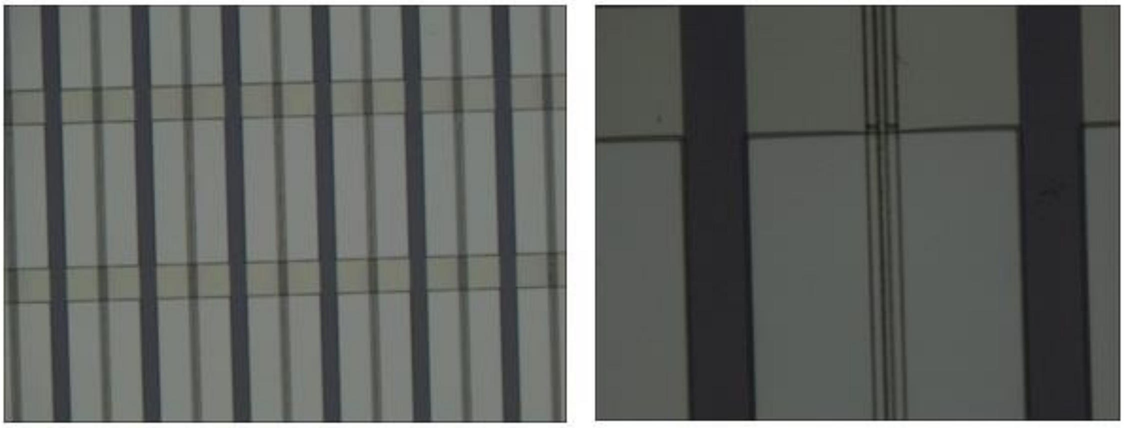

Figure 3.19 Optical microscope image after electroplating lithography and development.

3.2.11. Electroplating

To deposit thick metal electroplating technique is used instead of physical vapor deposition (PVD), because of easiness and inexpensiveness. During electroplating electrolyte temperature is fixed to 50 ^{o}C and 3 mA current is applied to the sample. Electroplating setup is presented in Figure 3.20.

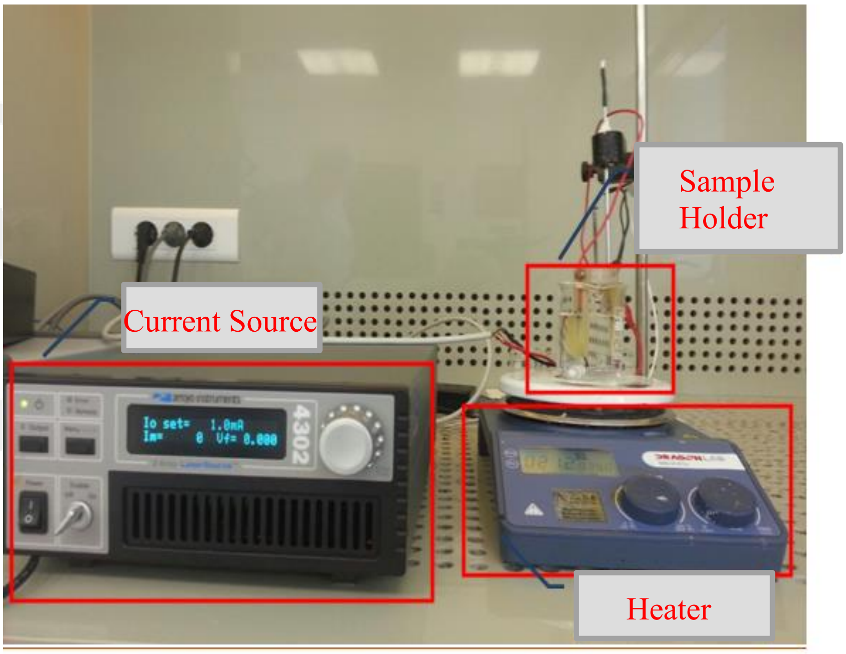

Figure 3.20 Electroplating setup.

5 µm gold is deposited at rate 142 nm/min by electroplating technique. After electroplating, standard development methods is applied. SEM image after thick metal deposition is presented in Figure 3.21.

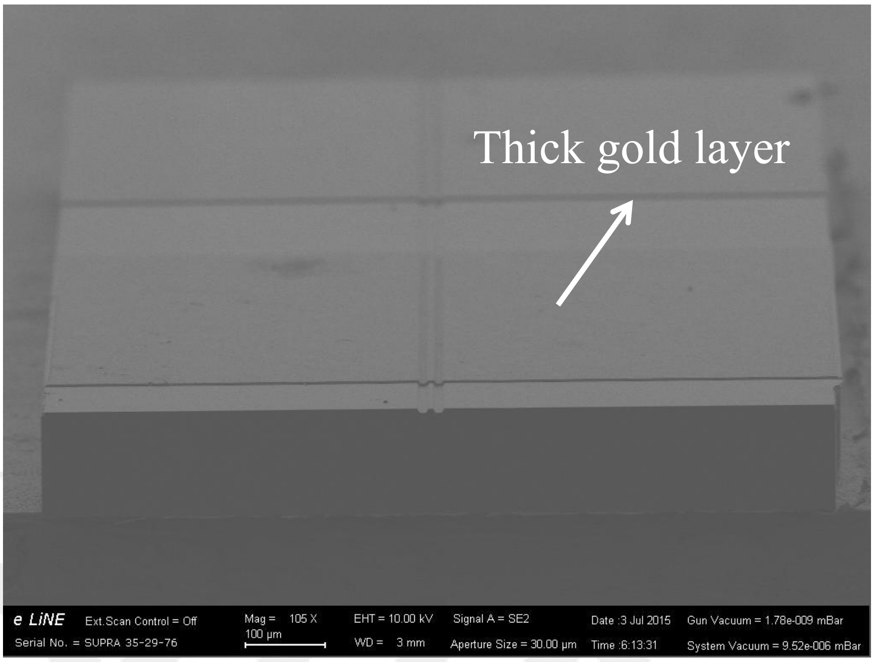

Figure 3.21 Scannig electron microscop image after thick metal deposition.

3.2.12. Lapping

Quantum cascade laser suffers from high operation voltages (about 13 V in this study) and large threshold currents (about 1 A in this study), which causes high local heating inside the active core of the laser. Therefore effective heat removal from active core is crucial for high performance quantum cascade laser especially working at room temperature [46].

Generally quantum cascade lasers are cooled from bottom of the substrate. Therefore decreasing the distance between active core, which produce entire heat, and bottom of the substrate increases effectiveness of cooling performance.

Hence, fabricated quantum cascade lasers are lapped 370 μm to 100 μm with (Logitech Pm5 Lapping&Polishing System) in this study. Beyond the 100 μm, of course, enhances cooling performance yet handling the devices would be nontrivial.

3.2.13. Backside Contact Deposition and Device Cleaving

After substrate lapping, bottom of the laser structure are deposited 20 nm germanium (Ge), 40 nm gold (Au), 20 nm nickel (Ni), 200 nm gold (Au) and 10 nm nickel (Ni) by e-beam evaporator (Oerlikon Leybold Univex 350 E-Beam Evaporator System) and 100 nm indium (In) by thermal evaporator (Nanovak Inkas Thermal Evaporator System). Germanium layer serve as thin buffer layer, and it diffuses into InP substrate to enable better ohmic contact with negligible contact resistance [32]. First nickel layer is used as diffusion block layer it prevents germanium to diffuse final gold layer and second nickel layer prevent indium to diffuse through the substrate. Indium layer is deposited in order for indium-indium soldering at packaging process.

After back contact metal deposition, in order to separate each laser bars and to obtain fresh and clean laser facet to form Fabry-Perot cavity, substrate is cleaved by scriber (JFP Microtechnic Scriber S 100).Separated laser bars and rest of the substrate image is presented in Figure 3.22.

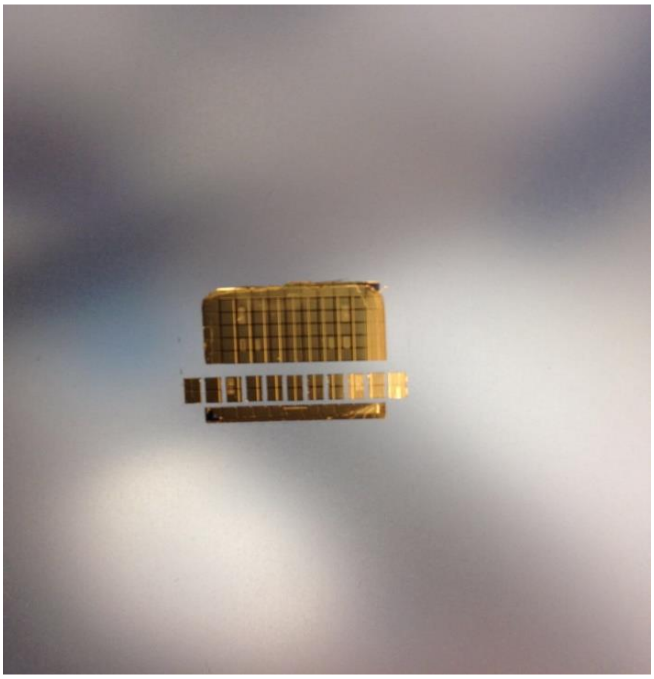

Figure 3.22 Separated laser bars and remained substrate.

3.2.14. Mirror Coating and Device Mounting

Typical quantum cascade laser uses cleaved facet which has low reflectivity coming from the dielectric coefficient difference between active region and air. Elementary Fresnel analysis of the facet reflectivity is about R ~ 0.33. Mirror coating on the one facet of the laser, improves laser efficiency dramatically, theoretically, if reflectivity was 100%, output optical power would double with mirror coating. Indeed mirror coating is substantial for room temperature operation high power quantum cascade laser. Increasing the waveguide dimensions, i.e., width and/or length, result in higher peak power in pulsed mode yet increasing the dimensions is not desirable for CW and/or quasi-CW operated devices because active region self-heating hinders the device operation and plunge the device performance dramatically [47,48]. Moreover increasing waveguide dimensions result in lower beam quality as well [48]. Therefore mirror coating, which increase optical power without increasing waveguide dimensions, is promising for room temperature high power quantum cascade laser.

In this study, first quantum cascade laser devices are mounted on copper a (Cu) plate which is equal length of the quantum cascade laser device. In order to perform indium (In)-indium (In) mounting, 1 μm In is deposited by thermal evaporator (Nanovak Inkas Thermal Evaporator System) on Cu plates. After mounting, a mirror coating begins. Mirror coatings consist of, from the facet, 100 nm Al_2O_3, 5 nm Ti and 100 nm Au, which are deposited by E-Beam evaporator (Oerlikon Leybold Univex 350 E-Beam Evaporator System). Al_2O_3 is deposited in order to ensure electrical isolation; Ti is used to promote adhesion of the gold layer to the dielectric layer. In order to obtain near unity reflection “Lumerical” simulations are performed. Simulation of the mirror which consists of 5 nm Ti and 100 nm Au and varying Al_2O_3 thickness is presented in Figure 3.23. 100 nm Al_2O_3 and 100 nm Au dielectric/metal stack provide highest reflectivity according to simulation result.

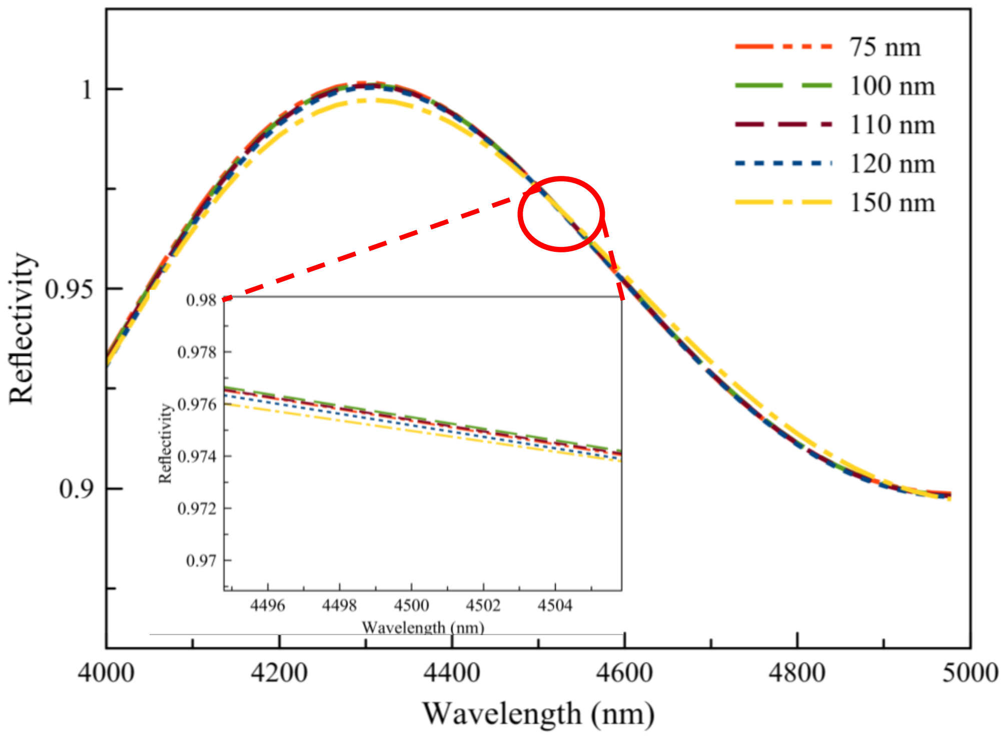

Figure 3.23 Reflectivity of the mirror which consists of 5 nm Ti and 100 nm Au with varying Al_2O_3 thickness.

As it is seen 100 nm Al_2O_3 gives almost unity reflectivity. According to FDTD simulation 100 nm Al_2O_3, 5 nm Ti and 100 nm Au metal/dielectric stack provide 98% reflectivity at 4.5 µm wavelength.

In contrast to the literature where Ti and Au deposition is performed directly on the Al_2O_3 layer, these metal layers are deposited by shadow mask evaporation in this study. Simple razor blade is used as hard mask to protect bottom side of the substrate to ensure electrical short causing by mirror metals and In-In soldering. Mirror coating process steps are presented in Figure 3.24.

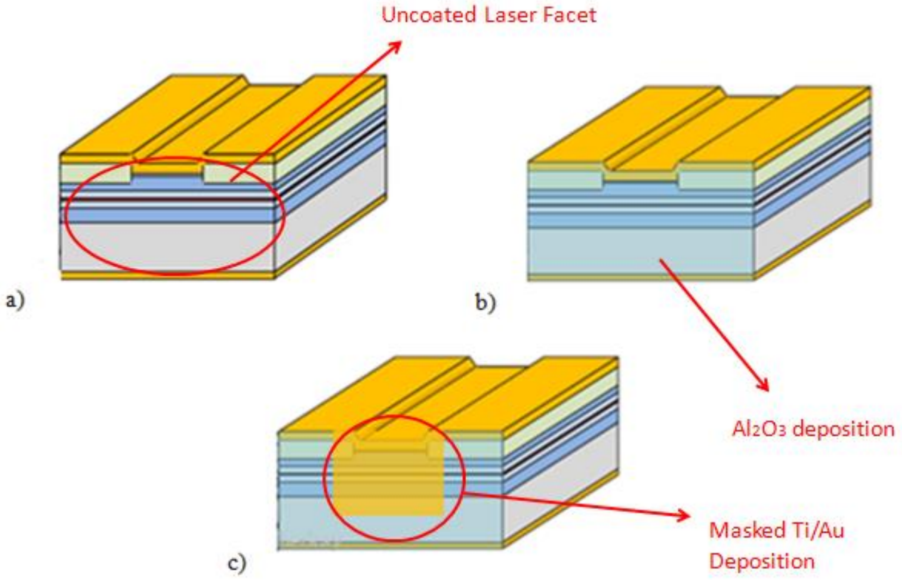

Figure 3.24 Schematic illustration of mirror coating process.

To ensure mirror coating success, optic microscope and SEM images are taken. Optic microscope image is presented in Figure 3.25.

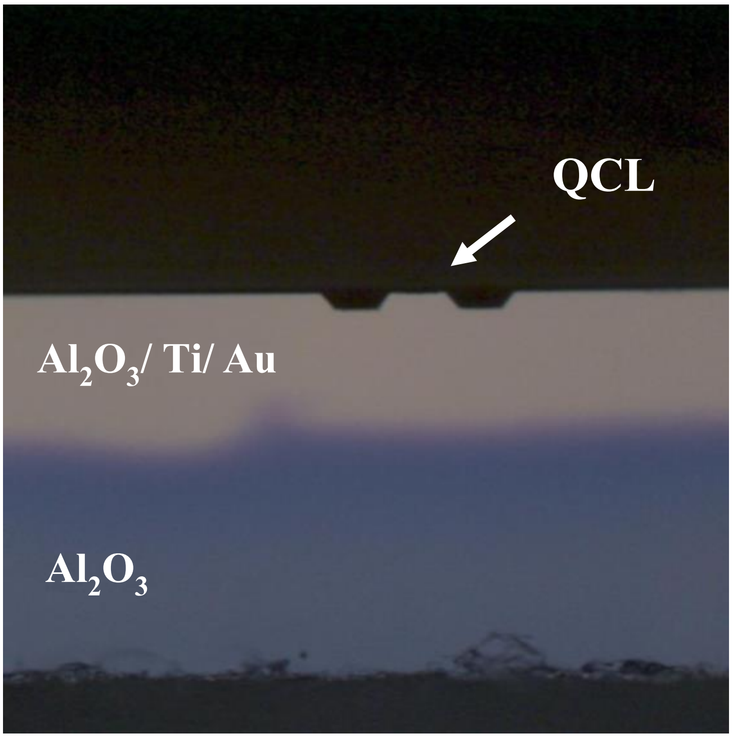

Figure 3.25 Optic microscope images after mirror coating process.

3.2.15. Packaging

Since quantum cascade laser generate considerable amount of heat, and its operation is very sensitive to temperature, it should be cooled well. In order to provide delicate control on the temperature of the device, quantum cascade laser package mounted on thermo electric cooler (TEC) with epoxy (Epo-Tek 360) and electrical connections are completed with wire bonding by (Tbi Hb16 Wire Bonder System). Completed quantum cascade laser is presented in Figure 3.26.

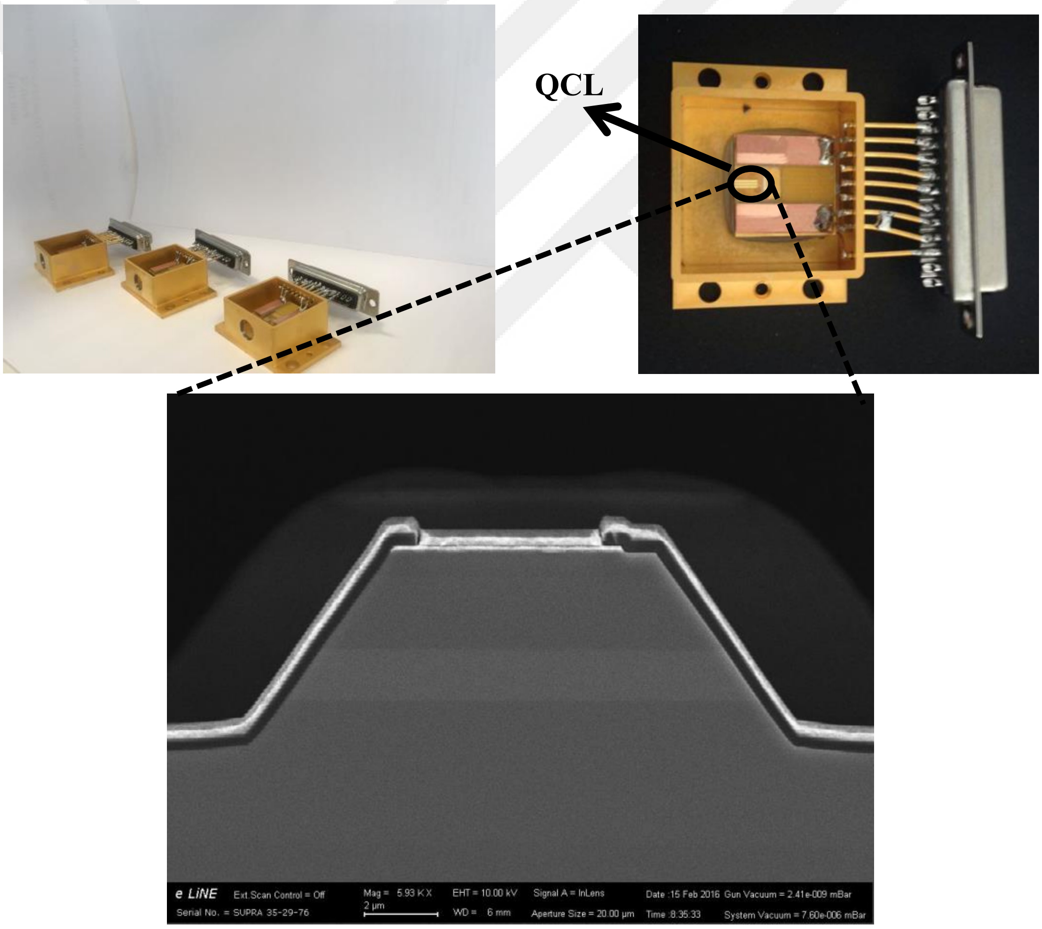

Figure 3.26 Completed quantum cascade laser devices' photography and SEM image.

Chapter 4

Device Characterization and Discussions

This chapter focused on characterization and discussion on characterization results of fabricated quantum cascade lasers. Detailed measurements over these devices are conducted in order to characterize these devices after device fabrication and packaging. Output optical power versus current and voltage on device (L-I-V) measurements are performed at different temperatures for device having different cavity length and cavity width in order to extract device performance parameters. The lasing spectrum is measured at different temperatures and different bias levels for device of different cavity lengths and widths.

4.1. Measurement Setup

In this sub-section measurement setups used for device characterization is discussed. Temperature dependent LIV and spectrum measurements are performed so as to characterize fabricated devices.

4.1.1. Temperature Dependent L-I-V Measurement

Temperature dependent optic power-current-voltage (L-I-V) measurement setup is presented in Figure 4.1.

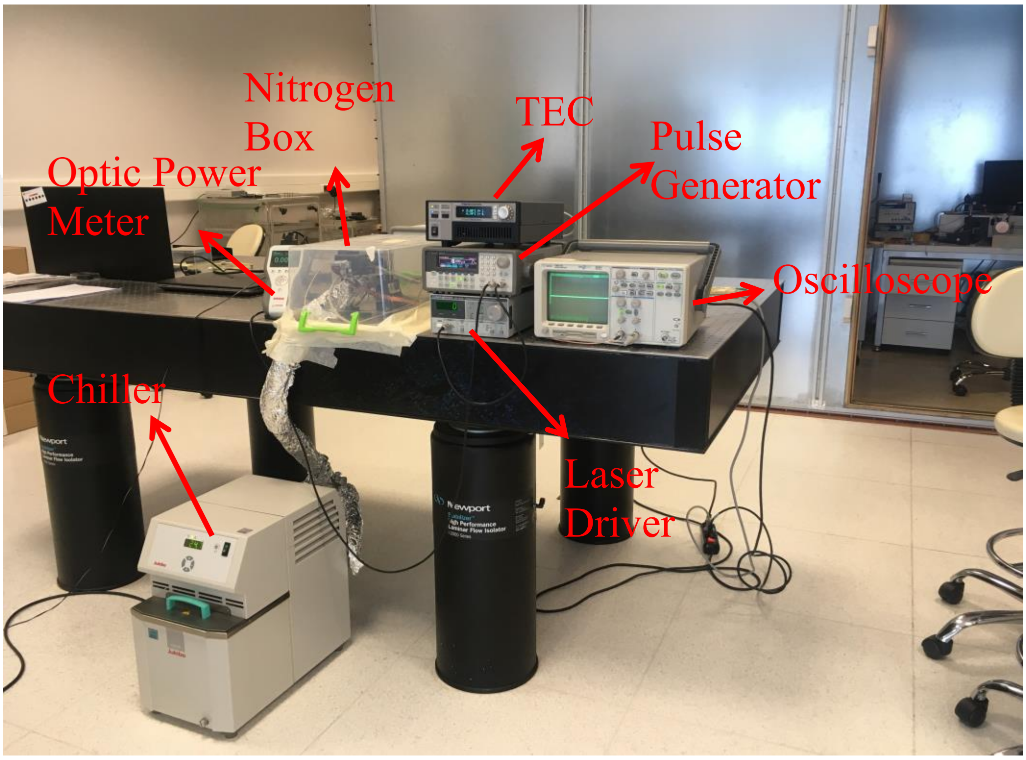

Figure 4.1 LIV measurement setup.

As discussed before quantum cascade laser sub-mount is mounted on thermo electric cooler (TEC) to keep device temperature stable. TEC can control device temperature in between 15 ^{o}C and 30 ^{o}C, for much lower temperatures chiller (Julabo Cf40 Chiller) and homemade nitrogen box is used. Signal generator produces trigger signal to trigger pulsed laser current driver and photo detector with diverse periods in order to adjust duty cycle of laser operation.

Pulsed laser driver supply current pulses to quantum cascade laser with different pulse widths to determine laser duty cycle. Current pulse on the quantum cascade laser is illustrated in Figure 4.2, in which “A” corresponds to pulse period determined by signal generator and “B” is pulse width adjusted by pulsed laser driver then B/A is the duty cycle.

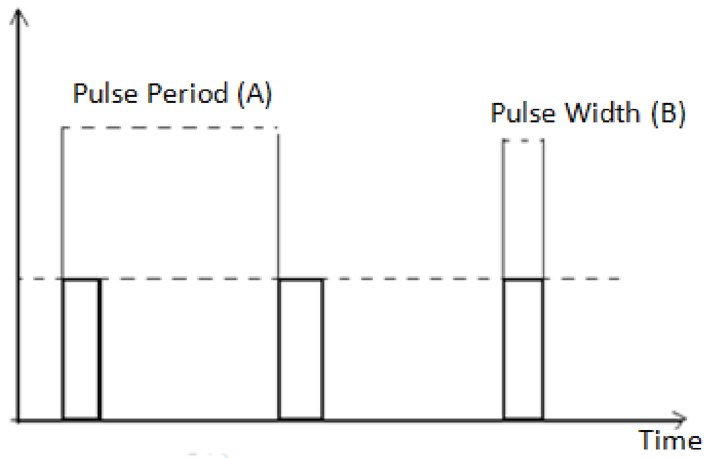

Figure 4.2 Illustration of current pulse applied on quantum cascade laser.

Oscilloscope is used to probe voltage and current on the device. The emitted light is collected by photo detector directly without using any lenses. The measurement setup is illustrated in Figure 4.3.

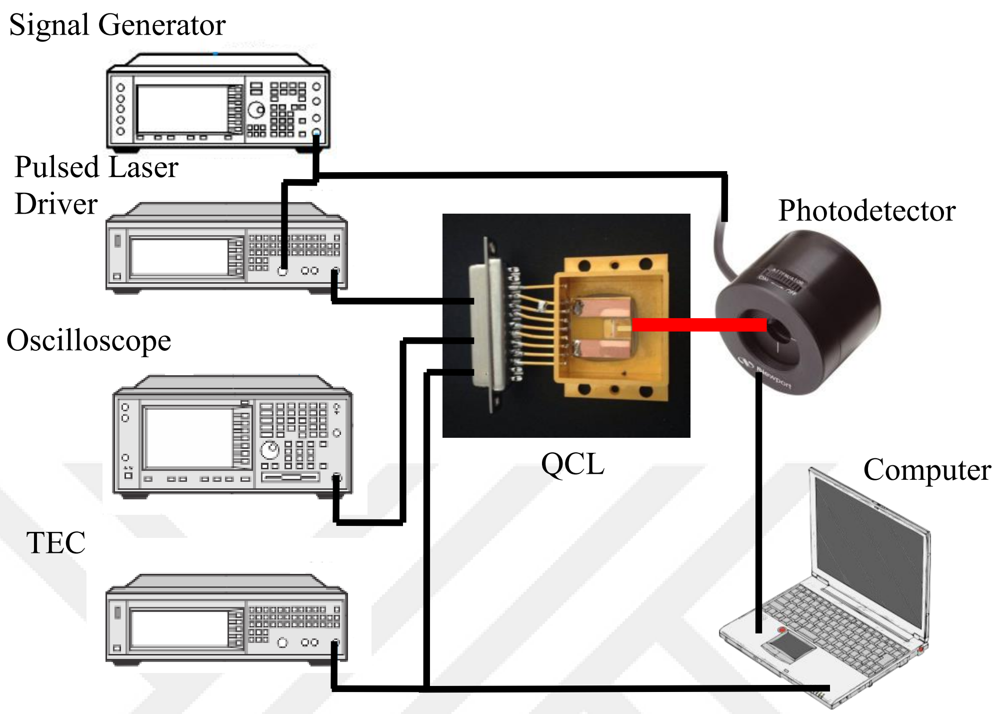

Figure 4.3 Schematic illustration of optical power-current-voltage (LIV) measurement setup.

4.1.2. Spectrum Measurement

The lasing spectrum measurement setup is presented in Figure 4.4.

Figure 4.4 Optical spectrum analyzer used for spectrum measurement.

Spectrum measurement setup is very similar to LIV setup only difference is Fourier Transform Infrared spectrometer (FTIR) is used to collect light instead of photo detector. The measurement setup is illustrated in Figure 4.5.

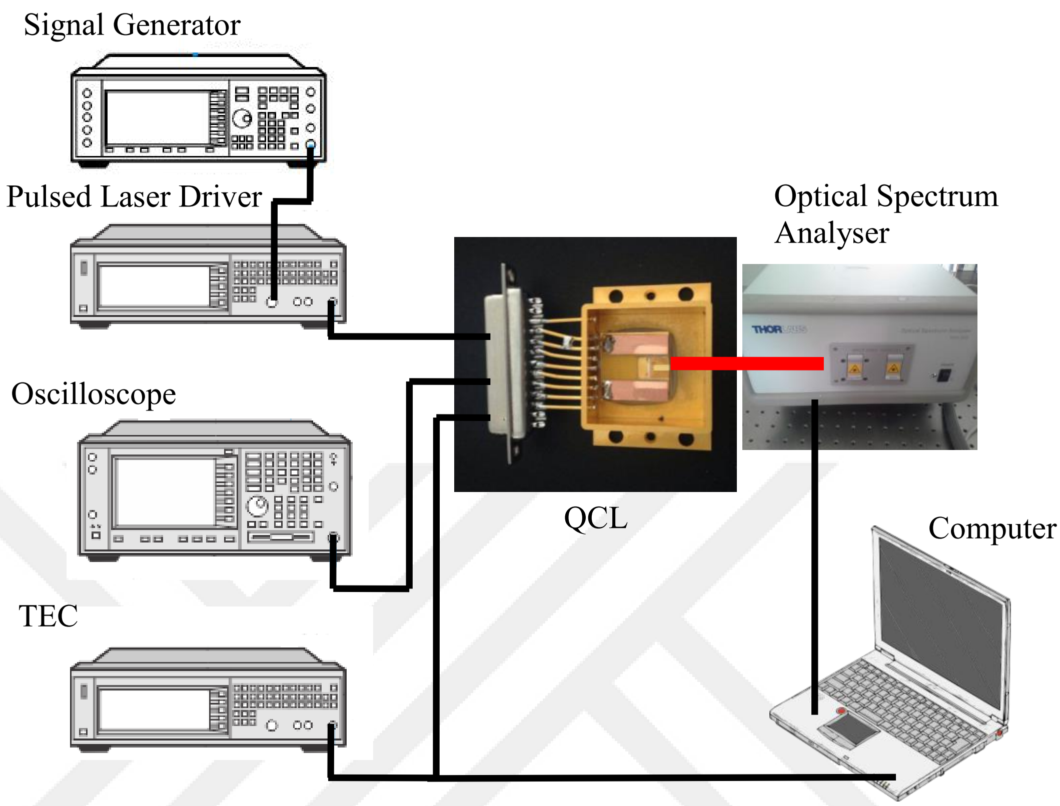

Figure 4.5 Schematic illustration of spectrum measurement setup.

4.2. Results and Discussions

4.2.1. Temperature Dependent L-I-V

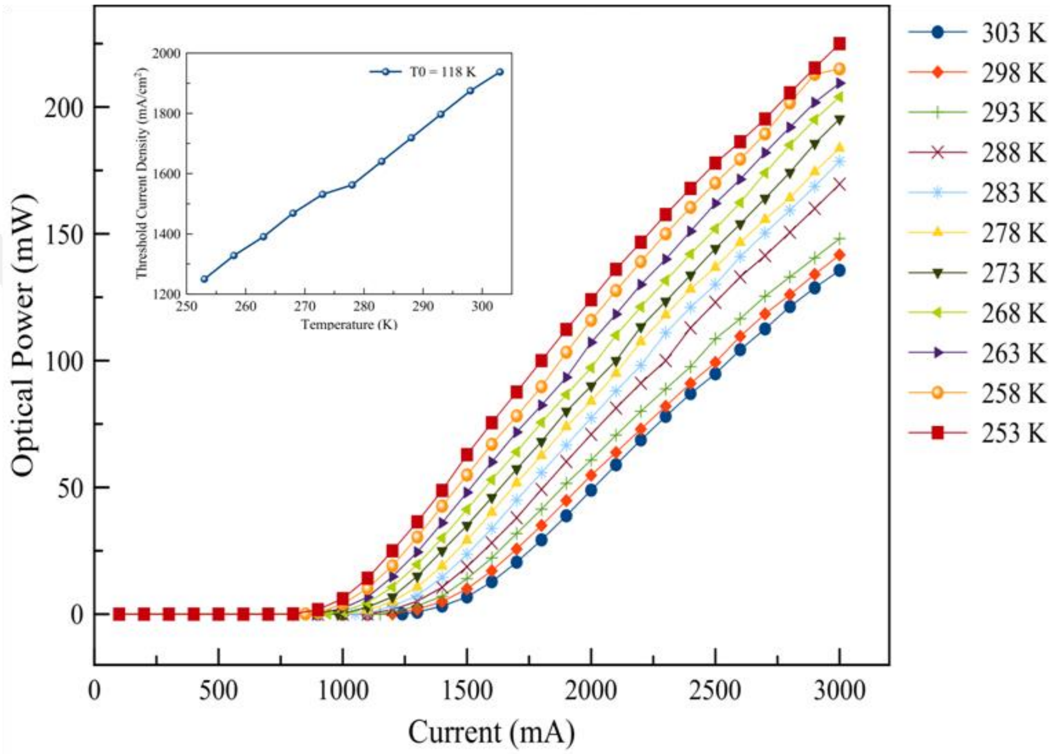

Figure 4.6 The optical power – current measurement (1% duty cycle) for device for which waveguide length is 4 mm and ridge width is 20 μm at different temperatures. Temperature dependent threshold current density and characteristic temperature (T_0) is shown.

The optical power – current measurement (1% duty cycle) for device whose cavity length is 4 mm and cavity width is 20 μm is shown in Figure 4.6. As operation temperature decrease, threshold current decreases and output optical power increases, since population inversion and lifetimes strongly depend on temperature as it is discussed in chapter two. The threshold current density extracted from optical power – current measurement with different temperatures and temperature – threshold density behavior is also presented in Figure 4.6. The characteristic temperature (T_0), which is temperature performance parameter for lasers, is extracted by fitting threshold current density and temperature with the formula;

$$J_{th} = J_{th}e^{T/T_0} \quad (4.1)$$

The characteristic temperature (T_0) shows the temperature performance of the lasers, it indicates how much lasers will effect with temperature increment. High T_0 is desirable for high performance lasers since high T_0 means with temperature increment threshold current rise slowly and optical power decrease less. T_0 is not only depends on active region design but also it depends waveguide design, packaging design and size of the device.

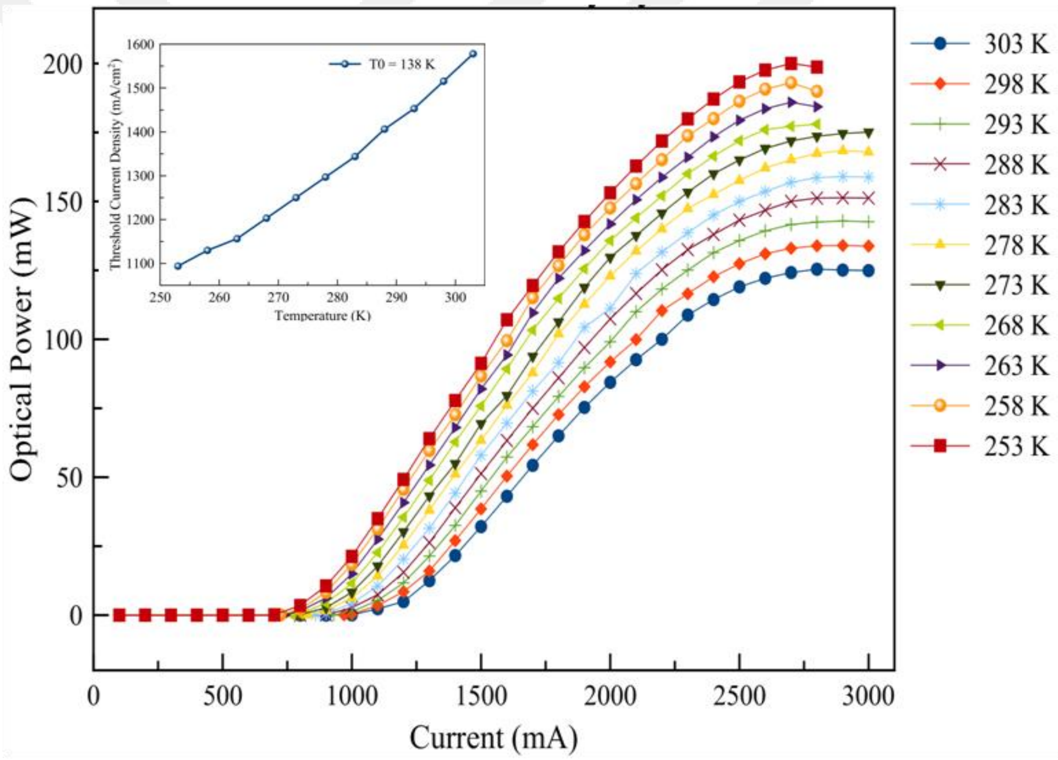

Figure 4.7 The optical power – current measurement (1% duty cycle) for device for which waveguide length is 4 mm and ridge width is 20 μm at different temperatures. Temperature dependent threshold current density and characteristic temperature (T_0) is shown.

The optical power – current measurement (1% duty cycle) for device whose cavity length is 4 mm and cavity width is 16 μm is shown in Figure 4.7. Since cavity width decreases from 20 μm to 16 μm, optical power and threshold current decreases slightly. However since device size is reduced characteristic temperature increases as well.

Threshold currents of quantum cascade lasers are naturally very high when compared to conventional semiconductor lasers, which is due to very short nonradiative lifetime of quantum cascade lasers' energy states especially upper laser level lifetime (in the order of picoseconds). However characteristic temperature of quantum cascade lasers are higher than conventional semiconductor lasers, which means quantum cascade lasers are more robust to temperature since phonon scattering which is dominant upper state nonradiative relaxation mechanism is less temperature dependent than Auger recombination in conventional semiconductor lasers.

In order to analyze high duty cycle behavior of the quantum cascade laser 20% duty cycle current pulses are applied to the device whose cavity length is 4 mm and cavity width is 16 µm. Average optical power – applied current (20% duty cycle) measurement at different temperatures is presented in Figure 4.8.

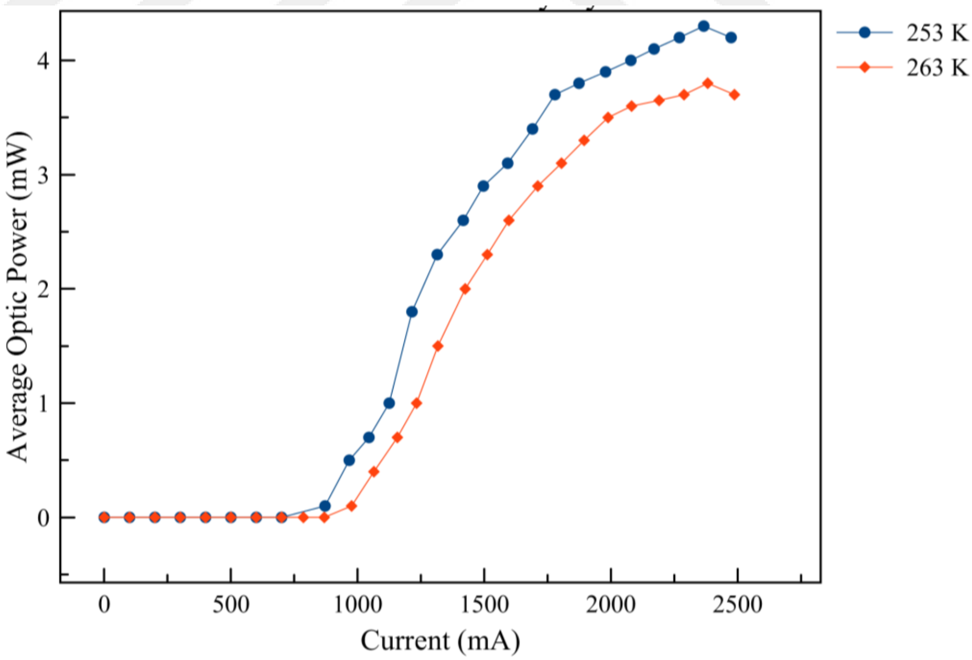

Figure 4.8 The optical power – current measurement (20% duty cycle) for device for which waveguide length is 4 mm and ridge width is 16 µm at different temperatures.

As it is seen in Figure 4.8, high duty cycle operation above 263 K is not possible. After 263 K device for which waveguide length is 4 mm and ridge width is 16 µm breaks down due to high temperature in the active region.

In order to obtain device which can operate with high duty cycle current pulses at room temperature, device length is reduce to half and so as to compensate optical power loss high reflective mirror coating is developed. The optical power – current measurement (1% duty cycle) for devices which are 4 mm length and 20 µm width without mirror coating, 2 mm length and 20 µm width without mirror coating and 2 mm length and 20 µm width with mirror coating is presented in Figure 4.9.

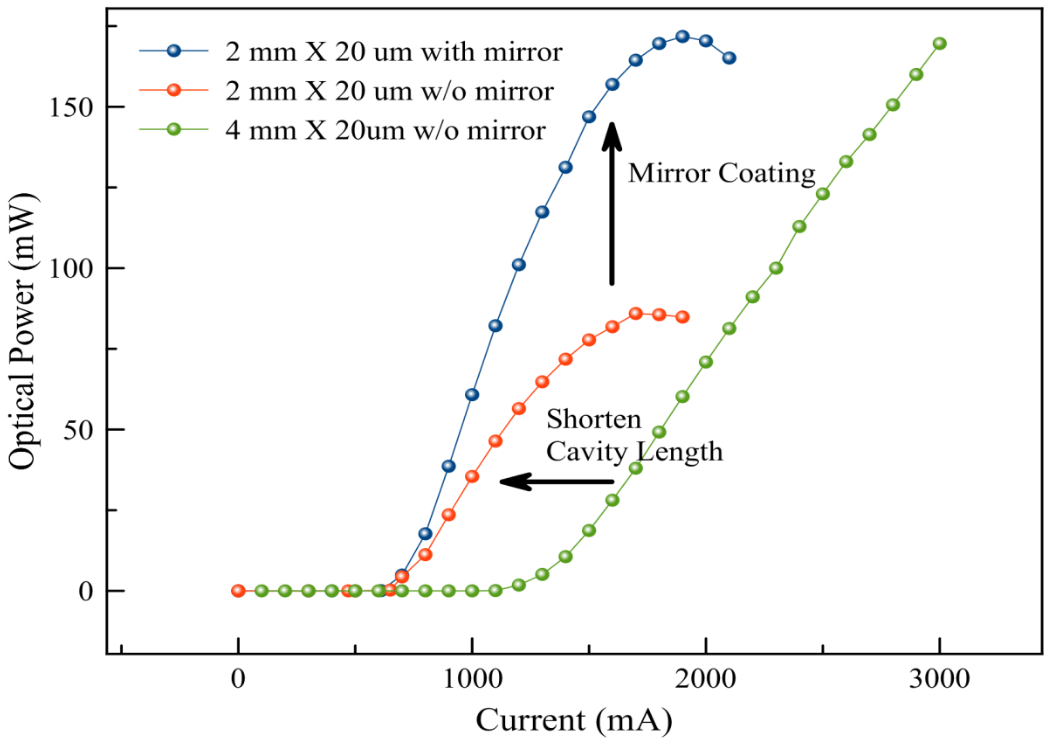

Figure 4.9 The optical power – current measurement (1% duty cycle) for devices which are 4 mm length and 20 µm width without mirror coating, 2 mm length and 20 µm width without mirror coating and 2 mm length and 20 µm width with mirror coating at room temperature.

As presented in Figure 4.9, when cavity length is decreased, both optical power and threshold current reduces. However mirror coating increases the optical power, in addition since mirror coating decreases the mirror loss, it reduces waveguide losses and threshold current decreases as well.

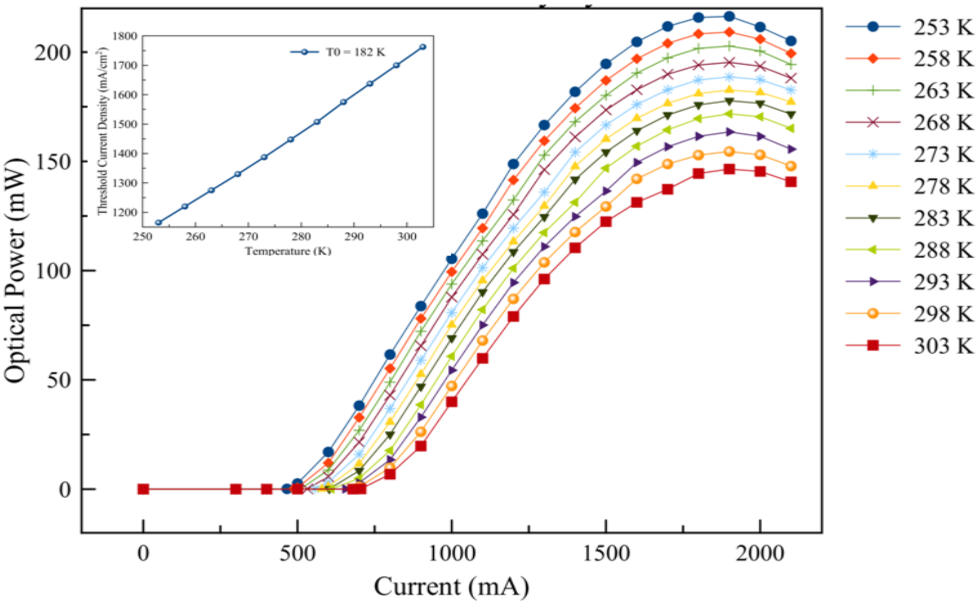

Figure 4.10 The optical power – current measurement (1% duty cycle) for device for which waveguide length is 2 mm and ridge width is 20 µm at different temperatures. Temperature dependent threshold current density and characteristic temperature (T_0) is shown.

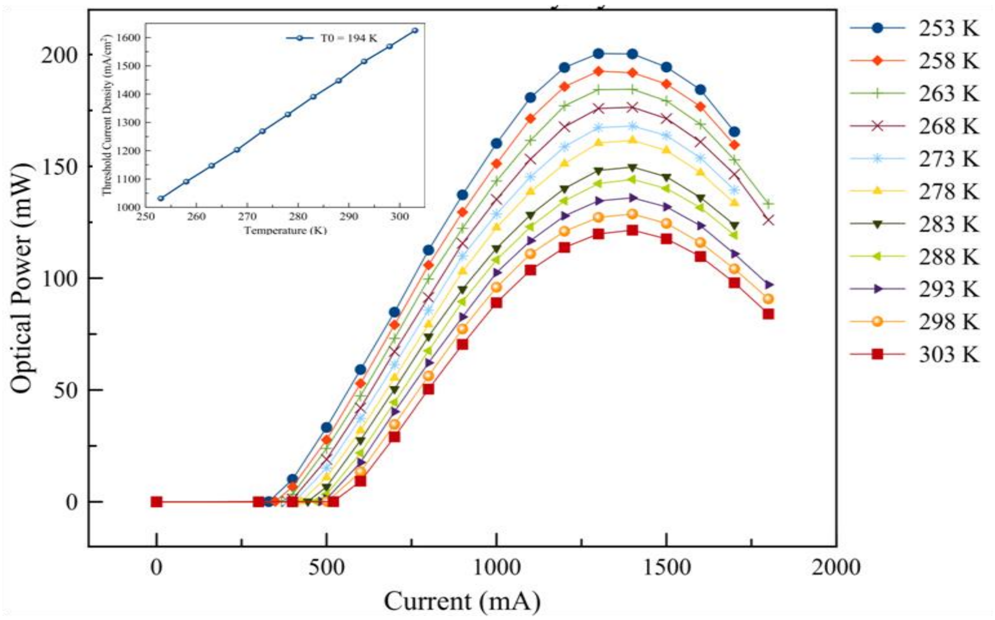

Figure 4.11 The optical power – current measurement (1% duty cycle) for device for which waveguide length is 2 mm and ridge width is 16 µm at different temperatures. Temperature dependent threshold current density and characteristic temperature (T_0) is shown.

The optical power – current measurement (1% duty cycle) for mirror coated device whose cavity length is 2 mm and cavity width is 16 μm is shown in Figure 4.11 and whose cavity length is 2 mm and cavity width is 16 μm is shown in Figure 4.10. Optical powers are almost same as 4 mm length devices but threshold currents are decreased significantly. Therefore required electrical powers to operate devices are decreased. Since devices require lower input power to operate, thermal performance of the quantum cascade lasers get better, which can be easily seen by characteristic temperature of the devices.

The size of cavity especially cavity length has impact on characteristic temperature of the quantum cascade lasers. Characteristic temperatures of the longer devices are much lower than shorter ones. Therefore it can be safely said that, shorter quantum cascade laser are more robust for temperature increment.

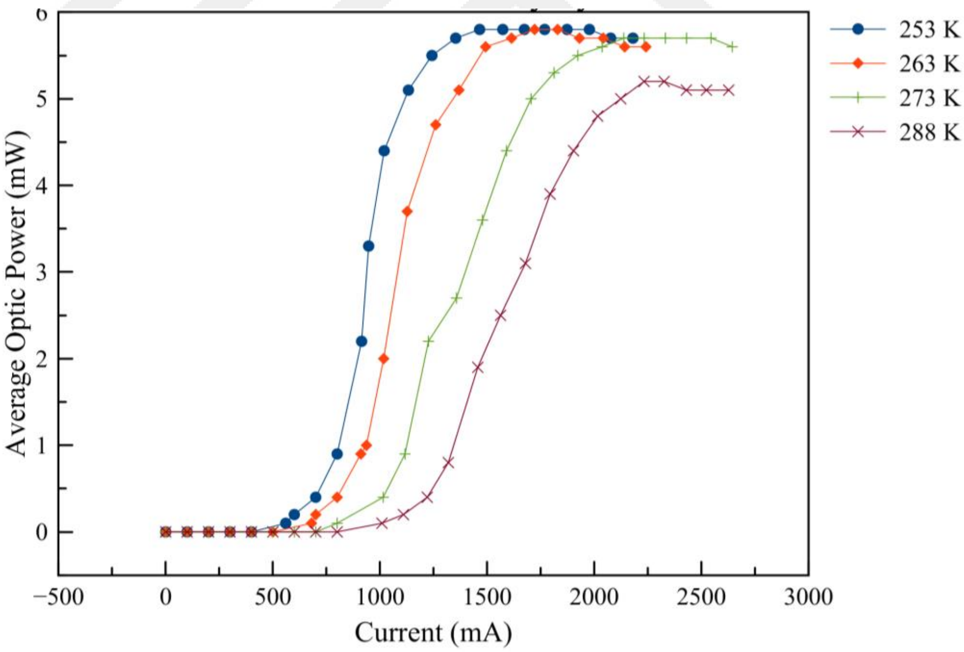

Figure 4.12 The optical power – current measurement (20% duty cycle) for device for which waveguide length is 2 mm and ridge width is 20 μm at different temperatures.

In order to analyze high duty cycle behavior of the quantum cascade laser 20% duty cycle current pulses are applied to the mirror coated device whose cavity length is 2 mm and cavity width is 20 μm. Average optical power – applied current

(20% duty cycle) measurement at different temperatures is presented in Figure 4.12. After decreasing cavity length, since temperature performance of the quantum cascade laser increases, high duty cycle operation at room temperature is possible.

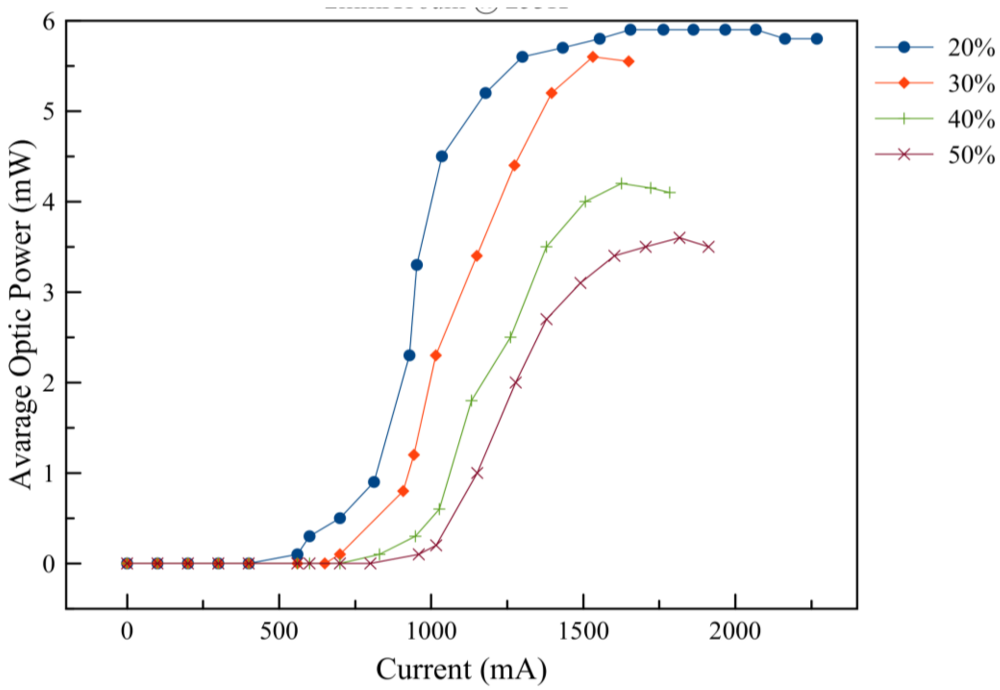

Figure 4.13 The optical power – current measurement (20%, 30%, 40% and 50% duty cycle) for device for which waveguide length is 2 mm and ridge width is 20 µm at room temperature.

To analyze high duty cycle operation of fabricated quantum cascade laser further, 30%, 40% and 50% duty cycle current pulses are applied to device at room temperature (Figure 4.13). High duty cycle behavior is very similar to high temperature behavior, in other words as duty cycle increases since active region temperature increases optical power reduces and threshold current increases as very similar to low duty cycle, temperature increment measurements. In addition after 50% duty cycle devices cannot operate and breaks down. Therefore it can be said that main limitation of the high duty cycle operation is heat removal limitation of active region. If heat removal performance of active region is increased, high duty cycle operation even continuous wave operation will be possible. In literature InP re-growth instead of dielectric coating is proposed a solution of active region cooling [49,50].

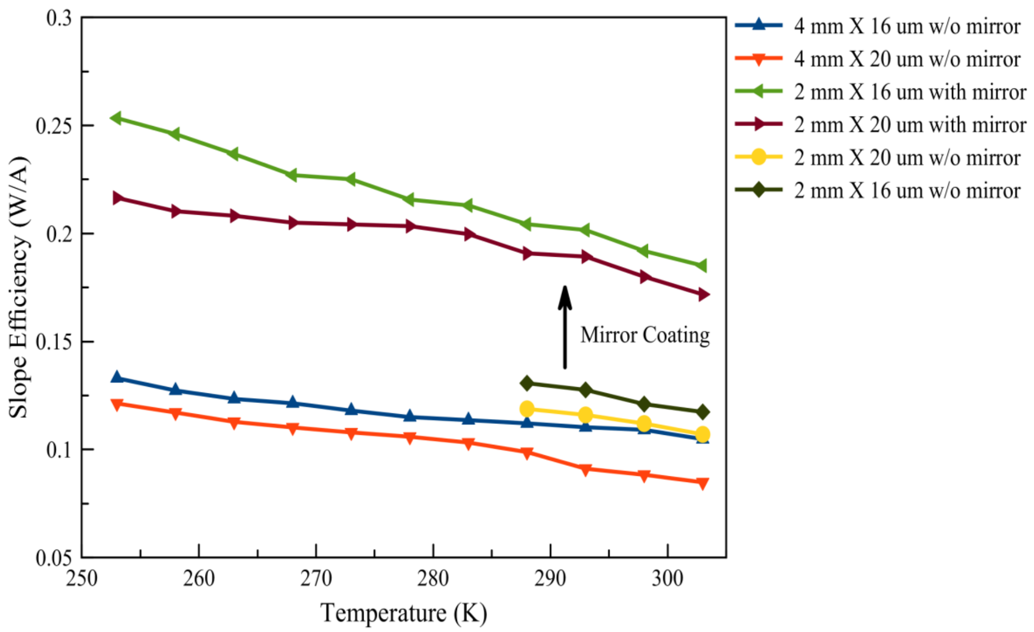

Figure 4.14 Temperature dependent slope efficiency (1% duty cycle) of devices for which waveguide length is 2 mm and ridge width is 20 µm with mirror coating, waveguide length is 2 mm and ridge width is 16 µm with mirror coating, waveguide length is 4 mm and ridge width is 16 µm without mirror coating and waveguide length is 4 mm and ridge width is 20 µm without mirror coating.

Another important performance parameter of quantum cascade lasers is slope efficiency (derivative of optical output power over applied current to the device). Slope efficiency is also temperature dependent parameter as discussed in chapter two. Briefly since phonon population increases as temperature increase, due to phonon scattering; upper laser level lifetime decreases, as a result slope efficiency decreases. Since reducing device sizes improves temperature performance of the quantum cascade laser, as device sizes reduce, slope efficiencies of devices also increase.

In addition since mirror coating reduces the waveguide loss and doubles the output optical power by reflecting back laser beam, it increases the slope efficiency significantly. Temperature dependent slope efficiencies of devices whose length is 2 mm and ridge width is 20 µm with mirror coating, waveguide length is 2 mm and ridge width is 16 µm with mirror coating, waveguide length is 4 mm and ridge width is 20 µm without mirror coating, and waveguide length is 4 mm and ridge width is 16 µm without mirror coating is presented in Figure 4.14.

Current – Voltage (I-V) behavior of the quantum cascade laser for which width is 20 µm and lengths are 2 mm and 4 mm is presented in Figure 4.15. I-V behavior does not depend on temperature but it depends on device dimensions only as expected.

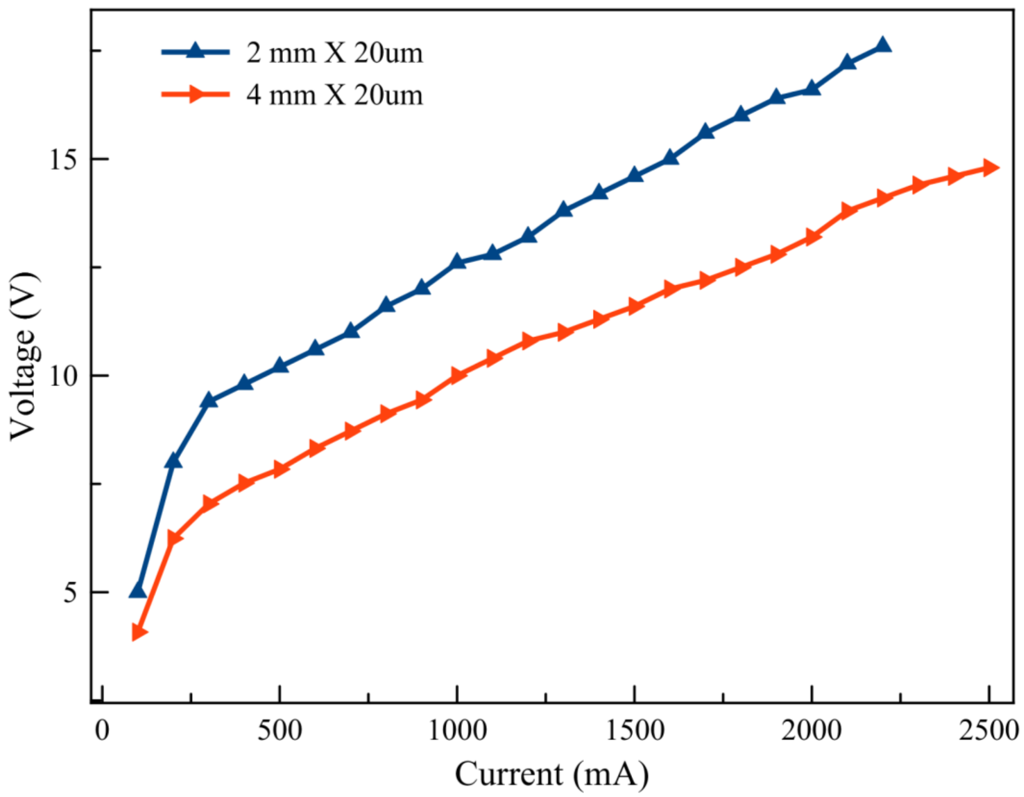

Figure 4.15 Current – Voltage (I-V) measurement (1% duty cycle) for device for which waveguide length is 2 mm, 4 mm and ridge width is 20 µm at room temperature.

4.2.2. Spectrum

The laser spectrum is measured for device for which length is 2 mm and width is 20 µm at different temperatures and different voltage bias using Thorlabs OSA205 Fourier Transform Optical Spectrum Analyzer (Figure 4.4). The spectrum measurement setup illustration is presented in Figure 4.5. The device is operated in pulse mode (1% duty cycle) to suppress self-heating effects.

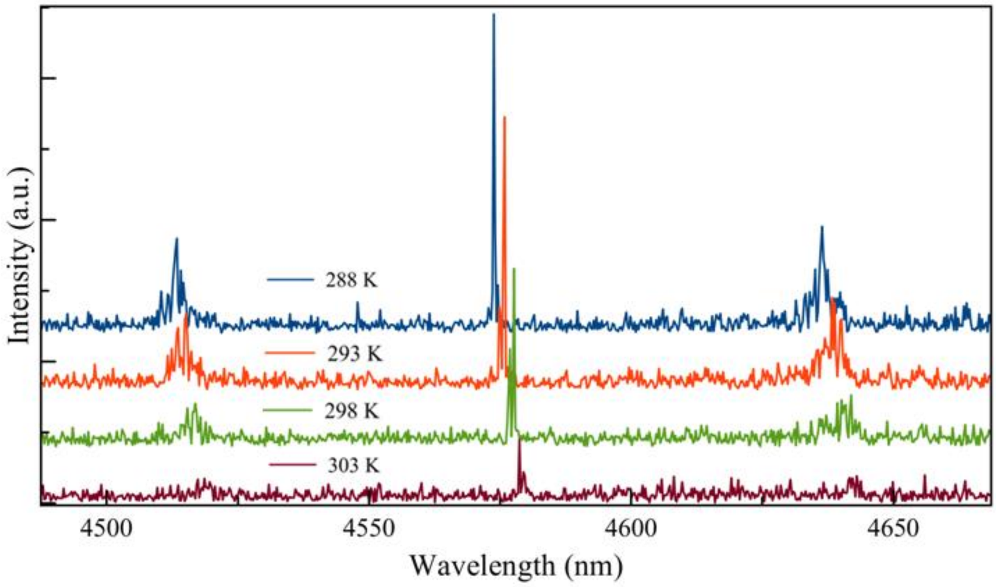

Figure 4.16 Lasing spectrum of the device whose length is 4 mm and width is 20 µm is operated in pulse mode at different temperatures.

The lasing spectrum of the device operated in pulse mode at different temperatures is presented in Figure 4.16. Since increment on device temperature make energy difference between discrete energy levels decrease. The lasing spectrum shows red shift and laser intensity decreases as device temperature is increased. A very narrow linewidth of lasing spectrum of the quantum cascade lasers is the consequences of symmetric gain spectrum since subbands have same parabolic like curvature leads narrow linewidth (Figure 1.3). In contrast conventional semiconductor lasers have opposite curvature of valence and conduction band and due to Pauli's exclusion principle, electron and hole populations are broadly distributed, which results relatively broad gain spectrum and broad lasing linewidth. In addition since quantum cascade lasers are less sensitive to temperature, gain broadening by temperature is lower than conventional semiconductor lasers.

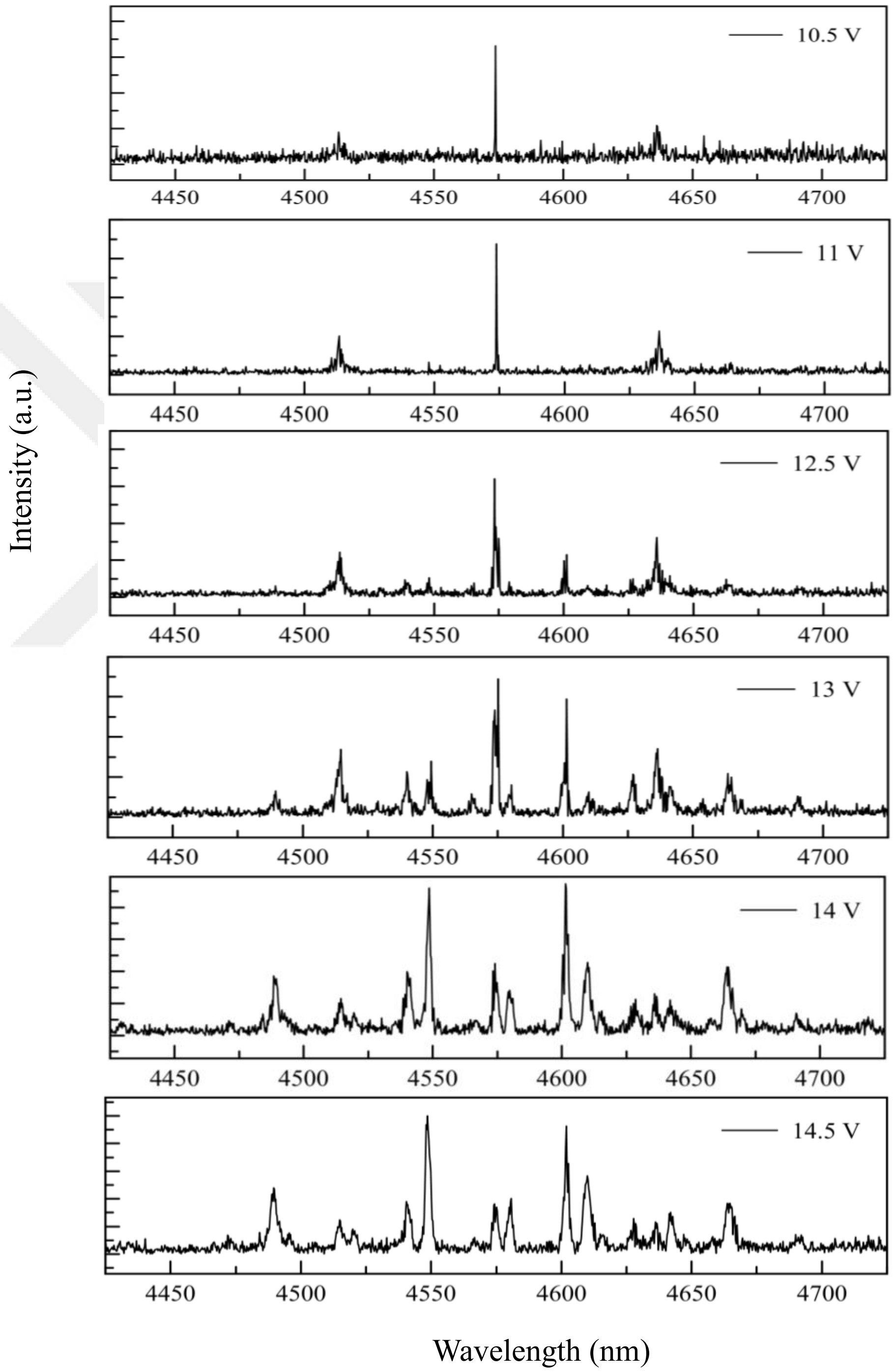

Figure 4.17 Lasing spectrum of the device whose length is 4 mm and width is 20 μm is operated in pulse mode under different bias at room temperature.

The lasing spectrum for the device under different voltage bias is presented in Figure 4.17. Under lower voltage biases, single longitudinal laser mode is available but as voltage bias steps up multiple longitudinal modes appear. The spectral hole burning and active region inhomogeneity (as voltage goes up energy levels' positions are changed and new upper laser states may be available) causes inhomogeneous broadening. Therefore as voltage bias goes up laser spectrum gets broader and even laser wavelength may be changed due to energy level variations under high voltages.

Chapter 5

Conclusions

The quantum cascade laser technology is very promising for long wavelength semiconductor laser source. Quantum cascade lasers are based on intersubband electron transition instead of electron-hole recombination as conventional semiconductor lasers do. Since intersubband transition energy is independent of material band gap, and it can be engineered just by changing material thickness easily. In addition quantum cascade lasers are the best devices as infrared laser source when considering complexity, cost and reliability.

In this thesis, detailed study over mid-infrared quantum cascade laser has been conducted with includes theoretical background review, theoretical analysis, quantum cascade laser design, quantum mechanical, thermal and optical simulations, device fabrication and optimization and experimental characterization.

The purpose of this work was to the developed quantum cascade laser which emits laser beam in between 3 μm to 5 μm wavelength and it must be operated above 50 mW pulsed optical power under 1% pulsed operation and it must be operated in continuous mode with minimum 5 mW optical power at room temperature.

As a result of this work, we developed quantum cascade laser emitting 4.5 μm wavelength and operates at room temperature with more than 150 mW pulsed optical power under 1% duty cycle. We obtain 6 mW average optical power under 20% duty cycle bias.

Although InP or GaAs based quantum cascade lasers has been studied a lot and even they have already been commercialized, GaN based quantum cascade lasers is very infant. Since GaN/AlN interface has large conduction band discontinuity, short wave quantum cascade lasers (minimum 1.08 μm is possible [51]) can also be possible. GaN/AlN based quantum cascade laser is very promising for optical communication, since intersubband transition has very high frequency modulation property.

Additionally, since optical phonon energy of GaN (94 meV) is higher than InP and GaAs based material systems, high temperature laser operation and room temperature THz quantum cascade laser are also possible with GaN based quantum cascade laser.

There are several theoretical proposals about GaN/AlN based quantum cascade laser exist in the literature [52, 53, 54], however, there is no GaN/AlN quantum cascade laser (except THz emitting) has been reported so far. Further works required in terms of epitaxy growth and growth optimization, because due to large lattice mismatch and defect structures of GaN/AlN in order to realize GaN/AlN based quantum cascade laser[55].

Therefore the future work of this thesis is to develop GaN/AlN based quantum cascade laser.

Bibliography

[1] “Quantum cascade laser technology.” http://www.daylightsolutions.com/technology/quantum_cascade laser_technology.htm. Accessed: 2017-04-22.

[2] “Mid-IR applications.” http://www.hcphotonics.com/applications.asp?sn=1009. Accessed: 2017-04-22.

[3] J. Faist, *Quantum cascade lasers*. Oxford, United Kingdom: Oxford University Press, 2013.

[4] R. F. Kazarinov and R. A. Suris, “Possibility of the Amplification of Electromagnetic Waves in a Semiconductor with a Superlattice,” *Soviet Physics—Semiconductors*, vol. 5, no. 4, pp. 707-710, 1971.

[5] A. T. Muhammad, “Analysis of Self-Induced Transparency Modelocking of Quantum,” PhD Thesis, Dept. Elec. Eng., University of Maryland Baltimore County, Baltimore, United States, 2010.

[6] L. Esaki and R. Tsu, "Superlattice and Negative Differential Conductivity in Semiconductors," *IBM Journal of Research and Development*, vol. 4, no. 1, pp. 61-65, 1970.

[7] J. Faist, F. Capasso, D. L. Sivco, C. Sirtori, A. L. Hutchinson, A. Y. Cho1, “Quantum cascade lasers,” *Science*, vol. 264, no. 5158, pp. 553-556, 1994.

[8] G. DEHLINGER *et.al*., “Intersubband Electroluminescence from Silicon-Based Quantum Cascade Structures,” *Science*, vol. 290, no. 5500, pp. 2277-2280,2000.

[9] R. Bates et al., "THz electroluminescence from Si/SiGe quantum cascade heterostructures," in *Lasers and Electro-Optics CLEO '02*, California, United States, 2002, pp. 629-630.

[10] D. A. B. Miller, *Quantum mechanics for scientist and engineers*. Cambridge, England: Cambridge University Press, 2008.

[11] G. Bastard, *Wave mechanics applied to semiconductor heterostructures*. Les Ulis, France: EDP Sciences , 1994.

[12] D. J. BenDaniel, C. B. Duke, “Space-Charge Effects on Electron Tunneling,” *Phys. Rev.*, vol. 152, no. 683, pp. 683—692, 1966.

[13] D. F. Nelson, R. C. Miller, and D. A. Kleinman, “Band nonparabolicity effects in semiconductor quantum wells,” *Phys. Rev. B*, vol. 35, no. 14, pp. 7770-7773, 1987.

[14] R. P. Leavitt, “Empirical two-band model for quantum wells and superlattice in an electrical field,” *Phys. Rev. B*, vol. 44, no. 20, pp. 11270-11280, 1991.

[15] A. Wittmann, “High-performance quantum cascade laser sources for spectroscopic applications,” PhD Thesis, Dept. Elec. Eng., ETH., Zürich, Switzerland, 2009.

[16] P. Harrison, *Quantum wells, wires and dots.* New Jersey, United States: Wiley, 2005.

[17] X. Luyao, “Mid-infrared Quantum Cascade Lasers Modeling, Fabrication and Characterization,” Ms Thesis, Dept. Elec. and Comp. Eng., MIT., Cambridge, United States, 2009.

[18] A. E. Sigman, *Lasers.* Mill Valey, United States: University Science Books, 1986.

[19] T. Ando, “Broadening of Inter-Subband Transitions in Image-Potential-Induced Surface States outside Liquid Helium,” *J. Phys. Soc. Jpn.*, vol. 44, no. 3, pp. 765-773, 1978.

[20] G. Bastard, “Energy levels and alloy scattering in InP- In (Ga)As heterojunctions,” *Applied Physics Letters,* vol.43, no. 6, pp. 591-593, 1983.

[21] T. Unuma and M. Yoshita, “Intersubband absorption linewidth in GaAs quantum wells due to scattering by interface roughness, phonons, alloy disorder, and impurities”, *Applied Physics Letters*, vol. 93, no. 3 , pp. 1586-1597, 2003.

[22] M. Beck *et.al*., “Continuous Wave Operation of a Mid-Infrared Semiconductor Laser at Room Temperature,” *Science*, vol. 295, no. 5553, pp. 301-305, 2002.

[23] B.E. A. Saleh and M. C. Teich, *Fundamentals of Photonics*. New Jersey, United States: Wiley, 2007.

[24] J. Faist *et.al*., “High power mid- infrared (λ~5 μm) quantum cascade lasers operating above room temperature,” *Applied Physics Letters,*vol. 68, no. 26, pp. 3680-3682, 1996.

[25] A. Yariv, *Quantum Electronics.* New Jersey, United States: Wiley, 1989.

[26] C. Sirtori, *et.al*., “Resonant tunneling in quantum cascade lasers,” *IEEE J. Quantum Electron.*, vol. 34, no. 9, pp. 1722-1729, 1998.

[27] S. Mukamel, *Principles of nonlinear optical spectroscopy*. Oxford, United Kingdom: Oxford University Press, 1995.

[28] J. Faist *et.al*., “Vertical transition quantum cascade laser with Bragg confined excited state,” *Applied Physics Letters*, vol. 66, no. 5, pp. 538-540, 1995.

[29] C. Gmachl, F. Capasso, D. Sivco and A. Cho, “Recent progress in quantum cascade lasers and applications”, *IOP*, vol. 64, no. 11, pp. 1533–1601, 2004.

[30] H. K. Lee, J. S. Yu, “Thermal analysis of short wavelength InGaAs/InAlAs quantum cascade lasers,” *Solid-State Electron*, vol. 54, no. 8, pp. 769-776, 2010.

[31] Chen G, “Thermal conductivity and ballistic-phonon transport in the crossplane direction of superlattices,” *Phys Rev B*, vol. 57, no. 23 , pp. 14958-14973, 1998.

[32] X. Luyao, “Mid-infrared Quantum Cascade Lasers Modeling, Fabrication and Characterization,” Ms Thesis, Dept. Elec. and Comp. Eng., MIT., Cambridge, United States, 2009.

[33] K. J. Franz, ”New quantum cascade laser architectures: II-VI quantum cascade emitters, high k-space lasing, and short injectors,” PhD Thesis, Dept. Elec. Eng., Princeton University, New Jersey, United States, 2009.

[34] “Molecular Beam Epitaxy.” http://archive.cnx.org/contents/0b2614e4-aa98-49c1-bf50-1db3ee3c5ecd@2/molecular-beam-epitaxy. Accessed: 2017-04-22.

[35] A. Bismuto, “Mid-infrared quantum cascade lasers: active medium and wave guide engineering,” PhD Thesis, Dept. Elec. Eng., ETH., Zürich, Switzerland, 2011.

[36] T. Gresch, “Gain and waveguide engineering in mid-infrared quantum cascadelasers”, PhD Thesis, Dept. Elec. Eng., ETH., Zürich, Switzerland, 2009.

[37]http://www.microchemicals.com/technical_information/image_reversal_resists.pdf

[38] C. Gmachl, F. Capasso, D. Sivco and A. Cho, “Recent progress in quantum cascade lasers and applications”, *IOP*, vol. 64, no. 11, pp. 1533–1601, 2004.

[39] J. Faist *et.al*., “Quantum cascade laser: Temperature dependence of the performance characteristics and high T0 operation,” *Applied Physics Letters*, vol. 65, no. 23, pp. 2901-2903, 1994.

[40] B. G. Lee *et.al*., “Widely tunable single-mode quantum cascade laser source for mid-infrared spectroscopy,” *Applied Physics Letters*, vol. 91, no. 23, pp. 1101-1104, 2007.

[41] X. Huang *et.al*., “Ridge-width dependence of the threshold of long wavelength (λ ≈14 μm) quantum cascade lasers with sloped and vertical sidewalls,” *Opt. Express*, vol. 30, no. 20, pp. 2539-2547, 2012.

[42] A.R Clawson, “Guide to references on III–V semiconductor chemical etching,” *Materials Science and Engineering: R: Reports*, vol. 31, no. 15, pp. 1-6, 2001.

[43] A. T. Muhammad, “Analysis of Self-Induced Transparency Modelocking of Quantum,” PhD Thesis, Dept. Elec. Eng., University of Maryland Baltimore County, Baltimore, United States, 2010.

[44] S. A. Maier, *Plasmonics: Fundamentals and Applications*. Berlin, Germany: Wiley, 2007.

[45] A. Szerling *et.al*., “Influence of Mesa-Fabrication-Dependent Waveguide-Sidewall Roughness on Threshold Current and Slope Efficiency of AlGaAs/GaAs Mid-Infrared Quantum-Cascade Lasers,” *Terahertz and Mid Infrared Radiation: Detection of Explosives and CBRN*, vol. 20 , pp. 143-151, 2014.

[46] C. A. Evans, “Investigation of Thermal Effects in Quantum-Cascade Lasers,” *IEEE Journal of Quantum Electron*., vol. 42, no. 9, pp. 859-867, 2006.

[47] H Page, “High reflectivity metallic mirror coatings for mid-infrared ($\lambda \approx 9$ μm) unipolar semiconductor lasers,” *Semicond. Sci. and Tech*., vol. 17, no. 22, pp. 1312-1316, 2002.

[48] R. Maulini *et.al*., “High power thermoelectrically cooled and uncooled quantum cascade lasers with optimized reflectivity facet coatings,” *Applied Physics Letters*, vol. 95, no. 15, pp. 1112-1115, 2009.

[49] M. Razeghi *et.al*., “Quantum cascade lasers that emit more light than heat,” *Nature Photonics*, vol. 4, no. 2, pp. 99-102, 2010.

[50] M. Beck *et.al.*, “Continuous Wave Operation of a Mid-Infrared Semiconductor Laser at Room Temperature”, *Science,* vol. 295, no. 5553, pp. 301-305, 2002.

[51] K. Kishino, A. Kikuchi, H. Kanazawa, and T. Tachibana, “Intersubband transition in (GaN)m/(AlN)n superlattices in the wavelength range from 1.08 to 1.61 μm,” *Applied Physics Letters,* vol. 81, no. 7, pp. 1234-1236, 2002.

[52] A. Ishida *et.al.*, “AlN/GaN Near-Infrared Quantum-Cascade Structures with Resonant-Tunneling Injectors Utilizing Polarization Fields,” J. Appl. Phys, vol. 41, no. 11, pp. 1303–1305, 2004.

[53] A. Ishida *et.al.*, “Quantum-Cascade Structure in AlN/GaN System Assisted by Piezo-Electric Effect,” J. Appl. Phys, vol. 41, no. 3, pp. 236–238, 2002.

[54] V. D. Jovanović, D. Indjin, Z. Ikonić, and P. Harrison, “Simulation and design of GaN/AlGaN far-infrared (λ∼34 μm) quantum-cascade laser,” vol. 84, no. 16, pp. 2995-2997, 2004.

[55] M Beeler and E Trichas and E Monroy, “III-nitride semiconductors for intersubband optoelectronics: a review,” Semicon. Sci. and Tech., vol. 28, no. 7, pp. 1-25, 2013.